The mitigation of underwater noise by PULSE

A study on the effects of impulse elongation and its interaction with air-bubble curtains

Floris Hilmer

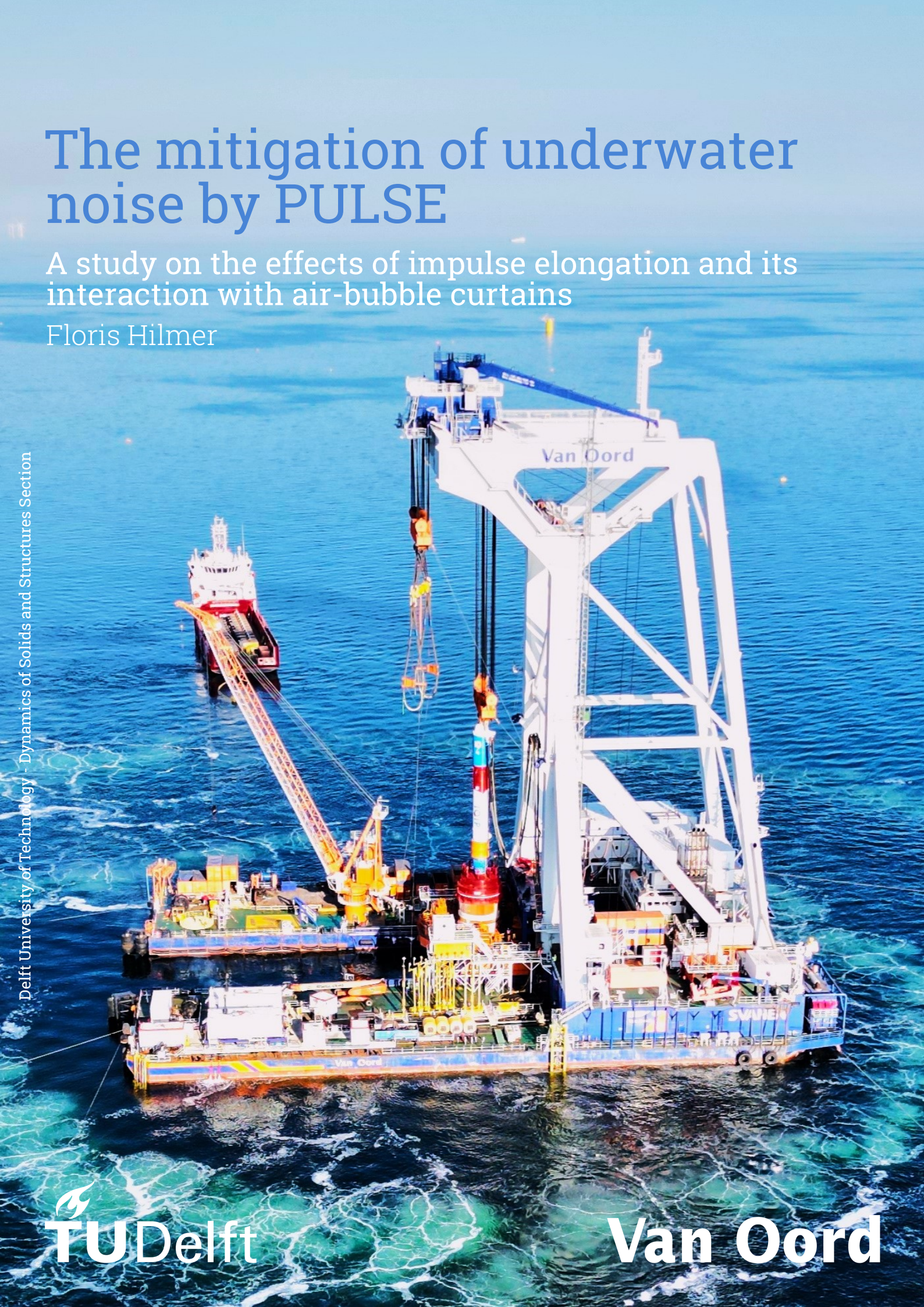

Delft University of Technology - Dynamics of Solids and Structures Section

TU Delft

Van Oord

The mitigation of underwater noise by PULSE

A study on the effects of impulse elongation and its interaction with air-bubble curtains

by

Floris Hilmer

to obtain the degree of Master of Science
at the Delft University of Technology,
to be defended publicly on Wednesday September 11, 2024 at 16:00 PM.

Student number:	4687418		
Project duration:	November 13, 2023 – September 11, 2024		
Thesis committee:	dr. ir. A. Tsouvalas	TU Delft	Chairman
	dr. ir. A. Faragau	TU Delft	Daily supervisor
	ir. G. W. Guichelaar	Van Oord	Company supervisor
	dr. ir. Y. Peng	TU Delft	University supervisor

An electronic version of this thesis is available at http://repository.tudelft.nl/.

TU Delft

Van Oord
Marine ingenuity

Preface

This thesis marks my final work as a student at Delft University of Technology and the completion of my Master's degree in Structural Engineering at the Faculty of Civil Engineering and Geosciences. On November 13th, this journey began with an initial deep dive into the fascinating world of underwater acoustics. Now, eight months later, I can reflect on a period that has been incredibly educational, interesting, and enjoyable, helping me discover my interests. This thesis has ignited my passion for the energy transition and reinforced my commitment to contributing to sustainable energy solutions.

Of course, this thesis would not have been possible without the support of many people. Firstly, I would like to thank Apostolos Tsouvalas for his expertise in underwater noise and his critical insights and guidance on the topic. Secondly, I am grateful to Gerwin Guichelaar, noise specialist at Van Oord, for his dedication during our weekly meetings, invaluable guidance, and passion for this field of engineering. I also appreciate the opportunity to research this topic at Van Oord. Thirdly, I want to express my gratitude to my daily supervisor, Andrei Faragau, for his pragmatic mindset, relaxed attitude, and for teaching me how to think as a scientist rather than merely an engineer. Also, I would like to thank Yaxi Peng for her patience in helping me understand the complex SILENCE model.

I would like to finish off this acknowledgement with special thanks to my family, friends and girlfriend for their unconditional support and belief in me. Maintaining a strong work ethic from 8:00 to 17:30 was important, but the distractions and side activities after closing my laptop or during the weekend were just as essential for the quality of my work. As this chapter of my academic journey concludes, I am grateful for the exciting journey Delft has brought me and the memories I have made over the past years.

Enjoy reading!

Floris Hilmer
Rotterdam, September 2024

Abstract

Nations worldwide are striving to meet the climate goals set forth by the Paris Agreement and reduce greenhouse gas emissions, with offshore wind farms (OWFs) playing a crucial role. However, OWF construction generates underwater noise from impact piling, which is harmful to marine life. This study examines the effects of PULSE – a novel mitigation measure acting as a spring-damper system between the hydraulic hammer and monopile – on underwater noise and its interaction with air-bubble curtains. Using the semi-analytical SILENCE model, the complete pile-water-soil system is simulated to evaluate noise levels, with the model's predictions compared to field data from a recent German project. Results show that PULSE effectively reduces both Sound Exposure Level (SEL) and Peak Sound Level (L_{peak}) by shifting acoustic energy from higher to lower frequencies. When combined with air-bubble curtain configurations, noise reductions are greater, but the effectiveness of PULSE diminishes. Consequently, the individual performance of PULSE and air-bubble curtains cannot be linearly added to predict their combined effectiveness. In conclusion, while PULSE effectively mitigates underwater noise, its combined use with air-bubble curtains impacts overall mitigation efficiency and requires careful evaluation.

Executive summary

Nations worldwide are striving to meet ambitious climate goals and reduce greenhouse gas emissions, making offshore wind energy a significant contributor to clean power. These climate goals, set forth by international agreements such as the Paris Agreement, aim to limit global warming to well below 2 degrees Celsius above pre-industrial levels and to pursue efforts to limit the temperature increase to 1.5 degrees Celsius. Offshore wind farms (OWFs) play a vital role in achieving these targets, with predictions indicating a substantial increase in their deployment. However, the construction of OWFs presents challenges, particularly the underwater noise generated by impact piling. Impact piling, the dominant method for installing monopiles – the most widely used foundation for offshore wind turbine generators (OWTGs) – involves transferring energy from a hydraulic impact hammer to the monopile, driving it into the seabed. This process radiates acoustic energy into the water and soil, resulting in underwater noise that disrupts and potentially harms marine life. Consequently, governments are implementing regulations to limit this underwater noise, necessitating the use of mitigation measures during monopile installation.

One such mitigation measure is PULSE, a novel *transition piece* that functions as a spring-damper system between the pile-driving hammer and the sleeve (anvil). PULSE consists of two hydraulic pistons separated by a fluid medium. It elongates the input force, resulting in a smaller amplitude but a longer duration of the impulse. The liquid volume inside can be adjusted, with settings ranging from *minimum PULSE* to *maximum PULSE*. While PULSE is currently used in the industry, its effects on sound levels – particularly when combined with other mitigation measures such as air-bubble curtains, which create a barrier of rising air bubbles around the monopile to prevent noise leakage – have not been extensively researched. Moreover, measuring its effects is challenging due to the complexities involved in quantifying its impact, which arises from the fact that PULSE is typically employed alongside other mitigation measures in the industry. This study aims to address this research gap.

This study has two primary objectives: (i) investigate how PULSE affects pile vibrations and underwater noise radiation, including the frequency shift it introduces; and (ii) assess the effectiveness of PULSE when combined with different configurations of air-bubble curtains by examining modifications in the frequency spectrum. These objectives enhance the understanding of PULSE's impact on underwater noise and address the following main research question:

To what extent does PULSE influence radiated underwater noise and interact with other mitigation measures such as air-bubble curtains?

To address the research objectives, the complete pile-water-soil system is modelled using the semi-analytic SILENCE model developed by the Environmental Vibrations & Acoustics (EVA) lab at TU Delft. The model consists of two main modules: a sound generation module, capturing interactions between the pile, water, and soil; and a sound propagation module, tracing the wavefield propagation at greater distances from the pile. The system's configuration includes a monopile, a hydraulic hammer, simplified as a vertical impulse, and the surrounding fluid and soil mediums. Key parameters such as shell stresses, displacements, water pressures, and soil stresses determine sound levels in the surrounding media.

Modelling the impact of PULSE involves multiplying the system's frequency response, due to a unit amplitude hammer excitation, with the exact time force depending on the PULSE setting. For air-bubble curtains, SILENCE incorporates a dedicated module to calculate sound transmission losses for different configurations. The reduced pressure sources at the position of the air-bubble curtain are then propagated to larger distances to compute the field at the receiver location. Combining the modelling of PULSE and air-bubble curtains is achieved by multiplying the system's frequency response, accounting for air-bubble curtain configurations and subjected to a unit load, with the exact time force depending

on the PULSE setting. Various scenarios are simulated, including PULSE without additional mitigation measures, and PULSE combined with a single Big Bubble Curtain (BBC) and a Double Big Bubble Curtain (DBBC). The model is compared to field data from a recent German project, provided by Van Oord, to confirm the predicted sound levels.

The comparison with field data shows excellent agreement for a receiver located 750 meters from the monopile and 2 meters above the seabed, a distance chosen to comply with regulations. The model for PULSE without additional mitigation measures overestimates the Sound Exposure Level (SEL) by 0.6 dB and underestimates the Peak Sound Level (L_{peak}) by 0.5 dB. Similarly, the model's predictions for PULSE combined with air-bubble curtains were within 0.5 dB of the measured SEL and 0.4 dB of the measured L_{peak}. Qualitatively, the model's spectral analysis aligned well with the field data across most frequency ranges, although it overestimates sound levels at lower frequencies and drops off earlier at higher frequencies when examining 1/3 octave band SEL values. The deviations in both cases fall within the uncertainty range of the results, which stems from inherent uncertainties in the parameter values, primarily soil parameters, and measurements [49].

Elongating the impulse for different PULSE settings reduces the peak amplitude of the energy in the monopile and extends its duration. Additionally, longer impulses favour the transmission of energy into the soil rather than the water, leading to a noticeable redistribution of energy with increasing impulse duration. This indicates that soil absorption becomes more significant when elongating the impulse.

Quantitative analyses of sound levels under different PULSE settings demonstrated that elongating the impulse duration effectively reduces both SEL and L_{peak} at various distances from the monopile. For instance, at 750 meters from the monopile, the *maximum PULSE* setting reduces SEL by 3.4 dB and L_{peak} by 6.8 dB relative to the baseline scenario *no PULSE*. When combined with a BBC, SEL is reduced by 3.8 dB and L_{peak} by 8.7 dB compared to *no PULSE*, while using a DBBC results in reductions of 4.9 dB in SEL and 9.2 dB in L_{peak}. However, since these reductions are logarithmic representations of sound levels, they can be misleading. To accurately assess the effectiveness of PULSE combined with air-bubble curtains, actual pressure value reductions must also be considered. The pressure reductions are significantly lower when a (D)BBC is added compared to when no (D)BBC is used, indicating that the efficiency of PULSE decreases when air-bubble curtains are introduced.

Qualitative analyses of the frequency spectra reveal that elongating the impulse using PULSE shifts the acoustic energy distribution. Without PULSE, energy concentrates at higher frequency bands, resulting in greater sound levels in these ranges. However, with PULSE, particularly at the *maximum PULSE* setting, there is a noticeable redistribution of energy from higher to lower frequencies. This shift reduces sound levels at frequencies above 32 Hz while increasing sound levels at frequencies below 32 Hz. A similar trend is observed when PULSE is combined with air-bubble curtains, but less energy is added to the low frequencies. It must be emphasised that this energy redistribution is relative to the baseline scenario, meaning that the changes in the bands below 32 Hz are less impactful than those in the higher frequency bands due to amplitude differences. Additionally, the overall sound levels are lower when a (D)BBC is applied, as the (D)BBC also mitigates noise. Consequently, the absolute amount of energy redistributed is reduced when adding a (D)BBC to the system.

The model results demonstrate that PULSE effectively reduces underwater noise from offshore piling activities. However, when combined with air-bubble curtains, the effectiveness of PULSE is diminished, as indicated by the differences in pressure levels. Therefore, it is important to emphasise that the individual performance of PULSE and air-bubble curtains cannot be linearly added to predict their combined effectiveness.

Contents

Abbreviations

Abbreviation	Definition
BBC	Big Bubble Curtain
BSH	Federal Maritime and Hydrographic Agency
CPT	Cone Penetration Test
DBBC	Double Big Bubble Curtains
dB	Decibel
FAD	Free Air Delivery
FD	Finite Difference
FEM	Finite Element Model
GDP	Gentle Driving of Piles
HSD-system	Hydro-Sound-Damper System
IEA	International Energy Agency
LBC	Little Bubble Curtain
L_{peak}	Peak Sound Level
MSFD	Marine Strategy Framework Directive
NMS	Noise Mitigation System
OWF	Offshore Wind Farm
OWTG	Offshore Wind Turbine Generator
Pa	Pascal
PE	Parabolic Equation
PML	Perfectly Matched Layer
p_{rms}	Root Mean Squared Sound Pressure
p_{ref}	Reference Pressure
PULSE	Piling Under Limited Stress Equipment
SEL	Sound Exposure Level
SPL	Sound Pressure Level
TBBC	Triple Big Bubble Curtain

1 Introduction

1.1. Relevancy and motivation

The increasing global emphasis on reducing greenhouse gas emissions and combating climate change has propelled the growth of renewable energy sources, with offshore wind energy emerging as a significant contributor. Offshore wind farms (OWFs) are important for nations striving to meet the ambitious targets set by international agreements like the Paris Agreement, which aims to limit global temperature rise to well below 2 degrees Celsius above pre-industrial levels, with a target of 1.5 degrees Celsius [66]. The International Energy Agency (IEA) projects that offshore wind capacity will need to expand significantly to meet these climate goals, with a predicted 15-fold increase by 2040 [22]. As the deployment of OWFs grows, addressing the environmental impacts associated with their construction, particularly the underwater noise generated during the piling of monopiles[1], is essential.

Underwater noise pollution from impact piling can disrupt marine life, particularly marine mammals, fish, and invertebrates, which rely on sound for communication, navigation, and foraging [51]. The introduction of loud, anthropogenic noises can cause stress, behavioural changes, and even physical harm. For instance, noise can lead to temporary or permanent hearing loss in marine mammals [21]. Fish and invertebrates can experience disruptions in spawning and feeding behaviours, leading to potential population declines [56]. The potential for noise to cause hearing loss, behavioural changes, and habitat displacement in these species has led to the implementation of regulations by governments worldwide, including limits on noise levels and mandatory use of mitigation measures. Table 1.1 provides an overview of the regulations regarding noise limits for countries with significant numbers of wind farms, as detailed by Sánchez et al. [54]. Effective noise mitigation measures are critical to ensuring the sustainable development of OWFs, balancing the need for renewable energy with the protection of marine ecosystems.

In recent years, numerous noise mitigation measures have been developed by research institutes and organisations, targeting both the source and the transmission path of noise. Among the most commonly used methods are the Hydro-Sound-Damper System (HSD-system) and the AdBm Noise Mitigation System (NMS) for near-field noise control, as well as air-bubble curtains for mitigating noise along its transmission path. The HSD-system involves surrounding the monopile with a net of PE-foam or rubber elements to dampen sound, providing another layer of noise reduction [44]. On the other hand, the AdbM NMS employs large arrays of Helmholtz resonators, tuned to specific frequencies, to capture and mitigate noise from various sources [1]. Air-bubble curtains create a barrier of rising bubbles that hinder the propagation of sound waves, enhancing noise reduction during offshore piling [63]. Despite the effectiveness of these path-based solutions, they often need to be supplemented by source-based mitigation measures. One such measure is Gentle Driving of Piles (GDP), which promises to offer a quieter alternative to traditional pile driving methods by significantly reducing noise emissions at the source [19].

[1] Monopiles are the primary foundations used for offshore wind turbine generators (OWTGs) [54].

Table 1.1: Noise limits for OWF construction in countries with a significant number of OWFs, based on governmental regulations. The regulations for the UK and Denmark are derived from the Marine Strategy Framework Directive (MSFD) [14], while those for Germany are based on the Federal Maritime and Hydrographic Agency (BSH) guidelines [65]. Belgium's regulations follow the Belgian MSDF [58], and the Netherlands' noise limits are specified in the Water Act [53].

Country	Regulation	Noise limit (750 m from source)	Additional information
UK	MSFD	-	Specific limits not defined; case-by-case assessment
Germany	BSH	SEL_{05} 160 dB re 1μPa^{2}s L_{peak} 190 dB re 1μPa	Max. piling time of 180 min/monopile
Denmark	MSDF	-	Specific limits not defined; case-by-case assessment
Belgium	Belgian MSDF	L_{peak} 185 dB re 1μPa	-
Netherlands	Water Act	SEL 160 dB re 1μPa^{2}s	-

Another innovative source-based mitigation measure is PULSE (Piling Under Limited Stress Equipment), developed by IQIP. PULSE serves as a *transition piece* between the impact hammer and the monopile, effectively mitigating noise during installation by modifying the input force [26]. PULSE functions as a spring-damper system between the pile-driving hammer and the anvil, consisting of two hydraulic pistons separated by a fluid medium. This configuration elongates the input force, resulting in a smaller amplitude but a longer duration of the impulse. The liquid volume inside the PULSE system can be adjusted, with the following settings: *no PULSE* indicates that there is no PULSE between the hammer and the monopile, *minimum PULSE*, *medium PULSE*, and *maximum PULSE* indicate the presence of 100 mm, 400 mm, and 800 mm of liquid in the PULSE system, respectively. This allows for varying degrees of noise mitigation, where more liquid results in greater noise reduction but increases energy losses during energy transfer.

This study focuses on PULSE, assessing its effectiveness in reducing underwater noise during monopile installation. Understanding its effects is vital for balancing advancing renewable energy infrastructure with preserving marine ecosystems. Research on the impacts of PULSE on underwater noise and its interaction with other mitigation measures, such as air-bubble curtains, can provide valuable insights for industry stakeholders.

1.2. Research gap

PULSE may offer a potential solution to underwater noise by reducing the amplitude of noise generated during pile driving. Although it is currently utilised in the industry, there is a significant lack of comprehensive research on its effectiveness, particularly when combined with other noise mitigation measures like air-bubble curtains. Air-bubble curtains reduce noise levels by creating a barrier of rising air bubbles around the monopile, which disrupts the transmission of sound waves through the water. However, their efficiency can vary widely based on environmental conditions such as water depth, current speed, seabed composition, and the specific configuration of the air-bubble curtain.

The lack of detailed studies on the combined effects of PULSE and air-bubble curtains on underwater noise is identified as a research gap. While PULSE may reduce the noise amplitude at its source, it is unclear how this reduction influences the frequency spectrum of the noise and whether it introduces changes that might impact the performance of air-bubble curtains. For example, if PULSE shifts the dominant frequencies of noise to a range where air-bubble curtains are less effective, the overall noise reduction might not meet expectations. Additionally, accurately measuring the noise reduction attributed to PULSE poses significant challenges due to the complexities involved in quantifying its impact. These challenges arise from the fact that PULSE is typically employed alongside other mitigation measures in the industry. This study aims to address these gaps by thoroughly investigating how PULSE affects pile vibrations and underwater noise. Furthermore, it will evaluate the performance of PULSE in combination with air-bubble curtains, providing a more comprehensive understanding of their combined impact on underwater noise mitigation.

1.3. Research objective and scope

To address the identified research gaps, this study seeks to provide a comprehensive understanding of PULSE's impact on underwater noise and its interaction with air-bubble curtains. The primary aim of this study is to investigate and enhance the knowledge of the effects of PULSE. Specifically, the study focuses on two main objectives:

- **Investigate the effects of PULSE on pile vibrations and underwater noise radiation:** This includes examining the frequency shift introduced by PULSE and determining the frequency range where PULSE is most effective.
- **Assess the effectiveness of PULSE in combination with air-bubble curtains:** This involves evaluating different configurations of air-bubble curtains and how they interact with PULSE. By examining modifications in the frequency spectrum, the study aims to assess the effectiveness of different air-bubble curtain configurations combined with PULSE.

These objectives enhance the understanding of PULSE's impact on underwater noise and address the following main research question:

To what extent does PULSE influence radiated underwater noise and interact with other mitigation measures such as air-bubble curtains?

The current most common method for installing monopiles is impact hammering. Therefore, this research focuses on this method, excluding other installation techniques such as vibratory devices or GDP. By narrowing the scope to impact hammering, a detailed exploration and analysis of this method and its associated noise mitigation measures is possible. It enables a focused study of the specific characteristics of noise produced by impact hammers, such as the amplitude and frequency of the sound waves.

To address the noise generated by impact hammers, various mitigation measures have been developed. This research examines two specific measures: PULSE, which targets noise mitigation at the source, and air-bubble curtains, which focuses on noise mitigation along the transmission path. Other mitigation measures, although significant, are excluded from this study due to the extensive time required to model them sufficiently. Nonetheless, recommendations are provided on how an HSD-system can be integrated into the model, acknowledging its widespread use in OWF projects.

Furthermore, the study is confined to the installation of monopiles in shallow waters, specifically up to 50 meters in depth. This limitation is driven by two main factors: (i) the practicality and economic feasibility of installing OWTG foundations beyond certain depths, as deeper installations become increasingly large and costly; and (ii) the availability of field data for monopiles installed within this depth range.

1.4. Approach and methodology

This study is organised into six chapters to address the research question and accompanying objectives. Chapter 1 introduces the problem statement, research gap, objectives, and methodology. Chapter 2 provides an overview of relevant literature and previous research, discussing fundamental acoustic principles, the interaction between the monopile, water, and soil, the basic principles of PULSE and air-bubble curtains, and a brief history of computational methods for predicting underwater noise. The model used in this study to predict underwater noise due to offshore pile driving is presented in Chapter 3. This chapter discusses the two modules of the model: the sound generation module and the sound propagation module. It includes the governing equations, boundary and interface conditions, and the coupling of these modules. Next, Chapter 4 explains how the mitigation measures, PULSE and air-bubble curtains, are modelled and incorporated into the underwater noise prediction model. Chapter 5,

the most extensive chapter, compares the model's results with field data provided by Van Oord. Once a fair correspondence is established, the chapter discusses the monopile's response to different PULSE settings. It analyses the results of various PULSE settings with and without different configurations of air-bubble curtains, both quantitatively by comparing sound levels and qualitatively by analysing the frequency response. Additionally, it presents the energy introduced into the water and soil for different PULSE settings and the insertion losses for all analysed cases. Finally, Chapter 6 reflects on the model's results, presenting discussions and conclusions based on the study's outcomes. The chapter wraps up with recommendations for further research regarding the research objectives and question. The general report outline is displayed graphically in Fig. 1.1.

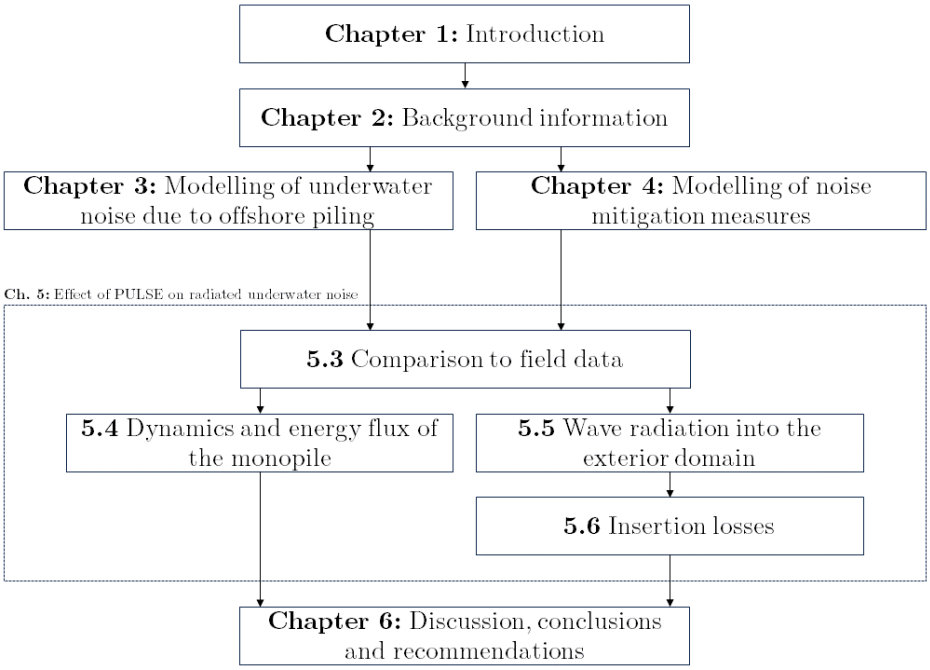

Figure 1.1: General outline of the report.

2

Background information

2.1. Fundamental acoustic principles

Understanding the fundamental acoustic principles requires an exploration of the nature of sound and vibrations. Sound, ever-present in our environment, plays a crucial role underwater, travelling long distances and affecting marine life significantly. Sound can be considered as a vibration[1] that propagates as an acoustic wave through mediums like seawater or soil [16]. Sound is generated primarily from vibrating structures, such as monopiles during installation. However, in the form of noise, sound can cause adverse effects on the physiological and psychological well-being of underwater marine life.

2.1.1. Sound waves

Sound propagates through water in the form of waves known as sound waves. In this process, energy is transmitted through the medium, such as water, via fluctuations in pressure. It is important to emphasise that there is no transfer of matter; rather, energy is transferred through the vibrations of the particles in the medium. When a sound wave travels from one medium to another (e.g., from seawater to soil or vice versa), it can transmit or reflect, depending on the impedance mismatch [29]. This mismatch arises when there are differences in the density and/or speed of sound between the two mediums. The following section elaborates on the concept of acoustic impedance.

2.1.2. Acoustic impedance

Acoustic impedance is a measure of the opposition that a medium offers to the propagation of sound waves [29]. In simpler terms, it quantifies the resistance a sound wave encounters as it travels through a medium. Acoustic impedance is typically denoted by the symbol Z and is measured in Rayls per square meter or Pascal seconds per cubic meter (Pa s/m^3). Eq. (2.1) provides the formula for calculating acoustic impedance. In the linear regime, the acoustic impedance of a fluid medium is determined by the product of the medium's density (ρ) and the speed of sound within it (c_f).

$$Z = \rho \, c_\mathrm{f} \tag{2.1}$$

2.1.3. Sound pressure

Sound pressure, or acoustic pressure, refers to the deviation in local pressure from the ambient pressure, induced by a sound wave [39]. This pressure variation can be captured using a hydrophone. The standard (SI) unit of measurement for sound pressure is the Pascal (Pa). An illustration in Fig. 2.1 depicts a typical sound wave.

[1] Commonly considered to be disturbances of solids or structures, such as monopiles.

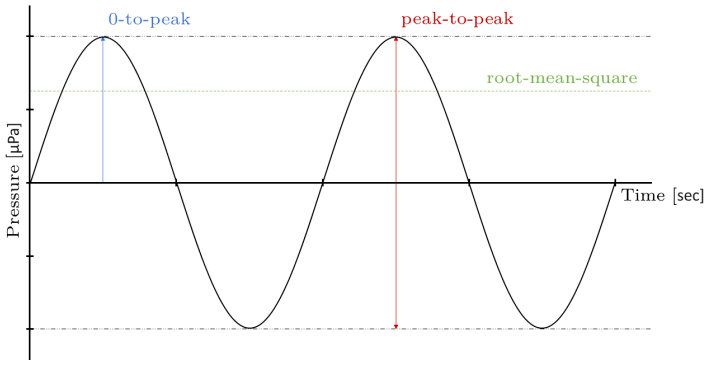

Figure 2.1: A simple sound wave and three common methods used to characterise the loudness of a sound signal.

Characterising the loudness of a sound signal can be approached through different common methods. The simplest methods describe the wave by its peak and peak-to-peak pressure. Peak pressure, also known as 0-to-peak pressure, signifies the range between zero pressure and the maximum positive pressure of the signal. Peak-to-peak pressure, on the other hand, represents the span between the most negative[2] and most positive pressures of the signal, both of which are deviations from the ambient pressure.

A more sophisticated approach to characterising sound waves involves root-mean-square pressure (p_{rms}), which calculates the square root of the average of the pressure ($\overline{p^2}$) squared over a specified duration [17]. Eq. (2.2) illustrates the calculation process for p_{rms}, where $p(t)$ represents the sound pressure deviation from the ambient pressure at time t.

$$p_{\mathrm{rms}} = \sqrt{\overline{p^2}} = \sqrt{\lim_{T\to\infty} \frac{1}{T} \int_0^T p^2(t)\mathrm{d}t} \tag{2.2}$$

Given the fluctuations in sound waves, the most widely used indicator of acoustic wave strength is the sound pressure level (SPL). SPL is defined [37] as the logarithmic measure of the root mean squared sound pressure (p_{rms}) relative to a reference value (p_{ref}). Denoted as L_{p}, SPL is expressed by Eq. (2.3), with the reference value being a medium-dependent pressure, typically set at 10^{-6} Pa in water.

$$L_{\mathrm{p}} = 20\log_{10}\left(\frac{p_{\mathrm{rms}}}{p_{\mathrm{ref}}}\right) = 10\log_{10}\left(\frac{p_{\mathrm{rms}}^2}{p_{\mathrm{ref}}^2}\right) \tag{2.3}$$

2.1.4. Acoustic intensity

Another important acoustical parameter is the acoustic intensity, representing the average flow rate of energy through a unit area normal to the propagation direction [29]. The magnitude of the instantaneous intensity of a plane wave at a specified position is

$$I(t) = \frac{p^2(t)}{Z} = \frac{p^2(t)}{\rho\ c_{\mathrm{f}}} \tag{2.4}$$

and the time-averaged acoustic intensity, denoted as I, can be determined as

$$I = \frac{1}{T}\int_0^T I(t) = \frac{p_{\mathrm{rms}}^2}{Z} = \frac{p_{\mathrm{rms}}^2}{\rho\ c_{\mathrm{f}}} \tag{2.5}$$

Eq. (2.5) computes the acoustic intensity by dividing the root-mean-square pressure (p_{rms}), derived in Eq. (2.2), by the acoustic impedance, obtained from Eq. (2.1) [29].

[2] In acoustics, negative acoustic pressure occurs during the rarefaction phase of a sound wave when the pressure drops below the ambient pressure level. This relative concept indicates that the acoustic pressure is lower than the average ambient pressure, not that it is absolutely below zero.

2.1.5. Decibel scale

The decibel (dB) is the dominant unit in underwater acoustics and is a relative unit that is based on the ratio of two values (i.e., sound pressure, intensity) on a logarithmic scale [50]. The decibel scale makes it easier to deal with very large and small numbers, simplifies the mathematical operations (i.e., addition in dB scale instead of multiplication in linear scale), and provides smooth visual representation. Expressed as a formula, the intensity level of a sound in decibels is

$$\text{Level} = 10\log_{10}\left(\frac{X}{X_{\text{ref}}}\right) \tag{2.6}$$

where X represents the intensity of a sound, while X_{ref} denotes the intensity of a reference sound. For instance, doubling the intensity of a sound corresponds to an increase of a little more than 3 dB.

$$\text{Level} = 10\log_{10}\left(\frac{2X}{X}\right) = 10\log_{10}(2) \approx 3 \text{ dB}$$

2.1.6. Sound Exposure Level

The Sound Exposure Level (SEL) quantifies the total sound energy over a given period of time [16]. It is denoted in decibels (dB) and is commonly used to describe the noise exposure of individuals (or communities) to distinct noise occurrences. The standard averaging period typically spans one second. Within the maritime sector, SEL refers to the potential effects of human-generated sounds (e.g., from impact hammering) on marine biodiversity and aquatic species. SEL computation utilises Eq. (2.7), with the reference pressure (p_{ref}) set at 10^{-6} Pa in water.

$$\text{SEL} = 10\log\left(\int_{T_1}^{T_2}\frac{p^2(t)}{p_{ref}^2}dt\right) \quad \text{dB re } 1\mu\text{Pa}^2\text{s} \tag{2.7}$$

2.1.7. Peak Pressure Level

The Peak Pressure Level (L_{peak}) represents the highest instantaneous sound pressure value at a specific time, expressed in decibels (dB). This value is, just as SEL, relative to the reference pressure (p_{ref}).

$$L_{peak} = 20\log\left(\frac{\max|p(t)|}{p_{ref}}\right) \quad \text{dB re } 1\mu\text{Pa} \tag{2.8}$$

2.2. Pile-water-soil interaction

This section delves into the underwater noise generated during impact piling for offshore monopile installation. It explores the dynamics of pile-water-soil interaction, focusing on compressional waves and the formation of Mach cones. The role of Scholte waves, emerging from the seabed-water interface, as a secondary noise source, is also discussed. Additionally, the presence of shear waves in the seabed is discussed.

2.2.1. Pile dynamics

As mentioned in Section 1.3, impact piling is the most common technique for monopile installation. This method involves an impact hammer, typically composed of two primary elements: an impact weight and an anvil. The process begins with the impact weight repetitively falling onto the anvil positioned on the pile head to drive the monopile into the seabed. This action increases stress in the contact area between the pile and the ramming hammer, leading to the deformation of the pile material and transmitting energy from the impact hammer to the monopile, progressively achieving the final penetration depth [33]. During this impact, an axial compressional wave travels with a speed c_p[3] defined as:

$$c_p = \sqrt{\frac{E}{\rho}} \tag{2.9}$$

[3]The wave speed mentioned here is predicted by the wave equation, which approximates the wave speed in a monopile. This approximation is reasonable for low frequencies, where the wavelengths are long compared to the material's microstructure, but not for very high frequencies due to short wavelengths and the effects of dispersion, material anisotropy, and other complex behaviours not accounted for in the simple wave equation.

where E is the modulus of elasticity, and ρ is the mass density. Due to Poisson's contraction, this axial compressional wave causes radial expansion of the monopile, as illustrated in Fig. 2.2a. The compressional wave propagates downward, pushing the monopile into the seabed. If the material parameters presented in Eq. (2.9), as well as the cross-sectional shape and area of the pile A, remain unchanged, the wave will always propagate further towards the pile toe. However, if there is a change in the dynamic stiffness, represented by the pile or mechanical impedance Z_{pile}, parts of the wave will be reflected and travel in the opposite direction back towards the pile head. Depending on the resistance encountered, either a tension or compression wave reflects at the pile toe. The pile impedance Z_{pile} is determined by the following equation:

$$Z_{pile} = A \cdot \rho \cdot c_p \tag{2.10}$$

In the initial blows, when the soil is relatively loose, low resistance is assumed, leading to a tension wave propagating towards the top of the pile, as depicted in Fig. 2.2b, thereby resulting in a reduction of the radius. The proportion of reflected and transmitted wave components depends on the degree of impedance change. The greater this change, or the stronger the change in pile impedance, the more components are reflected, and the fewer components of the strain wave are transmitted [52].

It is important to note that this pile impedance Z_{pile} is different from acoustic impedance Z, which describes the resistance to sound waves in a fluid medium, as discussed in Section 2.1.2. Pile impedance of a monopile reflects its resistance to mechanical vibrations and wave propagation, considering the material's elastic properties and cross-sectional area.

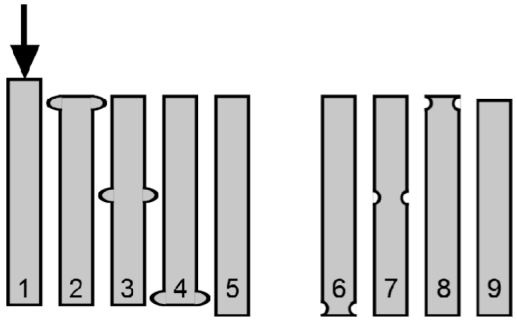

Figure 2.2: Schematic representation of wave passage in a driven pile. After the wave is initiated at the pile head (1), it travels down the pile as a compressional wave from top to bottom (2-4). Assuming a free bearing condition - a condition implying that the pile toe is free to move or displace without any resistance - the wave reflects at the pile toe (5) as a tension wave, which then travels through the pile from bottom to top (6-8). After this process, the pile is at rest and fully embedded in the soil (9) [33].

2.2.2. Energy introduced into the water and soil

The energy transfer through the pile to the water due to the hammer impact can be categorised into two main types: (i) energy that is directly radiated into the surrounding fluid region in the form of Mach cones, coming from the vibrations of the shell's surface, and (ii) energy carried by Scholte waves, which travel along the interface between the soil and water, inducing low-frequency pressure fluctuations near the seabed. The first category can be considered as a primary noise source and the latter can be considered as a secondary noise source [60]. This distinction is crucial due to several key differences:

- **Frequency content:** Mach cones encompass energy across the frequency spectrum, while Scholte waves predominantly carry energy at lower frequencies ($f < 100$ Hz).
- **Depth distribution:** Scholte waves' influence is confined to the proximity of the seabed, whereas Mach cones span the entire water layer.
- **Wave speeds:** Mach cones propagate in the fluid region at 1500 m/s, equivalent to the speed of sound, while Scholte waves propagate at significantly lower speeds below the shear wave speed in the soil region [60].

The primary noise source arises from the fact that the downward wave speed in the monopile due to the impact hammer exceeds the speed of sound in the surrounding water. These compressional waves, known as Mach cones, propagate at an angle in the surrounding water, a value that can be calculated using Eq. (2.11), where φ_w represents the angle between the monopile and the downward-propagating Mach cone, c_w signifies the speed of sound in water, and c_p denotes the speed of sound of the downward-propagating compressional wave in the monopile.

$$\varphi_w = \sin^{-1}\left(\frac{c_w}{c_p}\right) \tag{2.11}$$

When the compressional wave reaches the soil domain, Mach cones appear due to the vibrating monopile, but this time at a different angle, as the wave speed in the soil differs from that in the water. This phenomenon is termed rarefaction [52]. The angle at which the Mach cones propagate in the soil domain (φ_s) can be calculated using Eq. (2.12), where c_s signifies the speed of sound in the soil.

$$\varphi_s = \sin^{-1}\left(\frac{c_s}{c_p}\right) \tag{2.12}$$

Upon reaching the pile toe, the compressional wave reflects due to an impedance mismatch between the steel of the monopile and the underlying soil [52]. As mentioned earlier, the reflected wave travels upward as a tension wave, leading to a reduction in the radius. These upward tension waves give rise to Mach cones moving upwards. The angle of these Mach cones can be calculated using the same formula as the downward-propagating Mach cones in the soil, i.e., Eq. (2.12). Upon reaching the water domain again, upward-propagating Mach cones in the water column are created, under an angle similar to that in Eq. (2.11), due to the impedance mismatch between the soil layer and the water layer. Fig. 2.3 provides an overview of the compressional wave and tension wave in the monopile, along with the resulting Mach cones in both the water and soil layer.

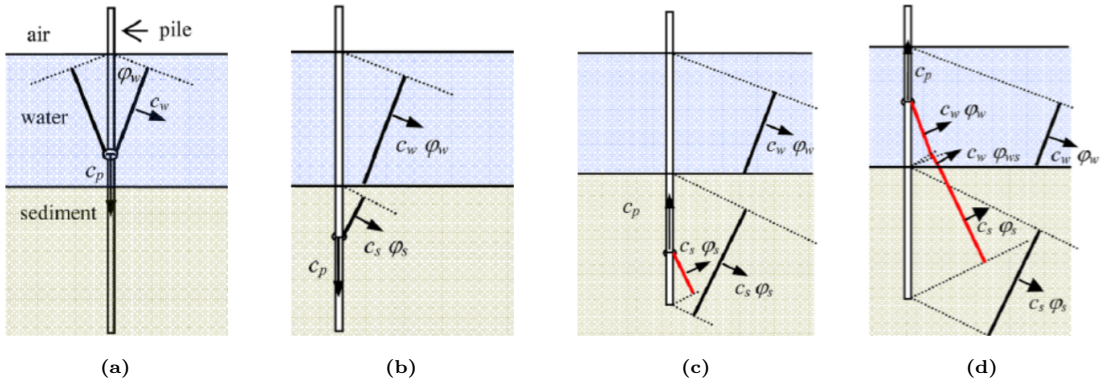

Figure 2.3: Mach cone generation caused by compression and tension wave in a monopile: (a) downward-propagating Mach cone in the water layer, (b) downward-propagating Mach cone in the soil layer, (c) upward-propagating Mach cone in the soil layer, and (d) upward-propagating Mach cone in the water layer.

In addition to the Mach cones, shear waves with nearly vertical polarisation, resulting from the substantial difference in wave speeds between the soil and monopile, are present in the soil, as outlined in a study by Tsouvalas [60]. Both wave types can be named body waves, as these waves propagate spherically in an infinitely large solid. The secondary noise source, known as Scholte waves, arises from the waves at the boundary between the seabed and water. These waves travel at a slower speed compared to the shear waves within the soil and experience less attenuation in intensity, as their energy remains concentrated near this boundary. Since they travel near the seabed-water interface, their impact on pressure fluctuations is significant near the seabed but diminishes as they propagate further into the water column [60]. Next to these Scholte waves, there exists Stoneley waves, which are also interface waves, that travel at the soil-soil interface. Fig. 2.4 schematically shows the different types of waves in the soil (half)space.

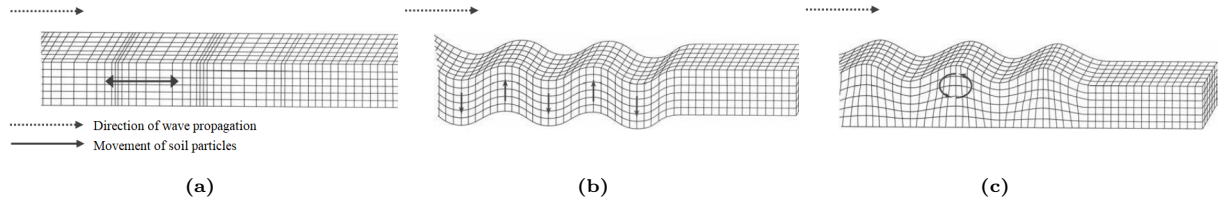

Figure 2.4: Different types of waves: (a) compression wave, (b) shear wave, and (c) interface wave.

2.3. Relevant mitigation measures

2.3.1. Mitigation by PULSE

The primary focus of this research is to investigate the effects of PULSE on monopile vibrations and radiated underwater noise, addressing the current lack of literature on this technique. This section delves into the fundamental principles and claimed advantages by the manufacturer of PULSE.

Fundamental principle of PULSE

PULSE is an add-on to the pile-driving hammer, positioned between the hammer and the sleeve (anvil), functioning as a spring-damper system. It acts as an intermediary component between the impact hammer and the monopile, consisting of two primary hydraulic pistons – a top piston and a bottom piston – separated by a fluid medium [26]. This fluid medium is crucial for the functioning of the PULSE system as it enables the adjustment of impact characteristics. Fig. 2.5 illustrates how PULSE works. Fig. 2.5a shows the two hydraulic pistons without the fluid medium, while Fig. 2.5b depicts PULSE with fluid between the pistons. Fig. 2.5c provides a rendered image of the PULSE system. The following is a detailed analysis of PULSE's mechanism:

1. **Impact energy distribution over time:** When the hammer strikes the top piston of PULSE, the force is transmitted through the fluid medium to the bottom piston, which is in contact with the monopile. The presence of the fluid medium elongates the contact time between the hammer and the monopile, distributing the force over a longer duration. According to the principles of impulse and momentum, this increased contact time allows the same amount of impulse to be delivered with a reduced peak force. The fluid medium, typically incompressible or nearly incompressible, gradually transfers the impact energy and creates a hydraulic cushioning effect. The rate of energy transfer depends on the fluid properties, which can be adjusted to control the flow rate. This prolonged contact time helps spread the impact energy more evenly, reducing the peak force transmitted to the monopile [5].
2. **Hydraulic damping:** The fluid medium between the pistons acts as damping. The fluid volume can be adjusted to control the system's damping characteristics. Increasing the fluid volume enhances the damping effect, resulting in greater noise reduction. Conversely, reducing the fluid volume decreases the damping effect. This adjustability allows for flexible control over the impact characteristics, making it possible to tailor the system for specific conditions and requirements.
3. **Energy absorption and dissipation:** The fluid absorbs and dissipates some of the impact energy as heat, reducing the energy transferred to the monopile and thereby lowering the overall noise generated. Thus, as this heat dissipation leads to energy losses, additional input energy is required to maintain the same energy transfer as operations without PULSE.
4. **Reduction of radiated noise:** By elongating the impulse duration and reducing the peak force, PULSE effectively lowers the radiated noise generated during pile driving [5]. This noise reduction is crucial for reducing the environmental impact on marine life, which is sensitive to underwater noise.

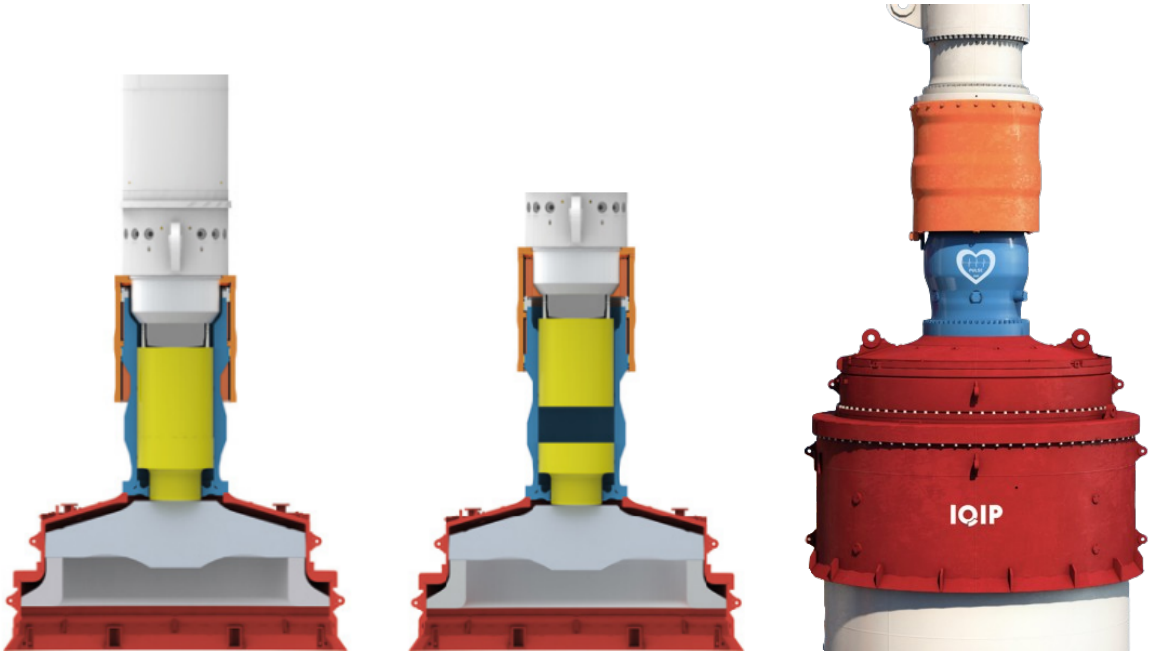

(a) (b) (c)

Figure 2.5: Different representations of PULSE: (a) schematic overview of PULSE without fluid medium, (b) schematic overview of PULSE with fluid between the pistons, and (c) rendered image of PULSE [25, 26]

Advantages of PULSE

According to IQIP [25], PULSE offers several major advantages:

- 6–10 dB reduction in SEL.
- 5–12 dB reduction in L_{peak}.
- Adjustable damping levels by varying the liquid volume in PULSE.
- Up to 60% reduction in fatigue damage to the monopile.
- Comparable installation time to traditional methods.

These statements are provided by IQIP, the manufacturer of PULSE. Due to the lack of extensive scientific research on PULSE, validating these statements poses a challenge. For new projects, a 4-6 dB reduction in SEL is assumed [13], a revision from the previously stated 6-10 dB reduction. This study aims to investigate these statements, focusing particularly on the effectiveness of PULSE in combination with air-bubble curtains and its behaviour across the frequency spectrum. The investigation of fatigue damage falls outside the scope of this research.

2.3.2. Mitigation by air-bubble curtains

Air-bubble curtains are a preferred solution for noise mitigation due to their ease of application and efficiency. They entail rising air bubbles forming a closed curtain around the monopile to reduce noise transmission. These air bubbles are created by compressed air injected through perforated hoses positioned horizontally on the seabed [63]. To achieve uniform pressure distribution along the hose, the nozzle opening's diameter should ideally increase from the feed points [34]. However, this is not practically feasible. The hoses are laid on the seabed by a hose deployment vessel equipped with compressors to supply air to the hoses. Adequate air volume streams must be provided, with greater depths requiring increased air volume streams (and consequently more compressors) due to the compressibility of air bubbles. Air-bubble curtains with larger radii experience a notable decrease in flow velocity at locations farther from the air feeder [46], as depicted in Fig. 2.6a. As the air bubbles rise, their volume expands, and eventually, they split. One challenge, particularly in greater depths, is the drift of bubbles due to currents [34].

Air-bubble curtains can be divided into two main types. One such type is the Little Bubble Curtain (LBC), which has the bubbly layer positioned near the pile. However, these LBCs have only been used in experimental settings and are not developed for commercial applications [4]. The more commonly used type is the Big Bubble Curtain (BBC), which comes in single, double (DBBC), or triple (TBBC) configurations.

Fundamental principle of air-bubble curtains

The fundamental principle of air-bubble curtains involves creating a barrier of rising air bubbles that effectively attenuates underwater noise. The following provides a detailed analysis of the mechanisms by which air-bubble curtains achieve noise reduction:

1. **Impedance mismatch:** One of the key principles behind the effectiveness of air-bubble curtains is the impedance mismatch between the bubbly layer created by the rising air bubbles and the surrounding water. The bubbly layer has a significantly different acoustic impedance compared to water, leading to reflections and scattering of sound waves at the interface between the two mediums [63]. This impedance mismatch causes a portion of the sound energy to be reflected back towards the source, reducing the amount of sound that propagates through the water. This mechanism is particularly effective at attenuating a broad range of frequencies, contributing to overall noise reduction.
2. **Scattering and absorption:** The bubbles in the air-bubble curtain act as scatterers that disrupt the propagation of sound waves. As sound waves encounter the bubbles, they are scattered in various directions, which diffuses the sound energy and reduces its intensity [49]. Additionally, the bubbles can absorb sound energy, especially when the frequency of the sound wave is close to the resonance frequency of the bubbles. At resonance, bubbles oscillate more strongly, converting sound energy into thermal energy, which is then dissipated [49]. This absorption mechanism is highly effective for high-frequency noise reduction.
3. **Bubble dynamics:** The size and distribution of bubbles within the air-bubble curtain play a crucial role in its effectiveness. Smaller bubbles resonate at higher frequencies, while larger bubbles resonate at lower frequencies. By carefully controlling the size and distribution of the air bubbles, air-bubble curtains can be optimised to target specific frequency ranges for noise reduction [63].
4. **Mitigation of waves from the soil:** In addition to attenuating direct sound waves, air-bubble curtains also mitigate waves coming from the soil, such as Mach cones generated in the seabed. When these waves re-enter the water at specific distances, they contribute to underwater noise. The presence of an air-bubble curtain disrupts the transmission of these waves, reducing their impact on underwater noise levels [52]. Proper positioning and configuration of the air-bubble curtain can effectively intercept and dissipate these waves, enhancing the overall noise mitigation performance. This concept is visualised in Fig. 2.6b.

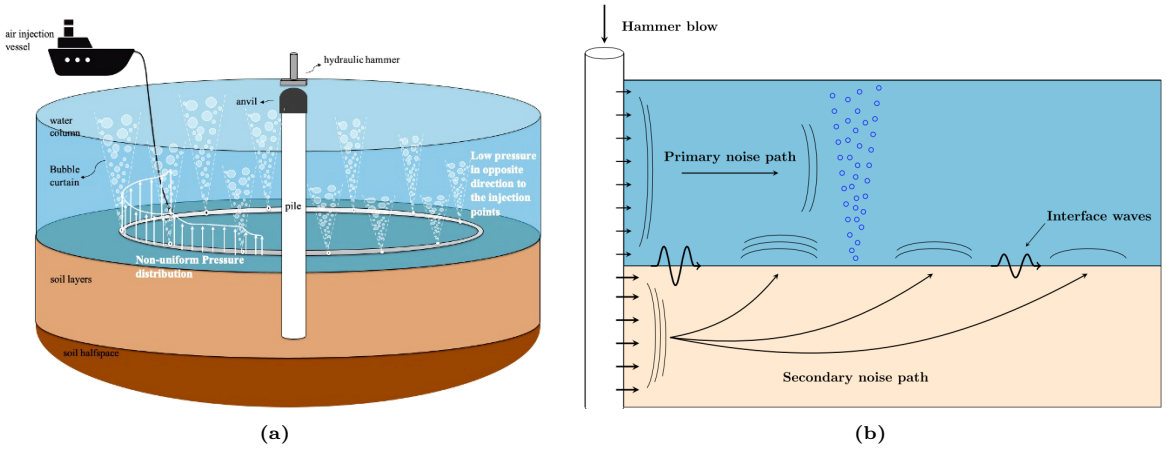

Figure 2.6: Schematic representation of an air-bubble curtain: (a) illustrates the non-uniform pressure distribution in the hose [46], while (b) demonstrates the operational principle of an air-bubble curtain, clearly showing the mitigation of pressure waves [7].

Advantages of air-bubble curtains

Air-bubble curtains offer several significant advantages in the context of underwater noise mitigation during pile-driving operations.

1. **Effective noise reduction:** Air-bubble curtains can achieve substantial reductions in SEL and L_{peak}. Research by Koschinski et al. [34] shows that a BBC can reduce SEL by up to 15 dB at a distance of 750 meters from the source, and a DBBC can achieve reductions by up to 18 dB. It is important to note that the claimed reductions in SEL are not systematically documented in the literature, with only a few exceptions [46, 49, 59]. Comparisons are often clustered together for varying soil conditions, pile sizes, and dissimilar environmental settings, making direct comparison difficult.
2. **Adaptability:** Air-bubble curtains are versatile and can be tailored to different operational conditions. The size of the air-bubble curtain, the rate of air volume injection, and the configuration of the nozzles can be adjusted to optimise performance for specific sites and depths [46].
3. **Operational efficiency:** Air-bubble curtains can be deployed quickly and efficiently. The setup involves laying hoses on the seabed and connecting them to compressors on a pipe-laying vessel. These hoses can be pre-laid and recovered after the installation, ensuring there is no adverse influence on the cycle time. Once in place, the system can operate continuously to provide ongoing noise reduction during pile-driving operations [63].

These advantages make air-bubble curtains a practical and effective solution for mitigating underwater noise generated during pile-driving operations. The ability to adapt to different conditions and provide significant noise reduction highlights their importance in mitigating noise.

2.4. A brief history in computational methods

The prediction of wave propagation in shallow waters is more complicated than the well-documented underwater noise in deep oceans, due to multiple reflections, refractions and scattering of sound waves, as was seen in Section 2.2.2. Next to these complications, another complexity arises due to the three interrelated domains: seawater, seabed and pile. In the next sections, different models are discussed which were developed in the past to tackle this complex problem. These sections are based on research conducted by Tsouvalas [59].

2.4.1. First generation models

Reinhall and Dahl [52] were pioneers in developing a numerical model, see Fig. 2.7a, to predict underwater noise resulting from impact pile driving. Their approach involved two key steps: firstly, employing a finite element model (FEM) to accurately capture the sound generation mechanism with detailed modelling of the source. Perfectly matched layers (PMLs)[4] are used to truncate the domain in FEM. Secondly, the parabolic equation (PE) method is utilised to simulate the propagation of sound over larger distances. The PE method simplifies the wave equation under the assumption of predominantly forward propagation, making it computationally efficient for long-range sound propagation modelling. It is noteworthy that both the fluid and soil are treated as acoustic fluids in these models, although this approximation is less precise for the soil layer. The key finding of this model was the identification of Mach cones, as visualised in Fig. 2.7b, in the pressure field near the monopile, due to supersonic compressional stress waves propagating from the monopile head to the toe and back after the hammer impact.

[4] PMLs are artificial absorbing layers used in numerical simulations to truncate computational domains. They are designed to absorb incoming waves from the interior of the computational domain and prevent artificial reflections at the boundaries, thereby simulating an infinite domain. While they are highly effective, they introduce a small error due to the imperfect absorption of waves. This error is generally minimal compared to the benefits of preventing reflections.

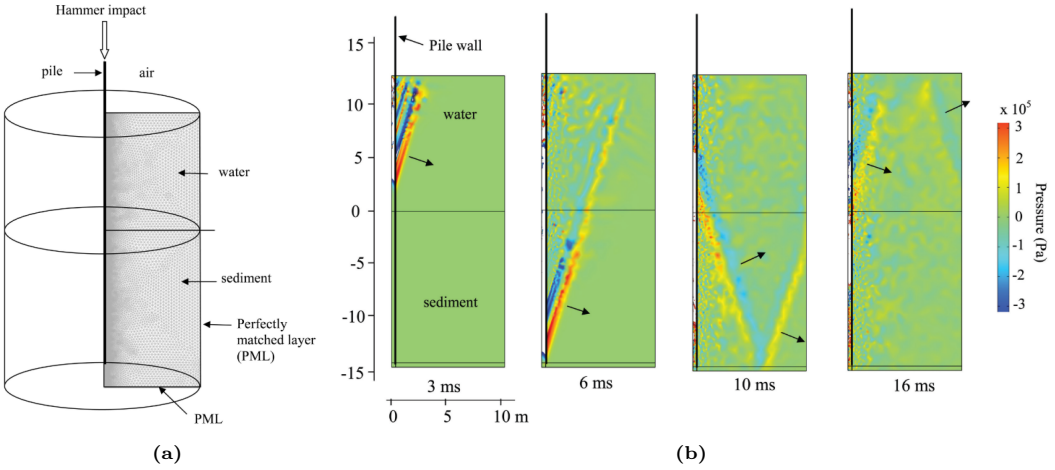

Figure 2.7: (a) An axisymmetric FE model showing the pile, acoustic fluids, and PML, and (b) the pressure field surrounding the monopile, displaying prominent Mach cones with arrows indicating their propagation direction [52]. The pressure field visualisations are 2D slices of the axisymmetric model, not 3D wedges.

Following Reinhall and Dahl's work [52], subsequent studies, which can be a review on underwater noise by Tsouvalas [59], adopted a similar FEM-PE approach for sound generation and propagation prediction. MacGillivray [38] explored a finite difference (FD) scheme for near-field acoustics, simplifying assumptions for shell surface energy. Other models [40, 41, 42] coupled finite elements for the structure and boundary elements for the soil, with a focus on soil vibrations near the pile.

Semi-analytical solutions emerged as an alternative modelling method, offering computational efficiency for larger-scale simulations. These models, exemplified by Tsouvalas and Metrikine [61], involve the shell theory for the pile, linearised acoustic fluid for water, and distributed springs and dashpots for soil representation. In this model, a mode-matching technique is utilised to solve the coupled problem.

2.4.2. Second generation models

The first generation models shed light on how underwater sound is produced during impact piling. However, they come with limitations, particularly in representing the seabed. They often simplify the seabed as either an acoustic medium or with spring-dashpot elements. These approaches do not fully capture the complex physics of the problem.

These simplifications pose two main challenges: (i) a significant amount of energy is released into the seabed during pile driving, requiring a detailed understanding of the seabed dynamics alongside seawater, and (ii) accurately determining the amplitude of the acoustic source needs a comprehensive understanding of the coupled problem.

Tsouvalas et al. [62] pioneered efforts in integrating the seabed's elastic properties into pile driving acoustics, as can be seen in Fig. 2.8a. Their work revealed that during offshore pile installations, the seabed mainly responds with vertically polarised shear waves, caused by pulses travelling through the pile at supersonic speeds. Alongside these, compressional waves similar to those in seawater are observed within the seabed. Furthermore, Scholte waves originating at the seabed-water interface travel considerably slower than the compressional waves. The results displayed in Fig. 2.8b depict the various types of waves identified by the model. These results have been substantiated by later studies and experiments, affirming the accuracy of the model's predictions.

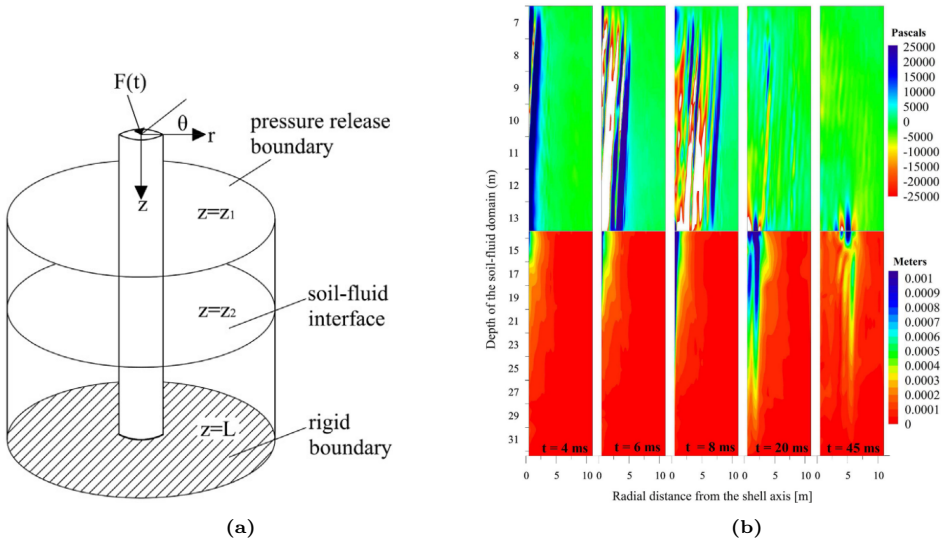

Figure 2.8: (a) An axisymmetric semi-analytical model showing the pile, fluid as an inviscid compressible medium, and soil as an elastic continuum, and (b) the pressures in the fluid and the displacement in the soil for different time moments after the impact. The Mach cones in the fluid and almost vertically polarised shear waves in the soil can be recognised, as well as the Scholte waves at the water-seabed interface [62].

2.4.3. The state-of-the-art

Presently, various approaches are available for modelling sound in the context of underwater acoustics. These models can be grouped based on the level of detail in representing the sound source and its surrounding environment. The simplest among these are the state-of-the-art empirical models, which define the acoustic source primarily by a sound level without providing an explicit geometry description. In this method, the initial sound level is then projected over greater distances using a transmission loss formula.

In addition to empirical models, there exists a semi-analytical and numerical approach. The semi-analytical method addresses the challenge in two distinct phases. Initially, a close-range module is employed to generate the wave field near the pile. Subsequently, a far-range module takes over to propagate the sound to larger distances. Both modules are coupled through a boundary integral at the interface. The dynamics of the monopile are characterised using classical shell theories.

Numerical solution techniques use traditional finite element packages or finite difference schemes to create the acoustic field surrounding the pile. Following this, the wave field undergoes propagation using a sound propagation model as described in Section 2.4.1. The semi-analytical method will be extensively discussed in the subsequent chapter, as it serves as the foundation for the SILENCE software, upon which this research is based.

3

Modelling of underwater noise due to offshore pile driving

In the previous sections, various models have been explored aimed at understanding underwater noise. This chapter delves into a state-of-the-art semi-analytical model developed by Tsouvalas et al. [49, 60], offering computational efficiency in predicting the generation and propagation of sound fields resulting from impact piling, especially at significant distances from the pile. The model comprises two main modules:

1. **Sound Generation Module:** This module intricately captures the interactions between the pile, water, and soil.
2. **Sound Propagation Module:** Dedicated to tracing the propagation of the wavefield at greater distances from the pile.

The system's overall configuration includes a monopile, a hydraulic hammer, and the surrounding fluid and soil media. For the fluid and soil, a cylindrical coordinate system (r, ϕ, z) is adopted, where z denotes positive downward and r signifies positive direction away from the pile. Due to the assumed axisymmetric model, the displacement in the ϕ-direction is zero [49].

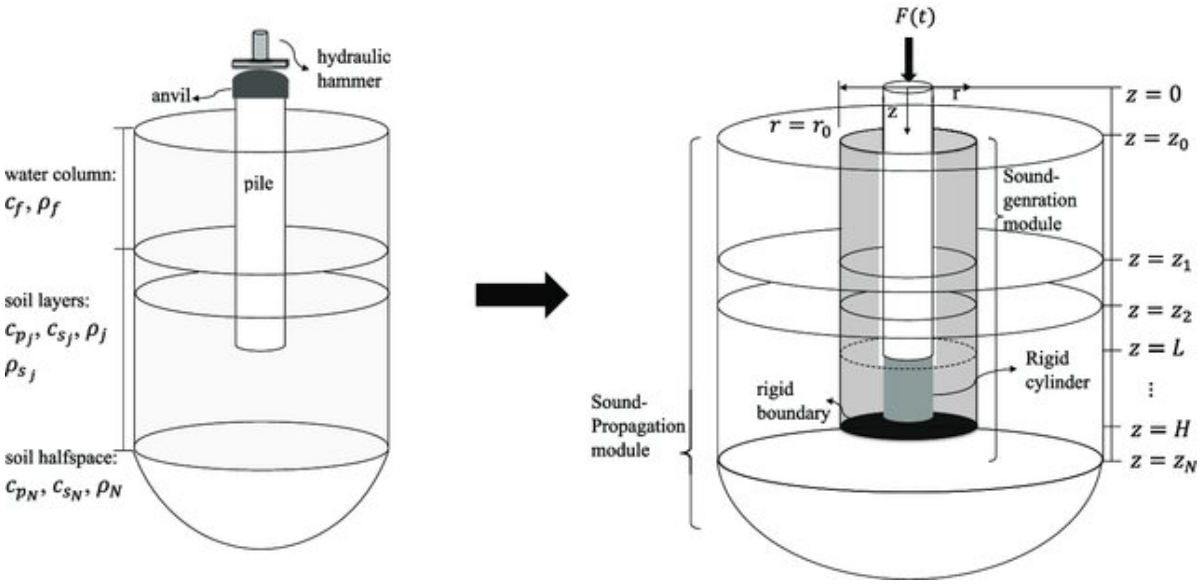

Figure 3.1: Schematic representation of the modelled system. r_0 is the radial distance of the coupled cylindrical surface, z_0 is the level of the sea surface, z_1 is the level of the seabed, z_j is the bottom level of $j-1$th soil later, L is the level of the bottom of the pile and H is the level of the rigid boundary in the sound generation module [49].

Fig. 3.1 provides an overview of the modelled system. Key assumptions include:

- **Exclusion of fluid and soil inside the pile:** This assumption, based on studies by Tsouvalas and Metrikine [61], indicates that internal fluid and soil do not significantly impact the pile's vibration or the energy radiated into the surrounding medium. The inner fluid can absorb a minor portion of the input energy, leading to slightly lower pressure levels outside the pile. Consequently, excluding the internal fluid might result in an almost negligible overestimation of sound levels in the surrounding medium. For frequencies above $2.2f_r$[1], the difference in pressure levels between an empty and fluid-filled pile becomes negligible [61].
- **Rigid cylinder:** A rigid cylinder, which has the same radius as the pile and is situated at a height $H - L$ below the pile tip, facilitates the use of a semi-analytical solution. This rigid baffle effectively eliminates the radiation of elastic waves from the pile tip into deeper soil layers, ensuring minimal influence on elastic wave propagation in shallow soil layers near the seabed [49];
- **Hydraulic hammer:** The hydraulic hammer and anvil are modelled as an external force applied at the top of the pile ($z = 0$) [49].

In this model, the Fourier transform pair to analyse quantities $F(t)$ such as shell displacement, soil stresses, or fluid pressure, is defined as:

$$F(t) = \frac{1}{2\pi}\int_{-\infty}^{\infty} \tilde{F}(\omega)e^{-i\omega t}d\omega \quad \text{and} \quad \tilde{F}(\omega) = \int_{-\infty}^{\infty} F(t)e^{i\omega t}dt \tag{3.1}$$

The symbols used in the Fourier transform pair are explained as follows:

- $F(t)$: This represents the original time-domain function. It could be the shell displacement, soil stress, or fluid pressure at that particular time.
- $\tilde{F}(\omega)$: This represents the Fourier transform of the function $F(t)$ at a specific angular frequency ω. It is the frequency domain representation of the time-domain function $F(t)$.
- t: This is the time variable in the time-domain function $F(t)$.
- ω: This is the angular frequency variable in the Fourier transform. It is related to the frequency f by $\omega = 2\pi f$.
- i: This represents the imaginary unit, where $i = \sqrt{-1}$.

After applying the forward Fourier transform, the governing equations in the frequency domain, which are discussed later in this section, are obtained. This Fourier transform pair ensures the analysis of the behaviour of the system across different domains, providing valuable insights into underwater noise prediction and wave propagation.

3.1. Sound Generation Module

This section introduces the partial differential equations that govern the dynamic behaviour of the coupled system comprising the shell structure and the acousto-elastic media. The dynamic response of the shell structure is described by a linear high-order shell theory, as established by Kaplunov et al. [31]. The fluid component is characterised as a three-dimensional inviscid compressible medium, while the soil component is represented as a three-dimensional elastic continuum [62].

3.1.1. Governing equations and fundamental solutions

Shell vibrations

The dynamic response of the coupled system, consisting of the shell structure and the acousto-elastic media, is governed by the following set of coupled partial differential equations:

$$\mathbf{L}\mathbf{u} + \mathbf{I}\ddot{\mathbf{u}} = -\left(H\left(z - z_1\right) - H(z - L)\right)\mathbf{t}_s + \left(H\left(z - z_0\right) - H\left(z - z_1\right)\right)\mathbf{p}_e + \mathbf{f}_e, \quad 0 \leq z \leq L \tag{3.2}$$

In Eq. (3.2), the operators $\mathbf{L}$ and $\mathbf{I}$ represent the stiffness and modified inertia matrices of the shell, respectively, based on the shell theory. The reader is referred to the work of Tsouvalas and Metrikine

[1]The ring frequency, often denoted as f_r, is the natural resonant frequency of the pile, associated with its radial modes of vibration.

[62] for a detailed description. The displacement vector $\mathbf{u}$ and its second time derivative $\ddot{\mathbf{u}}$ denote the mid-surface displacement and acceleration of the shell, respectively, varying with the axial coordinate z and time t. The boundary stress vector $\mathbf{t}_s$ accounts for the reaction of the surrounding soil on the shell within the range $z_1 \leq z \leq L$. The fluid pressure vector $\mathbf{p}_e$ corresponds to the pressure exerted on the outer surface of the shell in the region $z_0 \leq z \leq z_1$. The externally applied force vector $\mathbf{f}_e$ acts on the shell's surface. The Heaviside step functions $H\left(z - z_i\right)$ specify the segments where the fluid and soil interactions influence the shell. The abovementioned terms are further expanded as:

$$\mathbf{u} = \begin{bmatrix} u_z(z,t) & u_r(z,t) \end{bmatrix}^T$$

$$\ddot{\mathbf{u}} = \begin{bmatrix} \ddot{u}_z(z,t) & \ddot{u}_r(z,t) \end{bmatrix}^T$$

$$\mathbf{t}_s^j = \left[\lambda_j \nabla \cdot \mathbf{u}_s^j \mathbf{I} + \mu_j \left(\nabla \mathbf{u}_s^j + \left(\nabla \mathbf{u}_s^j \right)^T \right) \right] \cdot \hat{\mathbf{r}}$$

$$\mathbf{p}_e = \begin{bmatrix} 0 & p_r(z,t) \end{bmatrix}^T$$

$$\mathbf{f}_e = \begin{bmatrix} f_z(z,t) & f_r(z,t) \end{bmatrix}^T$$

Here, $\mathbf{t}_s^j$ represents the solid stress tensor of layer j, and $\hat{\mathbf{r}}$ is the unit normal vector to the shell's surface. By applying the Fourier transform, defined in Eq. (3.1), Eq. (3.2) is transformed into the frequency domain, denoted by the tilde symbol for complex amplitudes:

$$\mathbf{L}\tilde{\mathbf{u}} + \tilde{\mathbf{I}}\tilde{\ddot{\mathbf{u}}} = -\left(H\left(z - z_1\right) - H(z - L)\right) \tilde{\mathbf{t}}_s + \left(H\left(z - z_0\right) - H\left(z - z_1\right)\right) \tilde{\mathbf{p}}_e + \tilde{\mathbf{f}}_e \tag{3.3}$$

Fluid domain

The fluid domain is modelled as an inviscid compressible medium, fully characterised by the velocity potential $\phi_f(r,z,t)$. The equation of motion governing the fluid domain is given by:

$$\nabla^2 \phi_f(r,z,t) - \frac{1}{c_f^2} \frac{\partial^2 \phi_f(r,z,t)}{\partial t^2} = 0, \quad z_0 \leq z \leq z_1 \tag{3.4}$$

In Eq. (3.4), c_f represents the speed of sound in the fluid domain, and ∇^2 denotes the Laplace operator[2] defined in the cylindrical coordinate system. Similar to the shell equations, Eq. (3.4) can be transformed into the frequency domain using the Fourier transform pair:

$$\nabla^2 \tilde{\phi}_f(r,z,\omega) + \frac{\omega^2}{c_f^2} \tilde{\phi}_f(r,z,\omega) = 0 \tag{3.5}$$

Eq. (3.5) is known as the Helmholtz equation. Its solution, employing the separation of variables method, satisfies the radiation condition at infinity[3]:

$$\tilde{\phi}_f(r,z,\omega) = H_0^{(2)}\left(k_{\phi,f} r\right) \left(A_1 \mathrm{e}^{-\alpha_f z} + A_2 \mathrm{e}^{\alpha_f z} \right) \tag{3.6}$$

Here, $H_0^{(2)}\left(k_{\phi,f} r\right)$ denotes the Hankel function of the second kind of order zero, where $k_{\phi,f}$ is the separation constant in the radial r direction, describing the spatial distribution of the wave in the radial direction. The constants A_1 and A_2 are undetermined complex constants, where A_1 represents the amplitude of the downward-propagating wave, and A_2 represents the amplitude of the upward-propagating wave. The wavenumber in the fluid medium, α_f, is defined as:

$$\alpha_f = \sqrt{k_{\phi,f}^2 - \frac{\omega^2}{c_f^2}}$$

[2] $\nabla^2 = \nabla \cdot \nabla$. The Laplace operator is a second-order differential operator given by the divergence $(\nabla \cdot)$ of the gradient (∇f).

[3] If moving infinitely far away from the source, the amplitude of the waves tends towards zero.

The velocity and pressure fields are related to the velocity potential as follows, where $\hat{r}$ and $\hat{z}$ represent the unit vectors along the radial and vertical directions, respectively:

$$\tilde{\mathbf{v}}(r,z,\omega) = \nabla\tilde{\phi}_f(r,z,\omega) \quad \text{with: } \nabla = \frac{\partial}{\partial r}\hat{r} + \frac{\partial}{\partial z}\hat{z} \tag{3.7}$$

$$\tilde{p}_f(r,z,\omega) = -\mathrm{i}\omega\rho_f\tilde{\phi}_f(r,z,\omega) \tag{3.8}$$

Soil domain

The soil is modelled as a three-dimensional elastic continuum, and the wave propagation in this soil medium is described by the displacement potentials $\phi_s(r,z,t)$ and $\psi_s(r,z,t)$. Unlike water, which is modelled as a compressible fluid and supports only pressure waves, soil can sustain both compressional and shear waves due to its elastic properties. These potentials satisfy two uncoupled equations of motion:

$$\nabla^2\phi_s(r,z,t) - \frac{1}{c_L^2}\frac{\partial^2\phi_s(r,z,t)}{\partial t^2} = 0, \quad z \geq z_1 \tag{3.9}$$

$$\nabla^2\psi_s(r,z,t) - \frac{\psi_s(r,z,t)}{r^2} - \frac{1}{c_T^2}\frac{\partial^2\psi_s(r,z,t)}{\partial t^2} = 0, \quad z \geq z_1 \tag{3.10}$$

$$c_L^2 = \frac{\lambda_s + 2\mu_s}{\rho_s} \quad \text{and} \quad c_T^2 = \frac{\mu_s}{\rho_s}$$

Here, c_L and c_T are the speeds of compressional and shear waves in the medium, respectively. The constants λ_s and μ_s represent the Lamé coefficients, while ρ_s is the density of the soil. The calculation of these Lamé constants can be found in the work of Peng et al. [49]. Transforming the two equations above into the frequency domain using the Fourier transform pair from Eq. (3.1) yields:

$$\nabla^2\tilde{\phi}_s(r,z,\omega) + \frac{\omega^2}{c_I^2}\tilde{\phi}_s(r,z,\omega) = 0 \tag{3.11}$$

$$\nabla^2\tilde{\psi}_s(r,z,\omega) - \frac{\tilde{\psi}_s(r,z,\omega)}{r^2} + \frac{\omega^2}{c_T^2}\tilde{\psi}_s(r,z,\omega) = 0 \tag{3.12}$$

Solutions to Eq. (3.11) and Eq. (3.12) are obtained using the separation of variables method:

$$\tilde{\phi}_s(r,z,\omega) = H_0^{(2)}\left(k_{\phi,s}r\right)\left(A_3\mathrm{e}^{-\alpha_s z} + A_4\mathrm{e}^{\alpha_s z}\right) \tag{3.13}$$

$$\tilde{\psi}_s(r,z,\omega) = H_1^{(2)}\left(k_{\psi,s}r\right)\left(A_5\mathrm{e}^{-\beta_s z} + A_6\mathrm{e}^{\beta_s z}\right) \tag{3.14}$$

These solutions satisfy the radiation conditions at infinity, represented as $\lim_{r\to\infty}\tilde{\phi}_s(r,z,\omega) = 0$ and $\lim_{r\to\infty}\tilde{\psi}_s(r,z,\omega) = 0$. Here, $H_0^{(2)}\left(k_{\phi,s}r\right)$ and $H_1^{(2)}\left(k_{\psi,s}r\right)$ are the Hankel functions of the second kind of order zero and second kind of the first order, respectively. The constants $k_{\phi,s}$ and $k_{\psi,s}$ are separation constants in the radial r direction, while A_3, A_4, A_5, and A_6 are undetermined complex constants for the soil region. The wavenumbers along the vertical direction, α_s and β_s, are defined as:

$$\alpha_s = \sqrt{k_{\phi,s}^2 - \frac{\omega^2}{c_L^2}} \text{ and } \beta_s = \sqrt{k_{\psi,s}^2 - \frac{\omega^2}{c_T^2}}$$

The displacement fields and stress-displacement relations are given as [15]:

$$\tilde{u}_{s,r}(r,z,\omega) = \frac{\partial\tilde{\phi}_s(r,z,\omega)}{\partial r} - \frac{\partial\tilde{\psi}_s(r,z,\omega)}{\partial z} \tag{3.15}$$

$$\tilde{u}_{s,z}(r,z,\omega) = \frac{\partial\tilde{\phi}_s(r,z,\omega)}{\partial z} + \frac{1}{r}\frac{\partial\left(r\tilde{\psi}_s(r,z,\omega)\right)}{\partial r} \tag{3.16}$$

$$\tilde{\sigma}_{s,rr}(r,z,\omega) = \lambda_s \left(\frac{\partial \tilde{u}_{s,r}}{\partial r} + \frac{\tilde{u}_{s,r}}{r} + \frac{\partial \tilde{u}_{s,z}}{\partial z} \right) + 2\mu_s \frac{\partial \tilde{u}_{s,r}}{\partial r} \tag{3.17}$$

$$\tilde{\sigma}_{s,zz}(r,z,\omega) = \lambda_s \left(\frac{\partial \tilde{u}_{s,r}}{\partial r} + \frac{\tilde{u}_{s,r}}{r} + \frac{\partial \tilde{u}_{s,z}}{\partial z} \right) + 2\mu_s \frac{\partial \tilde{u}_{s,z}}{\partial z} \tag{3.18}$$

$$\tilde{\sigma}_{s,zr}(r,z,\omega) = \mu_s \left(\frac{\partial \tilde{u}_{s,r}}{\partial z} + \frac{\partial \tilde{u}_{s,z}}{\partial r} \right) \tag{3.19}$$

3.1.2. Boundary and interface conditions

In addition to the radiation conditions from Eq. (3.6) for the fluid and Eq. (3.13) and Eq. (3.14) for the soil, several boundary and interface conditions must be satisfied in the fluid and soil domains to solve for the undetermined complex constants $A_1 - A_6$.

At the sea surface ($z = z_0$), the pressure release boundary condition is imposed, indicating that the atmospheric pressure at the surface is zero, and the amplitude of the reflected waves equals that of the incident waves. While this assumes a simplified scenario compared to the reality of air bubbles on the sea surface due to waves and currents, it is expected to not significantly affect the accuracy of predictions [60]. Still, it might lead to a small overestimation of noise levels in the fluid near the surface.

$$\tilde{p}_f\left(r, z_0, \omega\right) = 0, \quad r \geq R \tag{3.20}$$

At the fluid-soil interface ($z = z_1$), the vertical stress equilibrium and the vertical displacement continuity are imposed, while the shear stress vanishes due to absence of tangential stresses in the fluid:

$$\tilde{\sigma}^1_{s,zz}\left(r, z_2, \omega\right) + \tilde{p}_f\left(r, z_2, \omega\right) = 0, \quad r \geq R \tag{3.21}$$

$$\tilde{u}^1_{s,z}\left(r, z_1, \omega\right) - \tilde{u}_{f,z}\left(r, z_1, \omega\right) = 0, \quad r \geq R \tag{3.22}$$

$$\tilde{\sigma}^1_{s,zr}\left(r, z_1, \omega\right) = 0, \quad r \geq R \tag{3.23}$$

At the soil-soil interface, stress equilibrium and displacement continuity are applied in both the z and r directions:

$$\tilde{\sigma}^j_{s,zz}(r, z_j, \omega) = \tilde{u}^{j-1}_{s,zz}(r, z_j, \omega), \quad 2 \leq j \leq N, \quad r \geq R \tag{3.24}$$

$$\tilde{\sigma}^j_{s,zr}(r, z_j, \omega) = \tilde{u}^{j-1}_{s,zr}(r, z_j, \omega), \quad 2 \leq j \leq N, \quad r \geq R \tag{3.25}$$

$$\tilde{u}^j_{s,z}(r, z_j, \omega) = \tilde{u}^{j-1}_{s,z}(r, z_j, \omega), \quad 2 \leq j \leq N, \quad r \geq R \tag{3.26}$$

$$\tilde{u}^j_{s,r}(r, z_j, \omega) = \tilde{u}^{j-1}_{s,r}(r, z_j, \omega), \quad 2 \leq j \leq N, \quad r \geq R \tag{3.27}$$

At the soil bottom ($z = H$), a rigid boundary is applied:

$$\tilde{u}^H_{s,z}(r, H, \omega) = 0, \quad r \geq R \tag{3.28}$$

$$\tilde{u}^H_{s,r}(r, H, \omega) = 0, \quad r \geq R \tag{3.29}$$

Furthermore, at the pile-water interface, pressure equilibrium and displacement continuity are imposed. A perfect contact condition is applied at the pile-soil interface, assuming no pile slip [62]. These kinematic conditions at the interface of the shell with its surroundings ($r = R$) are given as:

$$\tilde{u}_r(r, z, \omega) - \tilde{u}_f(r, z, t) = 0, \quad z_0 \leq z \leq z_1 \tag{3.30}$$

$$\tilde{u}_z(r, z, \omega) - \tilde{u}^j_{s,z}(r, z, \omega) = 0, \quad 1 \leq j \leq N \quad z_1 \leq z \leq L \tag{3.31}$$

$$\tilde{u}_r(r, z, \omega) - \tilde{u}^j_{s,r}(r, z, \omega) = 0, \quad 1 \leq j \leq N \quad z_1 \leq z \leq L \tag{3.32}$$

3.1.3. Solving the system of equations

The system of equations discussed in the preceding sections can be tackled by solving the forced response of the coupled system. However, this detailed process is left out here for brevity, and the reader is directed to the work of Tsouvalas and Metrikine [62]. In essence, a modal decomposition technique is employed for both the shell structure and the acousto-elastic waveguide. Utilising the mode-matching technique, the response of the coupled pile-water-soil system is obtained in the frequency domain. The wavenumber spectrum associated with the evanescent waves within the waveguide is of significant importance in the context of vibroacoustic interaction. The resulting set of response functions, including pressure, velocity, displacement, and stress tensors, serves as input for the sound propagation model.

3.2. Sound Propagation Module

As mentioned before, the input to the sound propagation module is provided by the sound generation module through a boundary integral formulation. This is done by deriving Green's tensor for a fluid overlaying a multilayered soil halfspace for sources both in the fluid and in the soil. These Green's tensors are obtained by placing a ring source in cylindrical coordinates at the boundary of the sound generation module, both in the fluid and in the soil, which generates pressure waves and produces a unit pressure amplitude at the location of the source. In the fluid a pressure-type ring source is placed at $[r_s, z_s]$ and in the soil a radial or vertical ring source is placed at $[r_s, z_s]$. Fig. 3.2 gives a schematic overview of the ring sources.

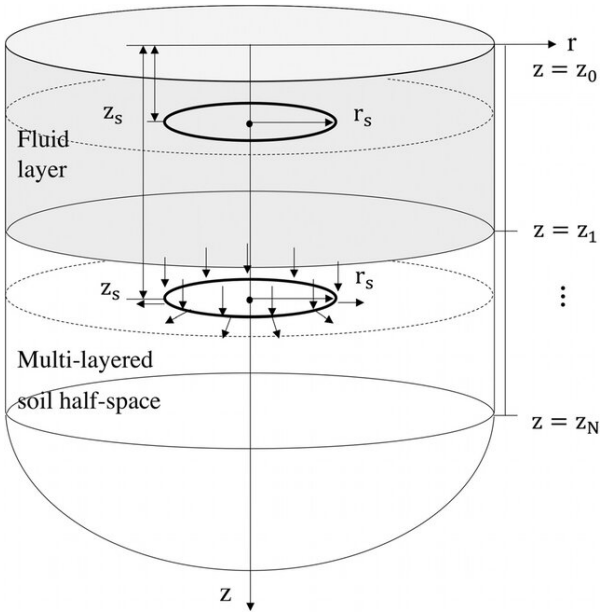

Figure 3.2: Schematic representation of the ring source at $r = r_s$, both in the fluid and in the soil [49].

3.2.1. Green's tensor for fluid source

To derive the Green's function for a fluid source, a pressure-type ring source is introduced located at (r_s, z_s) within the fluid layer. This ring source initiates pressure waves with a unit amplitude at its location. The equation of motion for the fluid displacement potential $\phi_{f,f}$ in the frequency domain is given by:

$$\left[\nabla^2 + k_f^2\right] \tilde{\phi}^g_{f,f}\left(r, z; r_s, z_s, \omega\right) = \frac{1}{-\rho\omega^2} \frac{\delta\left(r - r_s, z - z_s\right)}{2\pi r}, \quad r_s \geq R, \quad z_0 \leq z_s \leq z_1 \tag{3.33}$$

Additionally, the homogeneous equations of motion for the soil displacement potentials $\phi_{j,f}$ and $\psi_{j,f}$ are given as:

$$\left[\nabla^2 + k_{p_j}^2\right] \tilde{\phi}^g_{j,f}\left(r, z; r_s, z_s, \omega\right) = 0 \tag{3.34}$$

$$\left[\nabla^2 + k_{s_j}^2\right] \tilde{\psi}_{j,f}^g \left(r, z; r_s, z_s, \omega\right) = 0 \tag{3.35}$$

In these equations, each subscript has its significance: the first denotes the receiver location, and the second denotes the source location. f stands for the fluid domain, s stands for the soil domain, and j represents the jth soil layer. Next, the equations of motion are transformed to the wavenumber-frequency domain using the Hankel transform. The Hankel transform pair used in this work is given by:

$$\hat{f}\left(k_r\right) = \int_0^\infty f(r) J_0\left(k_r r\right) r dr \quad \text{and } f(r) = \int_0^\infty \hat{f}\left(k_r\right) J_0\left(k_r r\right) k_r dk_r \tag{3.36}$$

Transforming Eq. (3.33), Eq. (3.34) and Eq. (3.35) to the wavenumber-frequency domain gives the following expressions, which are wave equations reduced to depth-separated wave equations in the Hankel domain [3]:

$$\left[\frac{d^2}{dz^2} + k_{z,f}^2\right] \hat{\phi}_{f,f}^g \left(k_r, z; r_s, z_s, \omega\right) = \frac{1}{-\rho\omega^2} \delta\left(z - z_s\right) \frac{J_0\left(k_r r_s\right)}{2\pi} \tag{3.37}$$

$$\left[\frac{d^2}{dz^2} + k_{z,p_j}^2\right] \hat{\phi}_{j,f}^g \left(k_r, z; r_s, z_s, \omega\right) = 0 \tag{3.38}$$

$$\left[\frac{d^2}{dz^2} + k_{z,s_j}^2\right] \hat{\psi}_{j,f}^g \left(k_r, z; r_s, z_s, \omega\right) = 0 \tag{3.39}$$

the vertical wavenumber $k_{z,\xi} = \sqrt{k_\xi^2 - k_r^2}$ characterises the behaviour in the domain $\xi = f, p_j, s_j$. The solutions for the fluid displacement potential $\phi_{f,f}$ consist of a particular solution and a general solution, while the solutions for the soil displacement potentials $\phi_{s,f}$ and $\psi_{s,f}$ are purely a general solution:

$$\hat{\phi}_{f,f}^g \left(k_r, z; r_s, z_s, \omega\right) = \left(\frac{1}{-\rho\omega^2} \frac{e^{-ik_{z,f}|z-z_s|}}{4\pi i k_{z,f}} + A_1^g e^{ik_{z,f}z} + A_2^g e^{-ik_{z,f}z}\right) J_0\left(k_r r_s\right) \tag{3.40}$$

$$\hat{\phi}_{j,f}^g \left(k_r, z; r_s, z_s, \omega\right) = \left(A_{4j-1}^g e^{ik_{z,p_j}z} + A_{4j}^g e^{-ik_{z,p_j}z}\right) J_0\left(k_r r_s\right) \tag{3.41}$$

$$\hat{\psi}_{j,f}^g \left(k_r, z; r_s, z_s, \omega\right) = \left(A_{4j+1}^g e^{ik_{z,s_j}z} + A_{4j+2}^g e^{-ik_{z,s_j}z}\right) J_0\left(k_r r_s\right) \tag{3.42}$$

The same boundary and interface conditions, as described in Section 3.1.2, are applied to Eq. (3.40), Eq. (3.41), and Eq. (3.42). Here, the coefficients A_i^g with $i = 1, 2, ..., 4N + 2$ represent the undetermined complex amplitudes. Two unknown amplitude coefficients in the fluid displacement potential function $\phi_{f,f}$ indicate upward- and downward-propagating waves in the fluid, while four unknown amplitude coefficients in the soil displacement potential functions $\phi_{s,f}$ and $\psi_{s,f}$ indicate waves in each soil layer.

Applying the inverse Hankel transform to return to the frequency domain, the Green's tensor of the acousto-elastic medium in the frequency domain is given by:

$$\tilde{\Phi}_{\Xi,f}^g \left(r, z; r_s, z_s, \omega\right) = -\frac{1}{2} \int_{-\infty}^{+\infty} \left(\hat{\Phi}_{\Xi,f}^g \left(k_r, z; r_s, z_s, \omega\right)\right) H_0^{(2)}\left(k_r r\right) k_r dk_r \tag{3.43}$$

Here, $\hat{\Phi}_{\Xi,f}^g = \left[\hat{\phi} f, f^g, \hat{\phi} j, f^g, \hat{\psi} j, f^g\right]^{\mathrm{T}}$ represents the solutions of the displacement potential functions in the Hankel domain, and $\tilde{\Phi}_{\Xi,f}^g$ are the corresponding displacement potential functions in the frequency domain. The pressure, displacements, and stresses of the acousto-elastic medium are expressed by Green's functions of displacement potentials, which are omitted here for brevity [15].

By substituting the expressions into the boundary and interface conditions, detailed in Section 3.1.2, the final set of linear algebraic equations with unknowns A_i^g is obtained. This part, omitted for brevity, is discussed in the work by Peng et al. [49]. Once the amplitude coefficients are solved for every k_r, the Green's tensor for a pressure-type ring source in the fluid domain is obtained.

3.2.2. Green's tensor for soil source

In the context of sound propagation within the soil, a radial and vertical ring load is applied, as discussed in Section 3.2 and illustrated in Fig. 3.2. To derive Green's functions for the soil source, the layer of soil containing the source is divided into two sublayers, one above and one below the source level $z = z_s$, as depicted in Fig. 3.2. This division results in homogeneous equations of motion and includes the application of the jump condition at the source level, specifically concerning the stresses at $z = z_s$. This jump condition, referred to as the interface condition, is crucial for accurately modelling the soil source's impact on the surrounding medium. The homogeneous equation of motion for the fluid displacement potential $\phi_{f,s}$ in the frequency domain are:

$$\left[\nabla^2 + k_f^2\right] \tilde{\phi}^g_{f,s}\left(r, z; r_s, z_s, \omega\right) = 0 \tag{3.44}$$

For the soil displacement potentials $\phi_{j,s}$ and $\psi_{j,s}$, following equations of motion hold:

$$\left[\nabla^2 + k_{p_j}^2\right] \tilde{\phi}^g_{j,s^+}\left(r, z; r_s, z_s, \omega\right) = 0 \tag{3.45}$$

$$\left[\nabla^2 + k_{s_j}^2\right] \tilde{\psi}^g_{j,s^+}\left(r, z; r_s, z_s, \omega\right) = 0 \tag{3.46}$$

$$\left[\nabla^2 + k_{p_j}^2\right] \tilde{\phi}^g_{j,s^-}\left(r, z; r_s, z_s, \omega\right) = 0 \tag{3.47}$$

$$\left[\nabla^2 + k_{s_j}^2\right] \tilde{\psi}^g_{j,s^-}\left(r, z; r_s, z_s, \omega\right) = 0 \tag{3.48}$$

These equations are quite similar to the displacement potentials due to a fluid source, with the only difference being the subscript indicating the source's location. Additionally, a + or − is added to the source subscript to denote the layer above or below the source level, accounting for the jump condition.

Next, these equations are transformed to the wavenumber-frequency domain using the Hankel transform, similar to the procedure for a fluid source:

$$\left[\frac{d^2}{dz^2} + k_{z,f}^2\right] \hat{\phi}^g_{f,s}\left(k_r, z; r_s, z_s, \omega\right) = 0 \tag{3.49}$$

$$\left[\frac{d^2}{dz^2} + k_{z,p_j}^2\right] \hat{\phi}^g_{j,s^+}\left(k_r, z; r_s, z_s, \omega\right) = 0 \tag{3.50}$$

$$\left[\frac{d^2}{dz^2} + k_{z,s_j}^2\right] \hat{\psi}^g_{j,s^+}\left(k_r, z; r_s, z_s, \omega\right) = 0 \tag{3.51}$$

$$\left[\frac{d^2}{dz^2} + k_{z,p_j}^2\right] \hat{\phi}^g_{j,s^-}\left(k_r, z; r_s, z_s, \omega\right) = 0 \tag{3.52}$$

$$\left[\frac{d^2}{dz^2} + k_{z,s_j}^2\right] \hat{\psi}^g_{j,s^-}\left(k_r, z; r_s, z_s, \omega\right) = 0 \tag{3.53}$$

The homogeneous solutions for the displacement potential functions can be defined as:

$$\hat{\phi}^g_{f,s_n}\left(k_r, z; r_s, z_s, \omega\right) = \left(A_1^g e^{ik_{z,f}z} + A_2^g e^{-ik_{z,f}z}\right) J_0\left(k_r r_s\right) \tag{3.54}$$

$$\hat{\phi}^g_{j,s_n}\left(k_r, z; r_s, z_s, \omega\right) = \left(A_{4j-1}^g e^{ik_{z,p_j}z} + A_{4j}^g e^{-ik_{z,p_j}z}\right) J_0\left(k_r r_s\right) \tag{3.55}$$

$$\hat{\psi}^g_{j,s_n}\left(k_r, z; r_s, z_s, \omega\right) = \left(A_{4j+1}^g e^{ik_{z,s_j}z} + A_{4j+2}^g e^{-ik_{z,s_j}z}\right) J_0\left(k_r r_s\right) \tag{3.56}$$

In these equations, the coefficients A_i^g for $i = 1, 2, ..., 4N + 6$ represent the complex amplitudes, and the subscript n indicates the layer of the soil source. When $j = n$, the soil layer j is split into two sublayers at $z = z_s$, as depicted in Fig. 3.2, which are denoted as $\hat{\phi}s_n^+, s_n$, $\hat{\phi}s_n^-, s_n$, $\hat{\psi}s_n^+, s_n$, and $\hat{\psi}s_n^-, s_n$. The jump condition at the source level results in the following interface conditions at $z = z_s$ in the Hankel domain for the radial load case:

$$\hat{\sigma}^g_{zr_{s_n^+,s_n}}(k_r,z_s,\omega)-\hat{\sigma}^g_{zr_{s_n^-,s_n}}(k_r,z_s,\omega)=\frac{J_0(k_r r_s)}{2\pi} \tag{3.57}$$

$$\hat{\sigma}^g_{zz_{s_n^+,s_n}}(k_r,z_s,\omega)=\hat{\sigma}^g_{zz_{s_n^-,s_n}}(k_r,z_s,\omega) \tag{3.58}$$

$$\hat{u}^g_{\alpha_{s_n^+,s_n}}(k_r,z_s,\omega)=\hat{u}^g_{\alpha_{s_n^-,s_n}}(k_r,z_s,\omega), \quad \alpha=r,z \tag{3.59}$$

Similarly, the following set of interface conditions is found for the vertical load case:

$$\hat{\sigma}^g_{zz_{s_n^+,s_n}}(k_r,z_s,\omega)-\hat{\sigma}^g_{zz_{s_n^-,s_n}}(k_r,z_s,\omega)=\frac{J_0(k_r r_s)}{2\pi} \tag{3.60}$$

$$\hat{\sigma}^g_{zr_{s_n^+,s_n}}(k_r,z_s,\omega)=\hat{\sigma}^g_{zr_{s_n^-,s_n}}(k_r,z_s,\omega) \tag{3.61}$$

$$\hat{u}^g_{\alpha_{s_n^+,s_n}}(k_r,z_s,\omega)=\hat{u}^g_{\alpha_{s_n^-,s_n}}(k_r,z_s,\omega), \quad \alpha=r,z \tag{3.62}$$

By combining Eq. (3.57) through Eq. (3.62) with the boundary and interface conditions as outlined in Section 3.1.2, transformed into the Hankel domain, a linear algebraic system can be established with unknowns A_i^g for $i=1,2,...,4N+6$. Once the displacement potentials are solved in the Hankel domain, the expressions for Green's tensors of displacement and stress in the frequency domain can be derived.

3.3. Coupling of the modules

Evaluation of Green's tensors can be accomplished through two methods: (1) direct wavenumber integration along the real axis of k_r; and (2) employing the contour integration technique. A comprehensive explanation of these methods can be found in the study by Peng et al. [49]. Following this evaluation, the direct boundary element method is utilised to couple the modules responsible for sound generation and sound propagation. For an in-depth understanding of this coupling process, the reader is referred to the work of Peng et al. [49].

4

Modelling of noise mitigation measures

This chapter provides a more detailed exploration of the modelling aspects related to PULSE and air-bubble curtains. The modelling of PULSE can be conducted independently of the system modelling discussed in the preceding chapter. The system modelling computes the system's response to a unit load, allowing for the subsequent application of various PULSE settings. This process will be elaborated on in Section 4.1. As for the modelling of air-bubble curtains, SILENCE incorporates a dedicated module for calculating transmission losses attributed to different configurations of air-bubble curtains. This topic will be comprehensively discussed in Section 4.2.

4.1. Modelling of PULSE

Within the context of this study, modelling the impact of PULSE on the monopile and the surrounding media does not necessitate a complex model or algorithm. The fundamental principle of PULSE's effect on the system can be modelled relatively straightforwardly. While more complex models might yield more accurate predictions, they are unnecessary here. It is important to clarify that this research does not delve into the underlying mechanism of PULSE itself but focuses solely on the effects of different PULSE settings. Once the modelling principle is understood, the discussion will move on to the energy losses introduced by PULSE and the decision on an appropriate metric for normalising and comparing different settings. Using this metric, the input energy into the monopile from an impact hammer can be calculated, accounting for different PULSE settings.

As described in Section 2.3.1, elongating the contact time between the hammer and the monopile effectively spreads the force over a longer duration due to the liquid in PULSE. The frequency spectra, when the system is subjected to a unit amplitude hammer excitation, are computed first. This is the output of the SILENCE model. These frequency spectra are then multiplied by the actual time force, depending on the PULSE settings. In other words, this process involves calculating the system's response to a unit load and then multiplying this response by the elongated impulses provided by the various PULSE settings.

In this study, the effects of four distinct PULSE settings are investigated. The *no PULSE* setting represents a conventional impact hammer without the elongation effect of PULSE. The *minimum PULSE*, *medium PULSE*, and *maximum PULSE* settings represent different variations of impulse elongation, each with reduced amplitudes compared to the traditional impact hammer. Generally, greater elongation tends to yield more significant reductions in sound levels. The specific settings used in industry standards will be discussed in the next section.

4.1.1. Energy losses due to PULSE

Typically, the kinetic energy of the ram weight before striking the monopile is reported. However, the energy that reaches the monopile, known as ENTHRU, undergoes energy losses due to several factors.

Introducing PULSE between the hammer and the monopile results in additional losses, primarily due to heat dissipation from the liquid within the PULSE unit, as discussed in Section 2.3.1. As PULSE operates, the repeated compression and expansion of the liquid generate heat, leading to thermal energy losses. This phenomenon is particularly noticeable when the liquid undergoes rapid compression and expansion cycles, as in the case of PULSE activation during pile driving.

Different configurations of PULSE, characterised by variations in the amount of liquid used and the resulting elongation of the impulse, significantly influence the magnitude of energy losses. Considering that the top of the monopile remains above sea level during pile-driving operations, the hammer impact occurs in the air. The global efficiency, which encompasses all energy losses in the hammer, PULSE, and anvil, depends on the specific PULSE settings employed. This efficiency is defined as the ratio of the ENTHRU to the rated energy. The rated energy is the energy of the ram weight (calculated as stroke height $\times$ ram mass $\times$ gravity or $\frac{1}{2}mv^2$). The ENTHRU is computed by the prediction software GRLWEAP. According to a drivability assessment for a recent German project by Van Oord [9], the following approximate global efficiency values can be assumed for different PULSE settings:

- **No PULSE**: $\sim$86%
- **Zero PULSE**: $\sim$84%
- **Minimum PULSE**: $\sim$81%
- **Medium PULSE**: $\sim$74%
- **Maximum PULSE**: $\sim$66%

These settings can be defined as follows: *no PULSE* indicates that there is no PULSE between the hammer and the monopile. *Zero PULSE* implies PULSE installation between the hammer and the monopile but without any liquid. *Minimum PULSE*, *medium PULSE*, and *maximum PULSE* indicate the presence of 100 mm, 400 mm, and 800 mm of liquid in the PULSE system, respectively. In practice, the *zero PULSE* setting is not used as it can cause damage to PULSE. It is important to note that these values represent an approximation of the efficiencies for the different PULSE settings. They are calculated by summing all individual losses that occur and have not been validated with field data.

4.1.2. Normalisation metric for impulse elongation

As discussed in the preceding section, there exists a difference between the energy of the ram weight and the energy transmitted into the monopile, due to energy losses. To ensure a fair comparison among various PULSE settings, it is important to select the correct metric. Three potential options are being considered as metrics for normalising different PULSE settings:

- **Hammer energy:** This represents the energy directly transmitted by the impact hammer.
- **Monopile energy:** This denotes the energy entering the monopile, which is the energy in the hammer minus the energy losses.
- **Penetration depth:** This indicates the depth achieved as a result of a single blow with an impact hammer.

The hammer energy metric provides a straightforward measure of the energy directly applied by the impact hammer. However, it does not account for energy losses incurred during transmission to the monopile. While this metric offers simplicity and ease of measurement, it does not accurately reflect the effective energy transferred to the monopile. The penetration depth metric offers insight into the depth achieved by a single blow with the impact hammer. This metric directly correlates with the physical outcome of pile-driving operations and is often used as an indicator of performance. However, penetration depth alone does not fully capture the efficiency of energy transfer or the impact of energy losses.

The monopile energy metric takes into account the losses incurred during energy transmission and provides an accurate representation of the effective energy delivered to the monopile. Consequently, it serves as the basis for comparing various PULSE settings, ensuring that each impulse delivers an equivalent amount of energy to the monopile. To achieve this, amplification factors are employed to normalise the energy levels across different PULSE settings. By doing so, the monopile energy metric provides a scientifically accurate and fair comparison between different PULSE settings. This approach

ensures that variations in energy losses are properly accounted for, making it the most scientifically valid metric for comparison.

It is important to note that employing the monopile energy metric may lead to small overestimations of real-world outcomes. As advised by the noise specialist at Van Oord, utilising PULSE with equivalent input energy in the monopile is likely to result in a greater penetration depth compared to not using PULSE. Consequently, fewer blows could be required to achieve the final penetration depth of the monopile. As a result, the actual maximum sound levels are expected to be lower than the predicted values in this research. Since this study solely concentrates on noise mitigation, considerations related to drivability are beyond its scope.

In conclusion, while hammer energy and penetration depth metrics provide useful information, they do not fully account for the complexities of energy transfer and losses. The monopile energy metric stands out as the only comprehensive and scientifically valid option, ensuring an accurate comparison of different impulse elongations in terms of energy delivered to the monopile. The determination of this energy input will be elaborated upon in the following section.

4.1.3. Determining the energy input into the pile

Analysing the energy flux within the monopile allows for accurately determining the energy input into the pile. This energy flux through a cross-section at location z_0 of the monopile due to the compressional motion of the pile can be estimated by the product of the normal force in the shell and the vertical velocity of the mid-surface of the shell, multiplied by the area of the cross-section [60]:

$$E_{pile}\left(z_0, t\right) = 2\pi\, R\, N_{zz}\left(z_0, t\right) \frac{\partial u_z\left(z_0, t\right)}{\partial t} \tag{4.1}$$

Here, $2\pi R$ denotes the circumference of the monopile, $N_{zz}\left(z_0, t\right)$ signifies the normal force along the z-direction, and $\frac{\partial u_z(z_0,t)}{\partial t}$ represents the rate of change of displacement in the z-direction of the monopile, equivalent to the velocity of the monopile in the z-direction.

4.2. Modelling of air-bubble curtains

Implementing the modelling of air-bubble curtains into the semi-analytical SILENCE model described in Chapter 3 involves several steps. Yaxi et al. [46] developed a multi-physics model for simulating noise mitigation using air-bubble curtains, comprising four distinct modules, which will be detailed in the subsequent sections. Fig. 4.1 gives an overview of the complete coupled model, including the sound generation, sound reduction and sound propagation module. Initially, a compressible flow model is used to depict the transfer of compressed air from the air-injection vessel to the perforated hose on the seabed. The output generated by this model serves as input for the hydrodynamic model, which aims to capture the characteristics of bubble generation and their evolution with depth and range. Subsequently, an acoustic model is utilised to predict the sound transmission loss of the air-bubble curtain, with this transmission loss employed in the vibroacoustic model to predict underwater noise levels. Coupling between the acoustic model and the vibroacoustic model occurs through a boundary integral formulation, similar to the approach in Section 3.2.

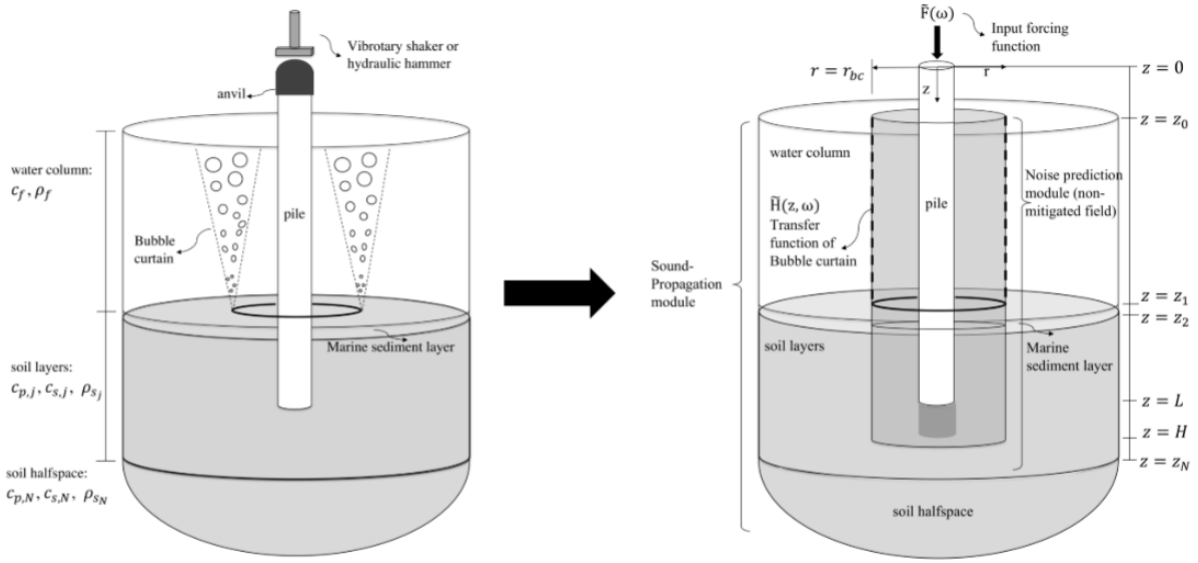

Figure 4.1: (left) Schematic representation of the complete system with an air-bubble curtain, and (right) the coupled model incorporating the transfer function for transmission losses caused by the air-bubble curtain [49].

4.2.1. Compressible flow model

This model describes the transport of compressed air in the hose, based on the compressible flow theory. The main input for this model is the total amount of air that is delivered by the compressors, which are usually located at the air-injection vessel. This is given as the volumetric flow rate at free air delivery conditions (FAD), meaning at standard atmosphere (atm) defined as 101325 Pa and at 293.15 K. Furthermore, the density of the seawater, the water depth, and the geometrical characteristics of the feeding and perforated hose configuration are required. The output of the model is the pressure distribution along the hose and the axial flow velocities and mass flow rates at each nozzle. The model considers a straight, horizontal hose with a constant diameter and uniform spacial of identical nozzles[1], and assumes symmetry. The air is injected from both sides of the hose, and due to symmetry only half of the total length is required to characterise the flow and pressure distribution. Fig. 4.2 shows the model, which is a discretised hose with a fixed number of segments, according to the length L and the nozzle spacing S of the hose. For each segment i, Shapiro [55] developed the following equation to obtain the mass flow rate $\dot{m}_{nz,i}$ at the nozzle:

$$\dot{m}_{nz,i} = C_d \frac{\pi d^2}{4} \left(\frac{2\gamma}{\gamma - 1} P_i \rho_i \left[1 - \left(\frac{P_{hst}}{P_i} \right)^{\frac{\gamma-1}{\gamma}} \right] \left(\frac{P_{hst}}{P_i} \right)^{\frac{2}{\gamma}} \right)^{0.5} \tag{4.2}$$

This equation is based on the isentropic compressible flow theory (Eq. (4.3)) and the state equation of the ideal gas law (Eq. (4.4)). Furthermore, in these equations, the discharge coefficient C_d is equal to 0.55 [43] and is used for each nozzle, d is the diameter of the nozzle, $\gamma = 1.402$ is the air adiabatic constant, P_i is the pressure inside the hose at each nozzle location, ρ_i is the density of the air inside the hose at each nozzle location, P_{hst} is the hydrostatic pressure outside the hose, M_i is the Mach number at each nozzle, U_i is the air velocity at each nozzle, $R = 287$ J/kg/K is the specific air gas constant, and $T = 291$ K is the assumed air temperature.

$$\frac{P_i}{P_{hst}} = \left(1 + \frac{\gamma - 1}{2} M_i^2 \right)^{\frac{\gamma}{\gamma-1}} \tag{4.3}$$

$$M_i = \frac{U_i}{\sqrt{\gamma R T}} \tag{4.4}$$

[1] In reality, the hole size increases due to the pressure in the hose. This means that the hole sizes are not constant.

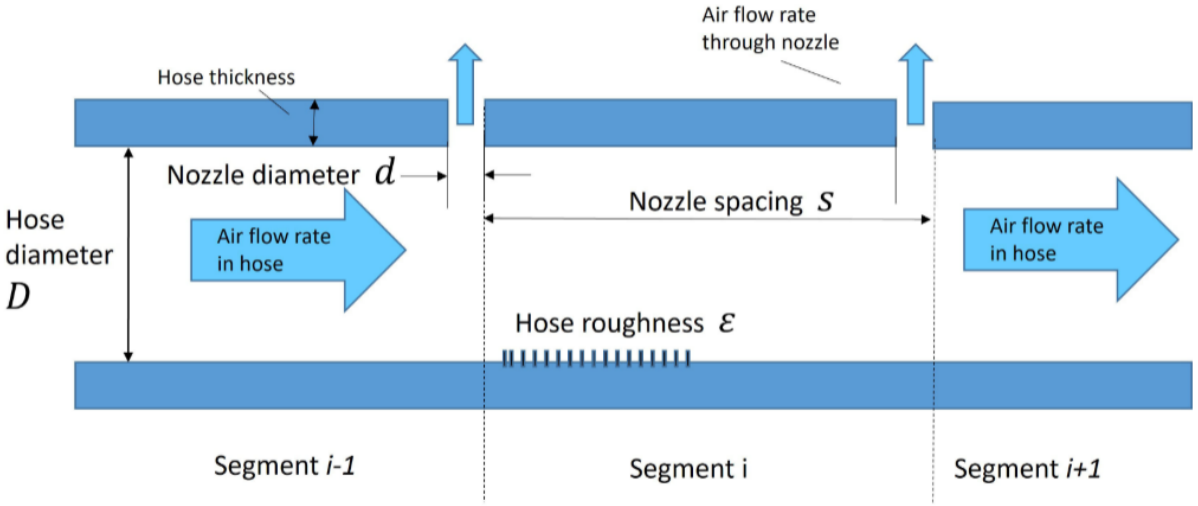

Figure 4.2: Schematic overview of the discretised compressible flow model [46].

4.2.2. Hydrodynamic and acoustic model

The hydrodynamic model, based on the airflow velocity through each nozzle derived in the compressible flow model, aims to capture the dynamics of bubble generation and development. This model characterises a turbulent two-phase bubble flow, tracing the evolution of the bubble plume from its nozzle origin to subsequent breakup and coalescence. Peng et al. [46, 49] described this hydrodynamic model, building upon the fluid dynamic model developed by Bohne et al. [6]. For a comprehensive understanding of the methodology and equations involved, readers are directed to the work of Bohne et al. [6], omitted here for brevity.

Once the hydrodynamic model has been utilised, the next step involves deploying the acoustic model. This model is based on a simplified one-dimensional acoustic wave propagation approach developed by Commander & Prosperetti [10]. Using the bubble characteristics obtained from the hydrodynamic model, this model determines the local effective wavenumber distribution across the water depth. With these local effective wavenumbers, a complex transfer function is established per z-coordinate, comprising complex transmission coefficients. This transfer function is coupled to the noise prediction module through a boundary integral formulation. For a detailed description of this process, readers are referred to the works of Peng et al. [49] and Bohne et al. [6].

5

Effect of PULSE on radiated underwater noise

In this chapter, the previously introduced modelling techniques are employed to simulate various scenarios. The objectives include assessing the effect of impulse elongations on pile vibrations and the surrounding environment, as well as evaluating the impact of combining impulse elongations with air-bubble curtains on radiated noise. To achieve this, different cases are elaborated on after comparing the model to field data. Section 5.1 provides an overview of the analysed cases, followed by the input parameters in Section 5.2. In Section 5.3, the model is compared to field data before discussing the effects of PULSE on the monopile in Section 5.4. The effects of PULSE, including its combination with air-bubble curtains, on the exterior domain are discussed in Section 5.5. The chapter concludes with the spectral insertion losses for all analysed cases in Section 5.6.

5.1. Overview of the different cases

This study analyses three distinct cases to address the research objectives:

1. PULSE without additional mitigation measures.
2. PULSE combined with a BBC.
3. PULSE combined with a DBBC.

The first case is designed to meet the first research objective, while the second and third cases aim to fulfil the second research objective. Before discussing these cases in Section 5.5, it is essential to compare both scenarios – one without an air-bubble curtain (case 1) and one with an air-bubble curtain (case 3) – against field data. Therefore, the parameters of cases 1 and 3 are provided in the next section, as only these are used for comparison against field data. The comparison for the case without air-bubble curtains is detailed in Section 5.3.1, while the comparison for the case with an air-bubble curtain is presented in Section 5.3.2. This step ensures that the modelling of PULSE and air-bubble curtains is correctly integrated into the semi-analytical model.

5.2. Input parameters

This section presents the input parameters used to model the different cases. This includes numerical parameters for the frequency and time analyses, which are consistent across all cases, as well as location-specific parameters. Assumptions are made for the location-specific parameters to approach reality as closely as possible when simulating the model. These assumptions concern the input force, pile geometry, and the stratification of water and soil layers, all of which will be described in detail in this section.

5.2.1. Frequency and time analyses

To perform frequency and time analyses in SILENCE, two parameters are essential as input: the number of frequency steps N_f and the time step size Δt.

The number of frequency steps N_f is calculated as half the number of time steps N_t:

$$N_f = \frac{N_t}{2} \tag{5.1}$$

To determine N_t, the total duration of the analysis t is divided by the time step size Δt. The duration must be sufficient to allow the sound wave to travel from the source to the hydrophone location. In this study, the hydrophones are situated 750 meters from the monopile, requiring a total duration of at least 0.5 seconds for sound waves travelling at the speed of sound in water. To capture the complete signal, a duration of 1 second is chosen:

$$N_t = \frac{t}{\Delta t} \tag{5.2}$$

The time step size Δt is determined by the reciprocal of twice the maximum frequency f_{max}:

$$\Delta t = \frac{1}{2 f_{max}} \tag{5.3}$$

For this analysis, f_{max} is set at 1000 Hz, as higher frequencies are unlikely to significantly contribute to the noise generated for the pile configurations considered in this study and would excessively increase computational demands. Finally, the frequency step size Δf is calculated as follows:

$$\Delta f = \frac{f_{max}}{N_f} \tag{5.4}$$

The parameters used for the frequency and time analyses are summarised in Table 5.1.

Table 5.1: Relevant parameters for the frequency and time analyses.

Description	Parameter	Value	Unit
Number of frequency steps	N_f	1000	-
Time step size	Δt	0.0005	s
Number of time steps	N_t	2000	-
Total time duration	t	1	s
Maximum frequency	f_{max}	1000	Hz
Frequency step size	Δf	1	Hz

5.2.2. Force input

The hammer force is modelled as a vertical force applied at the top of the monopile. As the impulse varies over time, it is depicted in a force-time diagram. The force-time diagrams for the different PULSE settings, as modelled by IQIP in FEM software for a recent German project, are depicted in Fig. 5.1.

For a recent German project, the IHC S-4000 hydraulic hammer with PULSE is utilised. This hydraulic hammer has a rated energy of 4000 kJ. Different PULSE settings include *no PULSE*, *minimum PULSE*, *medium PULSE*, and *maximum PULSE*, which are specifically modelled by IQIP for a recent German project. The *no PULSE* setting signifies the absence of PULSE, thus representing the force-time diagram of the IHC S-4000 hydraulic hammer alone.

To analyse how the applied force's energy is distributed across different frequencies, the input force is converted into the frequency domain, as shown in Fig. 5.2. This transformation is accomplished using the discrete Fourier transform pair defined in Eq. (3.1). Minor pressure fluctuations at higher frequencies likely result from small ripples in the input forces in the time domain. These ripples cause high-frequency components because rapid changes or discontinuities in the force signal translate into

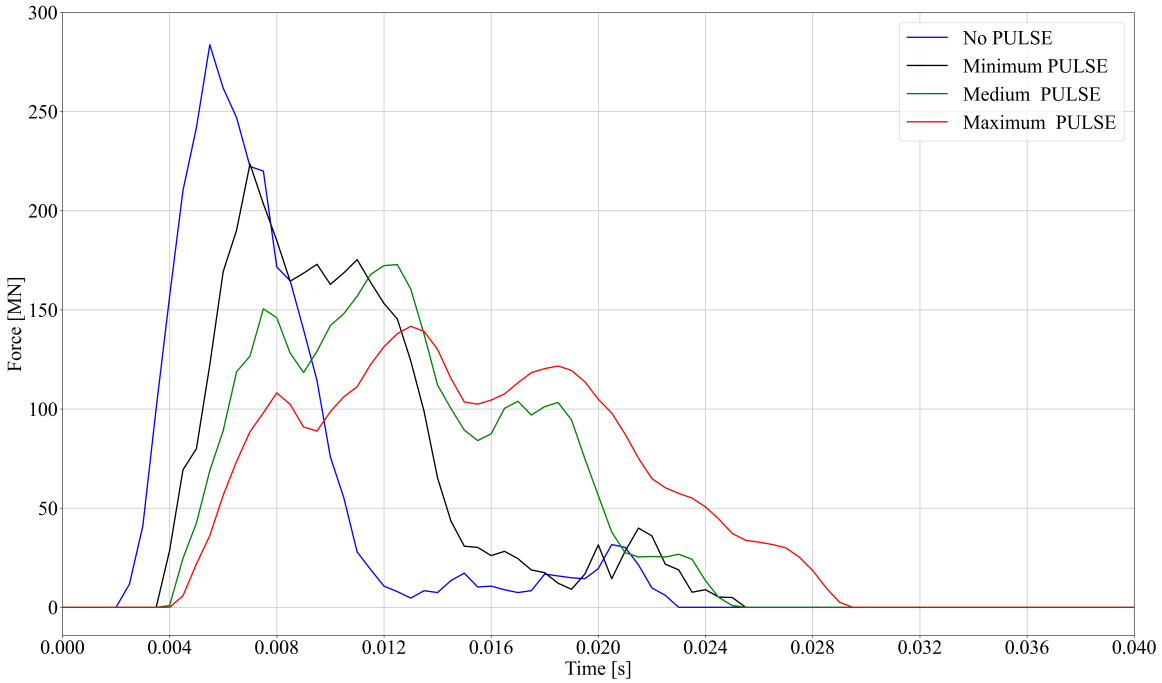

Figure 5.1: Force-time diagrams, employed in a recent German project, illustrate various configurations of PULSE settings. It is important to highlight that although the analysed impulse duration spans 1 second, the figure is zoomed to focus specifically on the active force duration.

a broad range of frequencies when analysed using the Fourier transform. Thus, these high-frequency components appear in the frequency domain, explaining the minor fluctuations at higher frequencies.

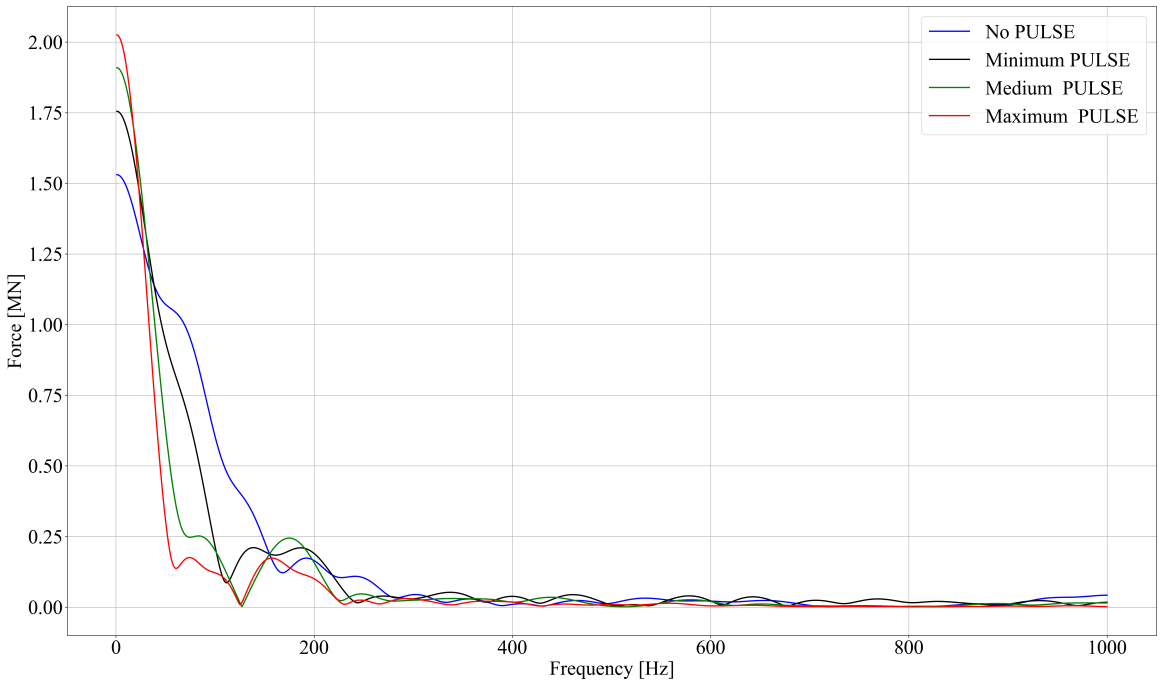

Figure 5.2: Different settings of PULSE in the frequency domain, obtained by applying the discrete Fourier transform pair on the force-time diagrams.

5.2.3. Monopile geometry

Monopile designs vary based on their intended installation location. These structures are constructed from multiple welded sections, each with a specific diameter and thickness. Typically, some sections have a tapered shape, while others are straight, featuring larger diameters at the base and smaller diameters at the top. In a recent German project, monopiles feature a top diameter of **** mm and variable diameters ranging from 8750 to 9000 mm at the base, depending on the location. Additionally, monopile thickness varies along their length, ranging from ** to ** mm, depending on location. Average values for each monopile are computed as the model requires a constant diameter and thickness:

$$D = \frac{1}{N} \sum_{n=1}^{N} D_n \tag{5.5}$$

$$d = \frac{1}{N} \sum_{n=1}^{N} t_n \tag{5.6}$$

Furthermore, the model requires the density, Young's modulus, and Poisson's ratio of the monopiles. While the monopiles are constructed using three types of steel (****, ****, and ****), the predominant material is **** steel. Therefore, for modelling purposes, the monopiles are assumed to comprise **** steel, with corresponding density values, Young's modulus, and Poisson's ratio, consistent across all cases. Table 5.2 provides an overview of the utilised values for each modelled monopile.

Table 5.2: Relevant parameters for the material properties and geometry of the monopiles.

Description	**Parameter**	**Unit**	**Case 1 Value**	**Case 3 Value**
Young's modulus	E	N/m^2	210×10^9	210×10^9
Poisson's ratio	ν	-	0.30	0.30
Density	ρ	kg/m^3	7850	7850
Thickness	d	m	<0.010	<0.010
Diameter	D	m	****	****
Length	L	m	81.42	78.99
Penetration depth	L_p	m	35.60	33.50

5.2.4. Water and soil stratification

The water and soil characteristics are crucial in acoustic wave propagation and must be accurately represented in the model. Given the proximity of the monopile locations for the analysed site, the water parameters are assumed to remain consistent across all locations. The site is assumed to show generally well-mixed saltwater conditions. For a frequency range up to 1000 Hz, as is analysed in this research, dominant sound channels are not to be expected, so layering within the water column has not to be considered, and seawater is represented as a homogeneous fluid with uniform temperature and salinity throughout the water depth [36]. Given the relatively shallow water depth, the impact of increasing hydrostatic pressure on the speed of sound propagation in acoustic waves is minimal. As a result, the speed of sound is considered constant throughout the water column. The water column parameters are as follows:

- Seawater density ρ_w: 1027 kg/m^3
- Speed of sound in seawater c_w: 1507 m/s

Each location shares a similar water and soil stratification setup, featuring a water column overlaying distinct soil layers. The soil is divided into two layers with comparable characteristics to accommodate the maximum allowable soil layers in SILENCE. The upper layer (L1) comprises marine mud and Holocene clay, while the lower soil layer (L2) represents deeper substrates, with its characteristics approximated by averaging those of the underlying layers. Fig. 5.3 illustrates this stratification pattern applicable to all scenarios.

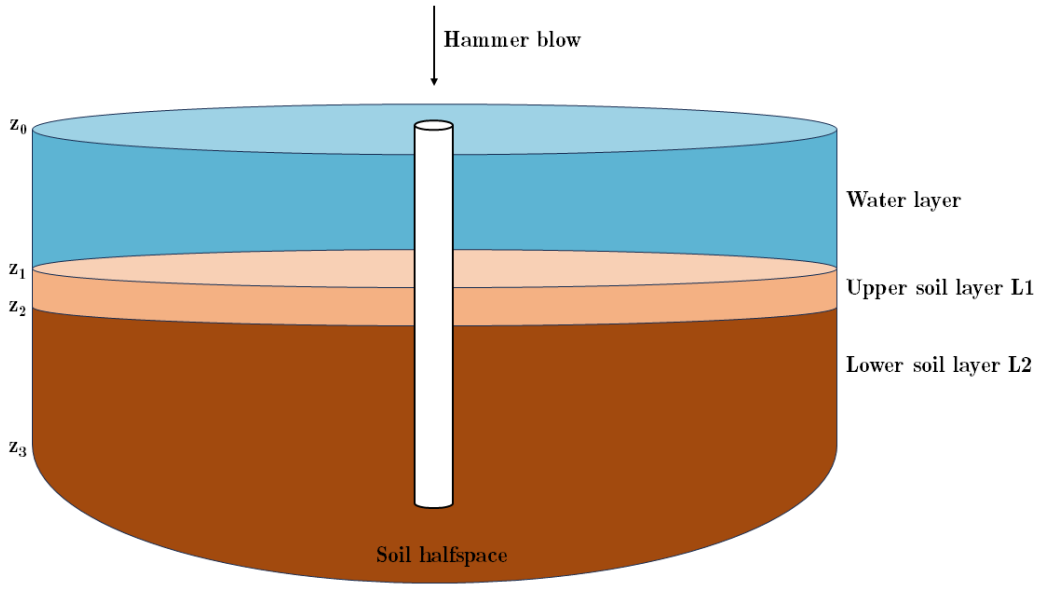

Figure 5.3: Basic setup of water and soil stratification used in the model, showing the water layer, upper soil layer (L1), and lower soil layer (L2).

Geotechnical reports made available by Van Oord [32, 36] provide the necessary parameters for soil characterisation. Young's modulus, Poisson's ratio, and density are derived from these reports, with compressional wave speed (v_p) and shear wave speed (v_s) subsequently calculated as follows:

$$v_p = \sqrt{\frac{E(1-\nu)}{\rho(1+\nu)(1-2\nu)}} \tag{5.7}$$

$$v_s = \sqrt{\frac{E}{2\rho(1+\nu)}} \tag{5.8}$$

The water depth, depth of the soil layers, and soil-related parameters are outlined in Table 5.3. The obtained soil parameters fall within a reasonable range based on research by Aziman et al. [2]. Additionally, soil-damping properties must be accounted for. Based on research by Hamilton [20], approximations of the damping parameters for the soil are obtained as follows:

- Damping ratio of compressional waves: 0.02 (= 2%)
- Damping ratio of shear waves: 0.05 (= 5%)

These damping coefficients are incorporated into the model as complex Lamé constants (λ^* and μ^*), where the imaginary part represents a percentage of the real part. For instance, a damping coefficient of 0.02 corresponds to 2% damping. By introducing these complex Lamé constants, the damping of the entire soil region is covered.

Table 5.3: Relevant parameters for water and soil stratification.

Description	Parameter	Unit	Case 1 Value	Case 3 Value
Sea surface from top pile	z_0	m	3	3
Water depth from top pile	z_1	m	45.82	45.49
Depth L1 from top pile	z_2	m	57.52	54.49
Depth L2 from top pile	z_3	m	96.32	93.49
Young's modulus L1	E_{s1}	N/m^2	8.0×10^7	6.9×10^7
Poisson's ratio L1	ν_{s1}	-	0.4967	0.4971
Density L1	ρ_{s1}	kg/m^3	1702	1683
Compressional wave speed L1	$v_{p,s1}$	m/s	1555	1538
Shear wave speed L1	$v_{s,s1}$	m/s	125	116
Young's modulus L2	E_{s2}	N/m^2	1.7×10^9	1.9×10^9
Poisson's ratio L2	ν_{s2}	-	0.4416	0.4415
Density L2	ρ_{s2}	kg/m^3	2060	2055
Compressional wave speed L2	$v_{p,s2}$	m/s	1666	1751
Shear wave speed L2	$v_{s,s2}$	m/s	538	566

The complex Lamé constants, λ^* and μ^*, are fundamental parameters in describing the elastic properties of materials. When considering damping, these constants are expressed as complex numbers:

$$\lambda^* = \lambda\,(1 + i\alpha_p) \tag{5.9}$$

$$\mu^* = \mu\,(1 + i\alpha_s) \tag{5.10}$$

Here, λ and μ are the real parts of the Lamé constants, representing the elastic properties of the material. i is the imaginary unit, and α_p and α_s are the damping coefficients for compressional and shear waves, respectively. The imaginary components of these constants introduce energy dissipation into the model [48].

5.2.5. Air-bubble curtain characteristics

To analyse the cases where PULSE is combined with air-bubble curtains, it is necessary to specify the characteristics of these air-bubble curtains. Case 3 (PULSE combined with a DBBC) is used to compare with field data. As previously mentioned, once this comparison is complete, all three cases will be analysed. Consequently, the characteristics of the air-bubble curtain for case 2 (PULSE combined with a BBC) are also provided here, even though this case is not compared to field data.

For the application of air-bubble curtains in a recent German project, two key reports are referenced: the underwater technical report [18] and the *Abschlussbericht* [8], both from itap (Institute of Technical and Applied Physics, Germany). These documents provide the parameters for the air-bubble curtains. Specifically, the underwater technical report details the nozzle diameter and nozzle spacing, while the *Abschlussbericht* includes information on the hose diameter, the amount of injected air (i.e., airflow), and the radius of the air-bubble curtain. From the amount of injected air, the gas velocity at the nozzle can be calculated as discussed in Section 4.2. This calculated gas velocity is also an essential input for the SILENCE model.

The key parameters for the air-bubble curtains, as required for the model, are summarised in Table 5.4. These parameters include:

- **Nozzle diameter:** The diameter of the individual nozzles on the hose; affecting the size and distribution of bubbles.
- **Nozzle spacing:** The distance between adjacent nozzles; influencing the density and coverage of the bubbles.

- **Hose diameter:** The overall diameter of the hose used to deploy the air-bubble curtain; impacting the structural integrity and airflow capacity.
- **Injected airflow:** The volume of air injected into the hose; determining the effectiveness and efficiency of the bubble generation.
- **Air-bubble curtain radius:** The radius of the air-bubble curtain; defining the spatial extent of its protective acoustic barrier.
- **Gas velocity at the nozzle:** The speed at which air exits the nozzle; crucial for the formation of the bubbles.

Table 5.4: Relevant parameters for the air-bubble curtains.

Description	Unit	Case 2 (BBC) Value	Case 3 (DBBC) Value
Nozzle diameter	m	0.002	0.002
Nozzle spacing	m	0.25	0.25
Hose diameter	mm	152	102
Injected airflow	m^3/min/m	0.97	0.59
Radius BBC1	m	75	75
Radius BBC2	m	-	150
Gas velocity at nozzle BBC1	m/s	168	104
Gas velocity at nozzle BBC2	m/s	-	99

5.3. Comparison to field data

This section compares the model to field data for two cases: (i) PULSE without additional mitigation measures, involving a monopile installed with the *maximum PULSE* setting, and (ii) PULSE combined with a DBBC, involving a monopile installed with the *maximum PULSE* setting and a DBBC. Data from a recent German project is used for these comparisons. Since during this project only three monopiles were installed without an HSD-system – which is not included in this study – the selection of monopiles for comparison is straightforward. The following monopiles are used:

- PULSE without additional mitigation measures: D26
- PULSE combined with air-bubble curtains (DBBC): D16

For these so-called test piles, there were no noise limits in place; otherwise, conducting the tests would be nearly impossible. To ensure an accurate comparison between the model and the field data, the input energy in the monopile must be consistent in both cases. This can be achieved as follows:

1. Determining the number of blows for final penetration depth
Since the model considers sound levels at the final penetration depth, it is important to consider this depth in the measurements. Clear criteria are needed to decide how many blows from the measurements to consider. The following criteria are used to determine the appropriate number of blows representing the final penetration depth:

1. **Penetration depth:** Determine the number of blows required to achieve the last 25 cm penetration depth, as this study focuses on the final penetration depth.
2. **Variability of sound levels:** Examine the variability of the SEL and L_{peak} measurements over time. Reliable comparison with the model requires that the SEL and L_{peak} values do not exhibit significant fluctuations during the period (i.e., the number of blows) being considered.

Using these criteria, the number of blows to consider for the final penetration depth is determined.

2. Determining the average blow energy
Next, the average blow energy for these blows is calculated by averaging the individual blow energies, which are measured on a linear scale in kJ. The blow energy refers to the kinetic energy delivered by the hydraulic hammer to drive the monopile into the ground.

3. Determining the energy input into the pile
As explained in Section 4.1.2, the energy input into the pile, rather than the blow energy, is considered for a fair comparison. The average blow energy is therefore adjusted by multiplying it by the efficiency of the *maximum PULSE* setting, which was used in a recent German project. This gives the actual energy input into the monopile, which is used for the model input.

Once the energy input into the pile is determined, the model's sound levels are compared with the field data. Sound levels are collected at 750 meters from the monopile, 2 meters above the seabed, using hydrophones. Multiple hydrophones are placed around each monopile location at this distance to comply with regulations. Specifically, four hydrophones are placed at 750 meters from the monopile. To average the sound levels measured by the four hydrophones, the SEL and L_{peak} values captured by each hydrophone are converted to pressure values using the following equation for sound intensity X:

$$X = X_{\text{ref}} \cdot 10^{\frac{\text{Decibel Level}}{10}} \tag{5.11}$$

Here, X_{ref} is the reference pressure underwater, which is 10^{-6} Pa. After converting the decibel levels to pressure values, these pressure values are averaged across the four hydrophones and then converted back to the decibel scale using Eq. (2.6).

With the procedure described above, the model can be compared with the measurements. First, the location of the monopile is discussed. Then, the blow energy used in the field data is determined, following the outlined procedure, to set the input energy for the model. Next, the evolution of the impulse in the time domain is analysed to check if the arrival time matches the expected arrival time. Finally, the sound levels predicted by the model are quantitatively compared to the field data by analysing the SEL and L_{peak} values over time, and a qualitative comparison is made through the examination of the 1/3 octave band spectrum.

5.3.1. PULSE without additional mitigation measures

Specifications of the monopile location

Fig. 5.4 illustrates the position of the monopile within the OWF. Multiple hydrophones are positioned around the monopile to monitor and measure sound levels at various locations. Relevant hydrophones are labelled *D26_B750_1* through *D26_B750_4*, and are strategically placed around the monopile based on the expected current and wind conditions, which determine the heading of the installation vessel and the anchor lines, thus influencing the possible locations for the hydrophones.

Figure 5.4: Location of monopile D26 and the associated measurement positions. Relevant hydrophones are labelled *D26_B750_1* through *D26_B750_4* [28].

Determination of the blow energy

By applying the previously mentioned criteria, the number of blows needed for comparison with the model can be determined. According to the piling data for monopile D26 [24], 34 blows were required to drive the monopile the final 25 cm into the ground, reaching the final penetration depth. Additionally, Fig. 5.5 presents the SEL measurements over time, while Fig. 5.6 shows the L_{peak} measurements over time. Both sets of measurements are averaged across the four hydrophones. These figures indicate that the measured sound levels remain relatively stable during the last 34 blows, thus validating the selection of 34 blows for the comparison.

Furthermore, Appendix A provides the individual recordings from the four hydrophones for both SEL and L_{peak} values. These recordings are useful for examining the azimuthal direction spread. Differences of up to 2-3 dB can be observed in some directions. These directional differences in sound measurements arise due to several factors. Changes in water conditions, such as temperature, salinity, current direction, and pressure, influence the travel of sound waves. The shape and composition of the seabed cause sound waves to reflect and scatter differently. Additionally, the precise positioning of the hydrophones relative to the monopile results in varying sound levels due to sound wave interactions and interference patterns. Background noise from other vessels, marine life, and weather conditions also contribute to differences in recorded sound levels.

The recordings in the azimuthal direction highlight directional differences but are not individually analysed in this study. They are provided solely to illustrate these differences. Instead, the average of these four directions is used for comparison with the model.

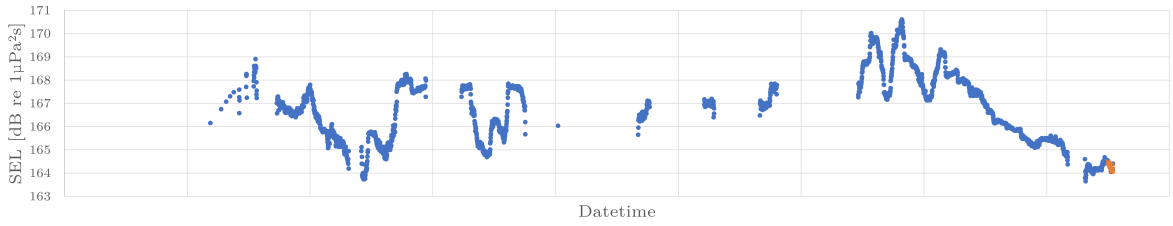

Figure 5.5: SEL measurements for monopile D26 monitored over time, depicting the average from the four hydrophones. The orange part highlights the blows necessary for the final 25 cm penetration.

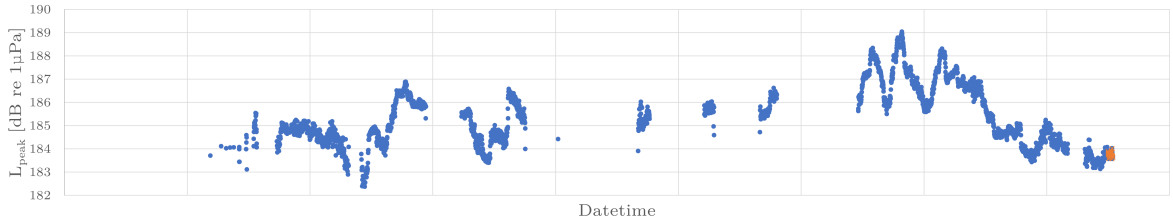

Figure 5.6: L_{peak} measurements for monopile D26 monitored over time, depicting the average from the four hydrophones. The orange part highlights the blows necessary for the final 25 cm penetration.

With the number of blows known, the minimum, mean and maximum blow energies for the final 25 cm penetration for monopile D26 are as follows:

- Minimum blow energy: 629 kJ
- Mean blow energy: 651 kJ
- Maximum blow energy: 664 kJ

Energy input into the pile

To begin the comparison, the energy input into the monopile must be equal for both the model and the measurements. For the model, the energy along the pile after a single hammer blow can be determined by integrating Eq. (4.1) over time. For the field data, the input energy, denoted as ENTHRU, is calculated by multiplying the mean blow energy of the last 34 blows by the 66% efficiency of the maximum PULSE setting used for monopile D26.

$$\text{ENTHRU} = \text{Mean blow energy} \cdot \text{efficiency} = 651\,\text{kJ} \cdot 0.66 = 430\,\text{kJ}$$

Fig. 5.7 illustrates the modelled energy distribution along the pile length. Key interfaces are marked with dotted lines: the blue line for the air-water interface, the first brown line for the water-soil interface, and the second brown line for the soil-soil interface. The red dotted line represents the derived ENTHRU.

The derived ENTHRU must correspond to the energy distributed along the pile within the initial few meters above sea level and the first few meters underwater. This is because, in the deeper parts of the pile, more energy has already been radiated into the surrounding water and soil, reducing the amount of energy available within the pile itself. The derived ENTHRU of 430 kJ, introduced by the hammer, aligns with the energy observed along the pile in these initial segments.

It is important to note that the actual dynamic response of the pile is not influenced by the modal summation[1] as long as a sufficiently large number of modes is considered. The stress wave propagating down the pile is accurately described, except for the first few centimeters from the pile top. Consequently, the acoustic pressure in the surrounding seawater and the wave field in the seabed are accurately captured. However, small jumps are caused by numerical artefacts.

[1] Theoretically, the solution includes an infinite number of modes, which represent different types of vibration patterns propagating through the structure. Each mode corresponds to a specific way the pile can vibrate, and the total response of the pile is the sum of all these modes.

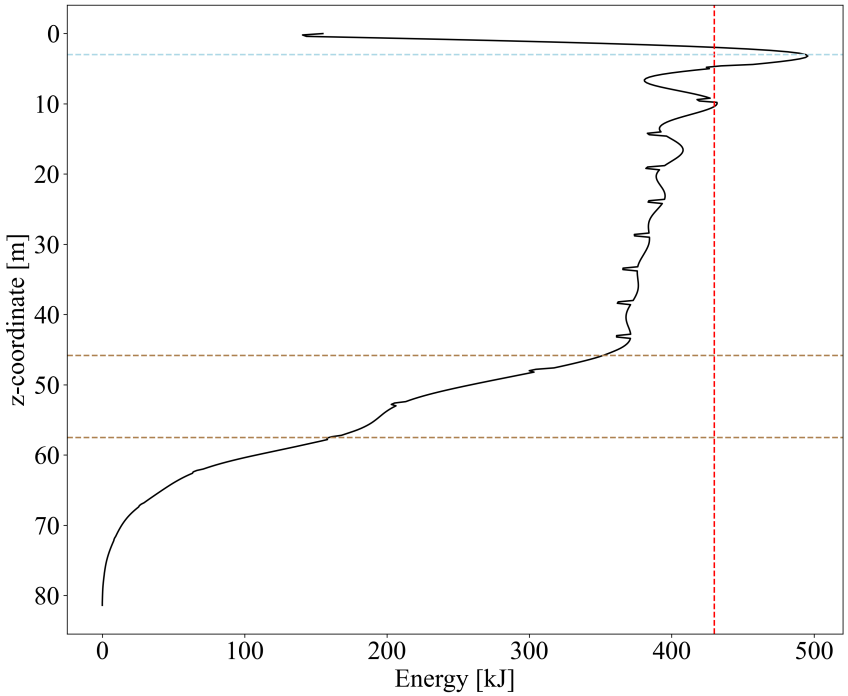

Figure 5.7: Total energy distribution along the pile length after a single hammer blow at the final penetration depth for PULSE without additional mitigation measures. The red dotted line represents the measured ENTHRU.

Arrival time of the impulse

The arrival time of the impulse indicates the successful transformation of frequency domain results, provided by the model, into the time domain. Given that sound levels are predicted at a distance of 750 meters from the monopile, the main impulse should arrive after approximately 0.5 seconds:

$$\text{Arrival time} = \frac{\text{Distance}}{\text{Speed of sound}} = \frac{750\,\text{m}}{1507\,\text{m/s}} = 0.498\,\text{s} \approx 0.5\,\text{s}$$

Fig. 5.8 shows that the modelled impulse arrives at approximately 0.5 seconds, aligning with the expected arrival time. It is important to note that the high-frequency oscillation observed at the start and end of the signal is due to the high-frequency truncation limit. In theory, this should appear as a flat line.

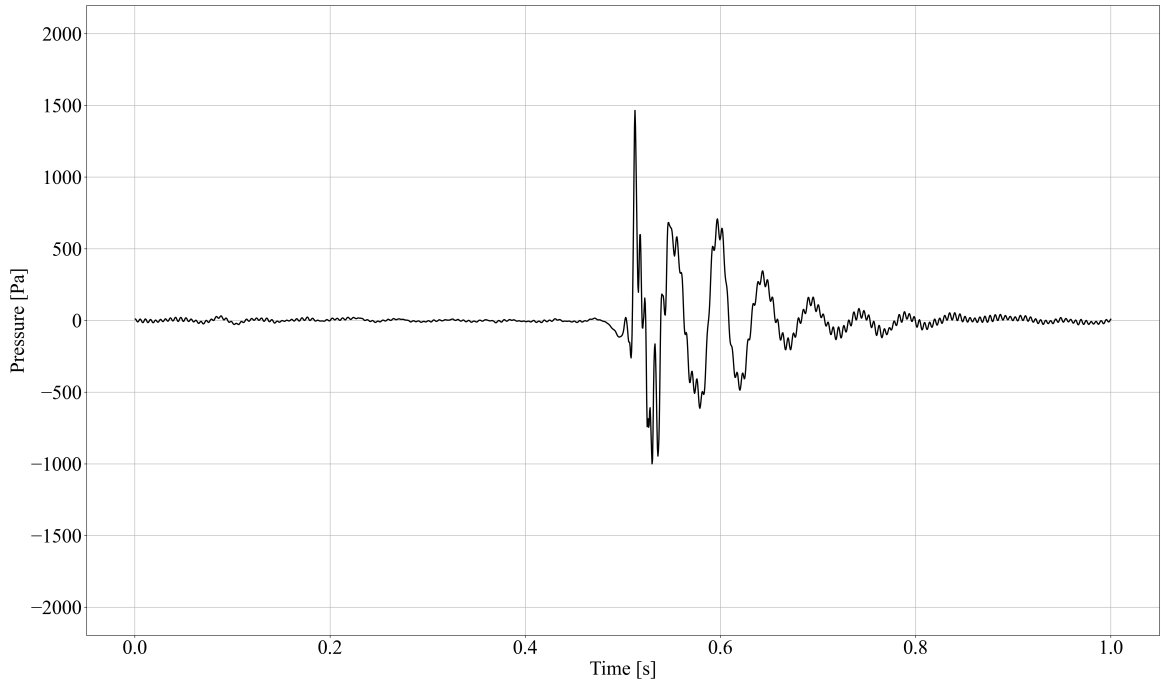

Figure 5.8: Pressure evolution of the modelled impulse in time for PULSE without additional mitigation measures. The impulse should arrive at 750 meters at 2 meters above the seabed after approximately 0.5 seconds.

Sound Exposure Level and Sound Peak Level

The predicted SEL and L_{peak} values from the model are compared to field measurements, using the average readings from four hydrophones. This average is visualised with a boxplot, which includes the minimum and maximum values of the last 34 blows indicated by its whiskers. Fig. 5.9 shows the modelled SEL and L_{peak} values over varying horizontal distances from the monopile. The SEL, represented by the solid black line, exhibits a clear decreasing trend as the distance from the source increases. Similarly, the L_{peak} values, depicted by the dashed blue line, also show a decreasing trend with increasing distance, with a noticeable increase after approximately 350 meters before decreasing again. The cause of this increase will be discussed in Section 5.5. The model demonstrates excellent consistency with field data at 750 meters from the monopile. Specifically, the model overestimates the average measurement by 0.6 dB for SEL, while for L_{peak}, the model underestimates the average measurement by 0.5 dB. These deviations indicate the model's strong accuracy in predicting both SEL and L_{peak}, falling within the uncertainty range of the results, which stems from inherent uncertainties in the parameter values, primarily soil parameters, and measurements [49].

To verify the soil model's accuracy, simulations were conducted for SEL and L_{peak} values up to 1500 meters, where corresponding measurements are available. The results indicate that the model aligns well with the observed data, with an underestimation of 2.7 dB for both SEL and L_{peak}. The primary factor behind the SEL and L_{peak} discrepancies is the selection of damping parameters. Despite the challenges and uncertainties in accurately modelling real-world damping, the model performs well at this distance.

Additionally, Figs. 5.10 and 5.11 provide a detailed view of SEL and L_{peak} values at 750 meters from the monopile, respectively, highlighting the variability among the different hydrophones. The spread in measured SEL values is approximately 4 dB, and for L_{peak}, the spread is approximately 3.5 dB. By using the average of these four hydrophones, this study does not consider differences in azimuthal directions.

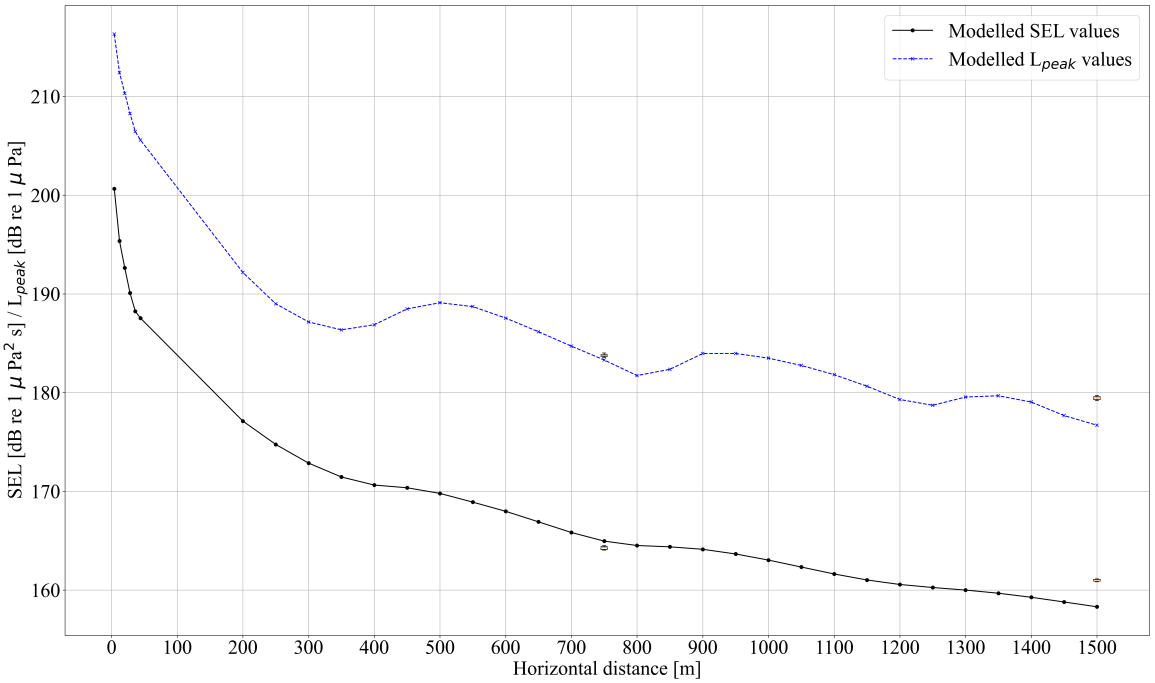

Figure 5.9: Comparison of modelled SEL and L_{peak} values with measurements for PULSE without additional mitigation measures. The blue line represents the modelled L_{peak} values, the black line represents the modelled SEL values, and the average measurements are visualised using a boxplot.

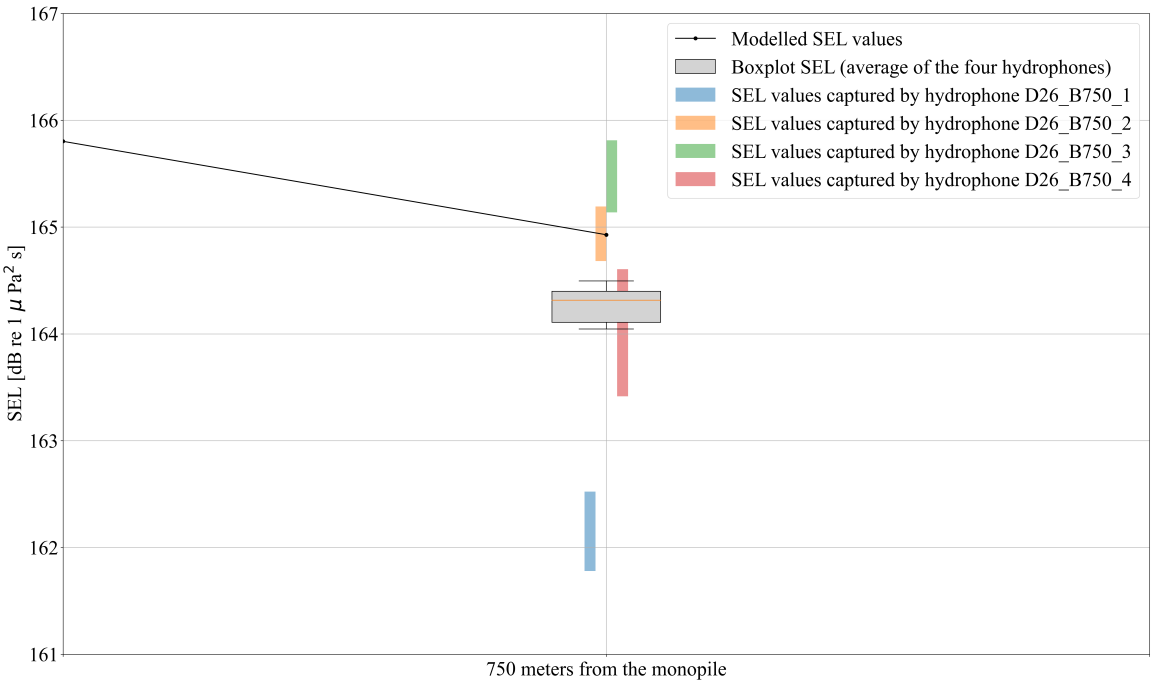

Figure 5.10: Detailed view of SEL values at 750 meters from monopile D26 highlighting the variability among the hydrophones.

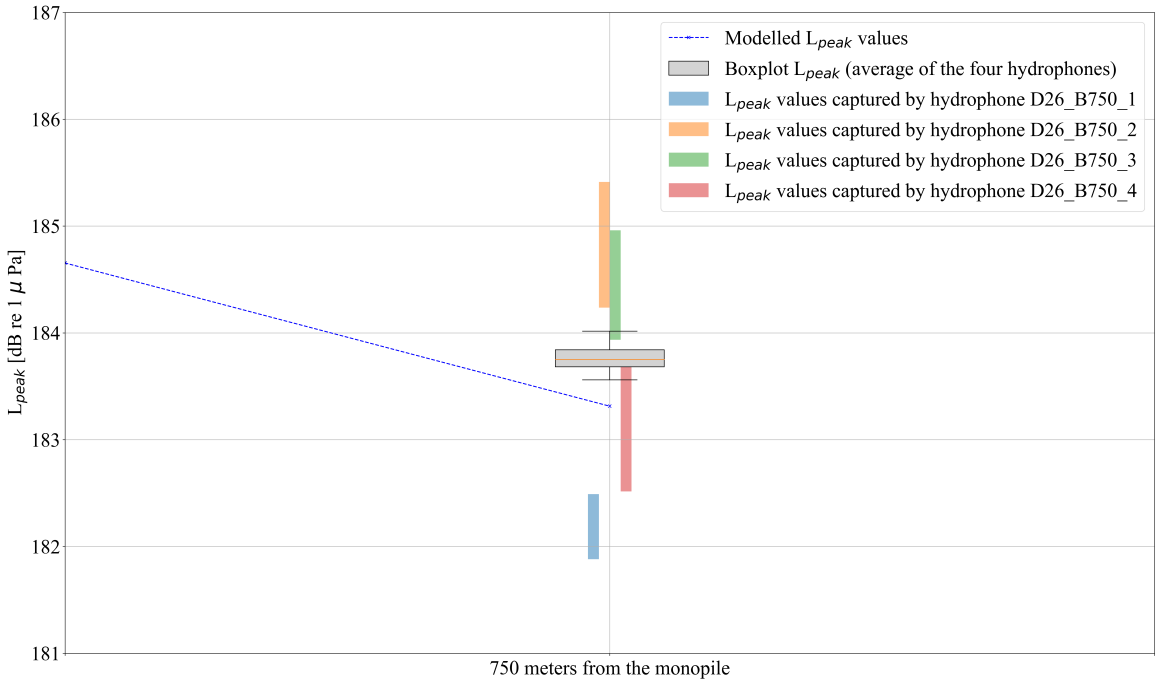

Figure 5.11: Detailed view of L_{peak} values at 750 meters from monopile D26 highlighting the variability among the hydrophones.

Spectral analysis

To compare the model with the field data more in-depth, the data can be analysed qualitatively by examining the system's frequency response, ensuring good broadband correspondence. The SEL values per 1/3 octave band are calculated through a systematic approach. Initially, the pressure values corresponding to each frequency are obtained from the model. These frequencies are then divided into 1/3 octave bands, each containing band energy. This process involves grouping the energies of the frequencies within each band to provide a more granular view of the energy distribution. The energy within each band is computed by integrating the squared pressure values over the frequency range within that band. This integration represents the cumulative energy of the pressures within the specified frequency range, ensuring an accurate representation of the energy distribution across the frequency spectrum. With the pressures for each 1/3 octave band known, these values can be transformed into SEL values:

$$\text{SEL} = 10\log_{10}\left(\frac{\text{Band energy}}{\text{Reference energy}}\right) = 10\log_{10}\left(\frac{\text{Band energy}}{p_{\text{ref}}^2}\right) \tag{5.12}$$

Fig. 5.12 compares the modelled 1/3 octave band SEL values with field data averaged over four hydrophones, also presenting the individual hydrophone recordings for completeness. The measurements are obtained by transforming the time series to the frequency domain, a process already performed by itap due to the confidentiality of the time-domain data. While the model accurately predicts the overall trend, several notable discrepancies exist. Firstly, there is an overestimation at lower frequencies, suggesting that the modelled impulse may contain more low-frequency content than the actual measurements. This discrepancy may be due to the boundary condition choices for the monopile, as low frequencies are sensitive to the pile's configuration. Conversely, the model exhibits an earlier drop in SEL values at higher frequencies, indicating it may not be capturing all the high-frequency energy present in the measurements. This could be attributed to the model only considering the first 1000 frequencies. Additionally, the sharp peaks observed in the actual PULSE force-time diagrams are not represented in the simplified force-time diagram used in this study, which employs larger time steps. Furthermore, the field data may include multiple noise sources (e.g., ship noise, marine life, etc.),

whereas the model accounts only for pile driving noise. It should be emphasised that these points are speculative.

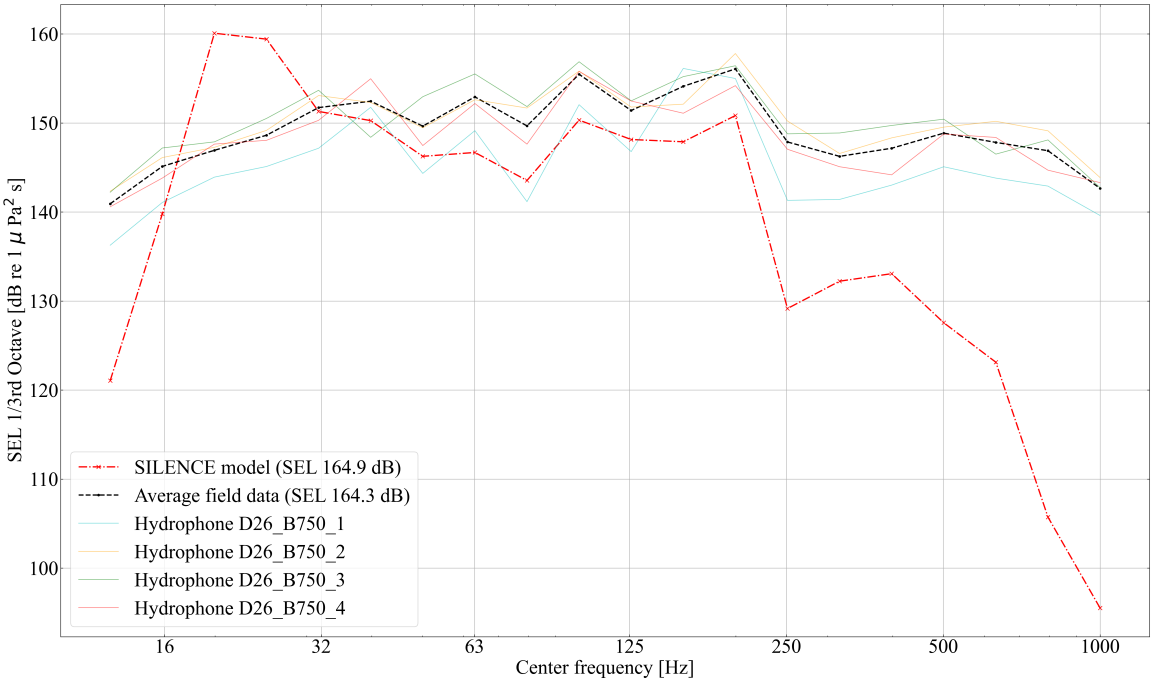

Figure 5.12: Comparison of modelled and measured SEL values per 1/3 octave band for PULSE without additional mitigation measures. The black dashed line represents the average field data over the four hydrophones, while the red dash-dot line represents the modelled values from the SILENCE model. The light blue, orange, green, and red lines represent the individual recordings from hydrophones 1, 2, 3, and 4, respectively.

5.3.2. PULSE combined with air-bubble curtains

Specifications of the monopile location

Fig. 5.13 illustrates the location of monopile D16 along with the positions of the hydrophones used for data collection. The relevant hydrophones are labelled *D16_B750_1* through *D16_B750_4*.

Figure 5.13: Location of monopile D16 and the associated measurement positions. Relevant hydrophones are labelled *D16_B750_1* through *D16_B750_4* [27].

Determination of the blow energy

As mentioned earlier, two criteria must be met to determine the appropriate number of blows to be considered in the analysis. According to the piling data for monopile D16 [23], 33 blows were required to drive the monopile the final 25 cm into the ground, thereby achieving the final penetration depth. To meet the second criterion, the SEL and L_{peak} values must remain relatively stable during the number of blows considered. Fig. 5.14 presents the SEL measurements over time, while Fig. 5.15 displays the L_{peak} measurements over time. These figures indicate that the sound level measurements remain relatively stable, supporting the validity of considering 33 blows for the analysis.

Additionally, Appendix A presents individual recordings from the four hydrophones, capturing both SEL and L_{peak} values. These recordings are valuable for assessing the azimuthal direction spread, illustrating directional differences. While these differences are not individually analysed in this study, the recordings are included to demonstrate their presence.

The blow energy for the required 33 blows can now be examined. These blow energies are documented in the piling data report for monopile D16 [23]. This analysis considers the minimum, mean, and maximum blow energies. The blow energies for monopile D16 are as follows:

- Minimum blow energy: 555 kJ
- Mean blow energy: 560 kJ
- Maximum blow energy: 579 kJ

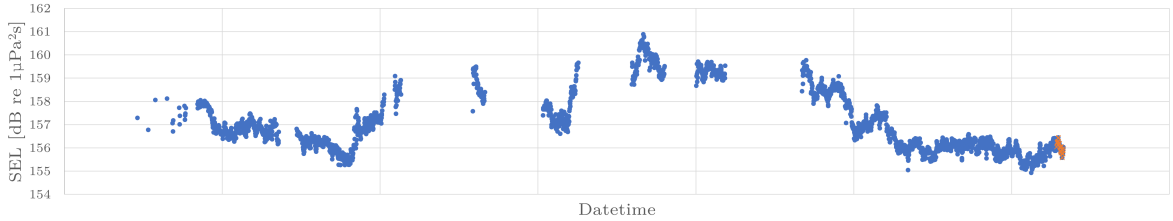

Figure 5.14: SEL measurements for monopile D16 monitored over time, depicting the average from the four hydrophones. The orange part highlights the blows necessary for the final 25 cm penetration.

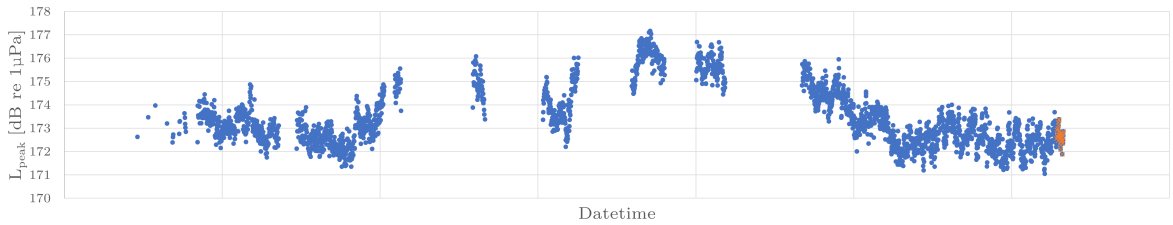

Figure 5.15: L_{peak} measurements for monopile D16 monitored over time, depicting the average from the four hydrophones. The orange part highlights the blows necessary for the final 25 cm penetration.

Energy input into the pile

The energy input for the measurements is determined by multiplying the mean blow energy of the last 33 blows by the efficiency of the *maximum PULSE* setting. The energy input into the pile, referred to as ENTHRU, is obtained as follows:

$$\text{ENTHRU} = \text{Mean blow energy} \cdot \text{efficiency} = 560\,\text{kJ} \cdot 0.66 = 370\,\text{kJ}$$

The energy distribution along the length of the pile is illustrated in Fig. 5.16. Key interfaces are indicated with dotted lines: the blue line represents the air-water interface, the first brown line marks the water-soil interface, and the second brown line denotes the soil-soil interface. The red dotted line represents the derived ENTHRU. As depicted in the figure, the derived ENTHRU aligns closely with the energy modelled along the first meters of the pile. This alignment indicates that the modelled energy input into the pile corresponds accurately to the derived ENTHRU, demonstrating the model's accuracy in simulating the energy distribution during piling operations.

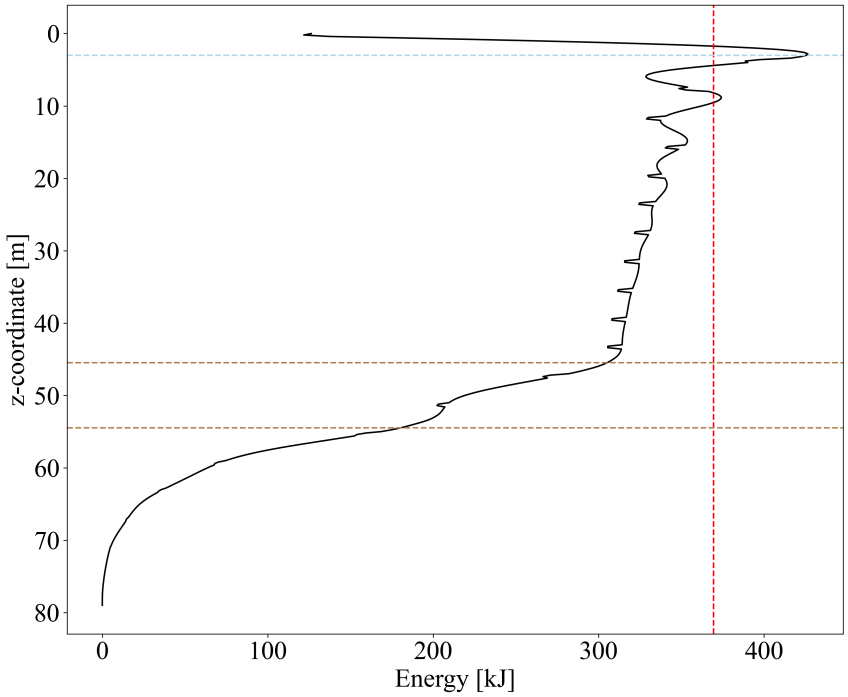

Figure 5.16: Total energy distribution along the pile length after a single hammer blow at the final penetration depth for PULSE combined with air-bubble curtains. The red dotted line represents the measured ENTHRU.

Arrival time of the impulse

The arrival time of the impulse must be examined to validate the transformation from the frequency domain results to the time domain results. According to the theoretical predictions discussed in Section 5.3.1, the impulse is expected to arrive after approximately 0.5 seconds. Fig. 5.17 illustrates the pressure evolution of the modelled impulse over time. The signal's arrival time can be observed around 0.5 seconds, aligning with the theoretical predictions and confirming the validity of the transformation.

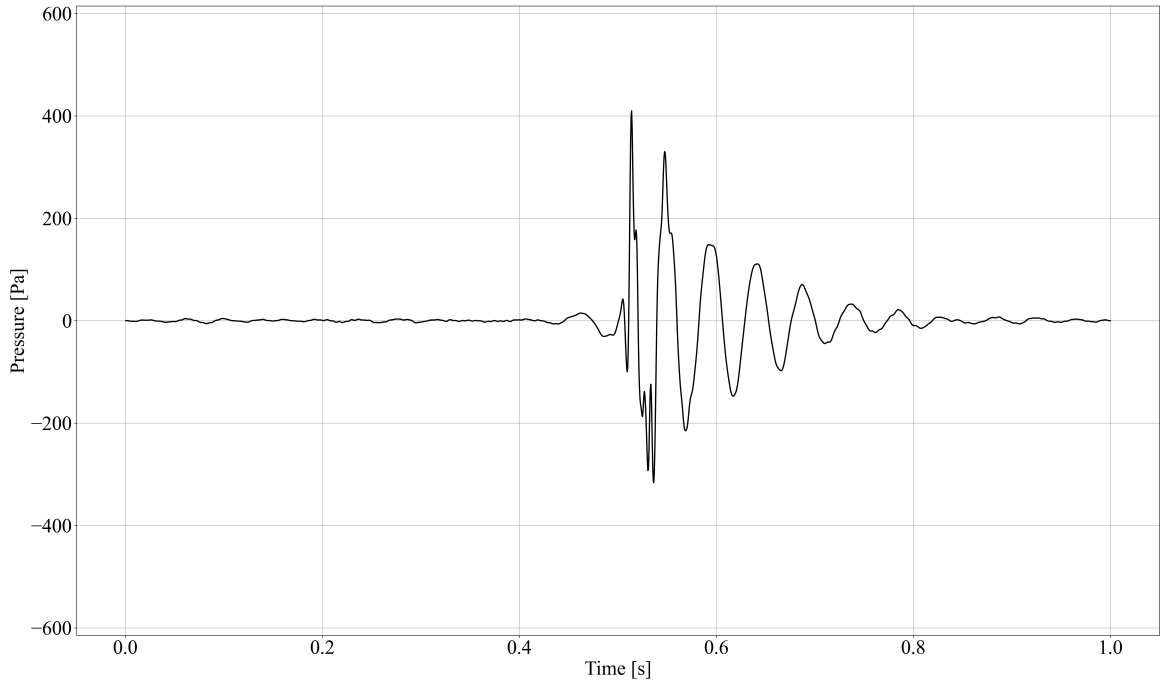

Figure 5.17: Pressure evolution of the modelled impulse in time for PULSE combined with air-bubble curtains. The impulse should arrive at 750 meters at 2 meters above the seabed after approximately 0.5 seconds

Sound Exposure Level and Sound Peak Level

Fig. 5.18 presents the modelled SEL and L_{peak} values over the horizontal distance from the monopile, compared with field data for D16. The average readings from four hydrophones for the last 33 blows are illustrated using a boxplot. The data show a decreasing trend in both sound levels as the distance from the monopile increases. At 750 meters, the model underestimates the average SEL measurement by 0.5 dB and the average L_{peak} measurement by 0.4 dB. This close agreement suggests that the model performs well in predicting noise levels at a significant distance from the source. The deviations fall within the uncertainty range of the results, which stems from inherent uncertainties in the parameter values, primarily soil parameters, and measurements [49].

To evaluate the accuracy of the soil model, SEL and L_{peak} values were modelled up to 1500 meters, where measurements are also available. The SEL values continue to show good correspondence, with the model underestimating the measurements by 2.6 dB. For L_{peak}, the model overestimates the measurements by only 0.3 dB, indicating very good correspondence. The 2.6 dB underestimation for SEL is primarily influenced by the choice of damping. Due to the inherent uncertainty and difficulty in accurately representing real damping, the model demonstrates quite good performance at this distance.

Additionally, Figs. 5.19 and 5.20 provide a detailed view of SEL and L_{peak} values at 750 meters from the monopile, respectively, highlighting the variability among the different hydrophones. The measured SEL values have a spread of approximately 4.5 dB, while the L_{peak} values spread approximately 5 dB. This study does not account for differences in azimuthal directions by averaging these four hydrophone readings.

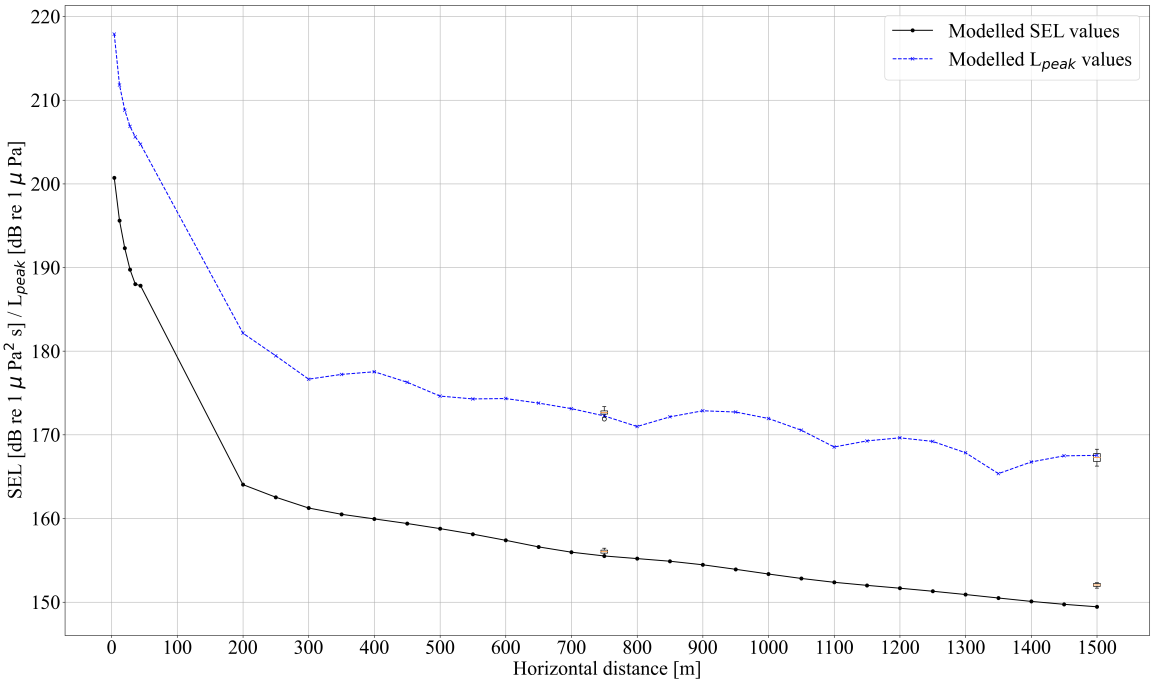

Figure 5.18: Comparison of modelled SEL and L_{peak} values with measurements for PULSE combined with air-bubble curtains. The blue line represents the modelled L_{peak} values, the black line represents the modelled SEL values, and the measurements are visualised using a boxplot.

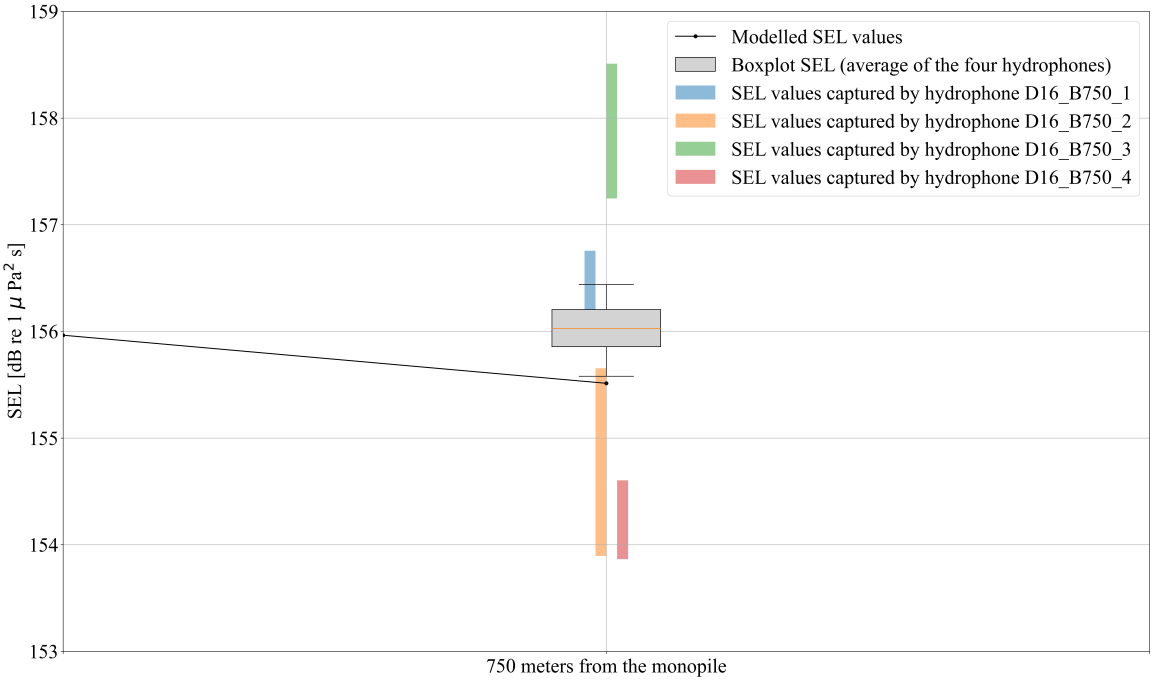

Figure 5.19: Detailed view of SEL values at 750 meters from monopile D16 highlighting the variability among the hydrophones.

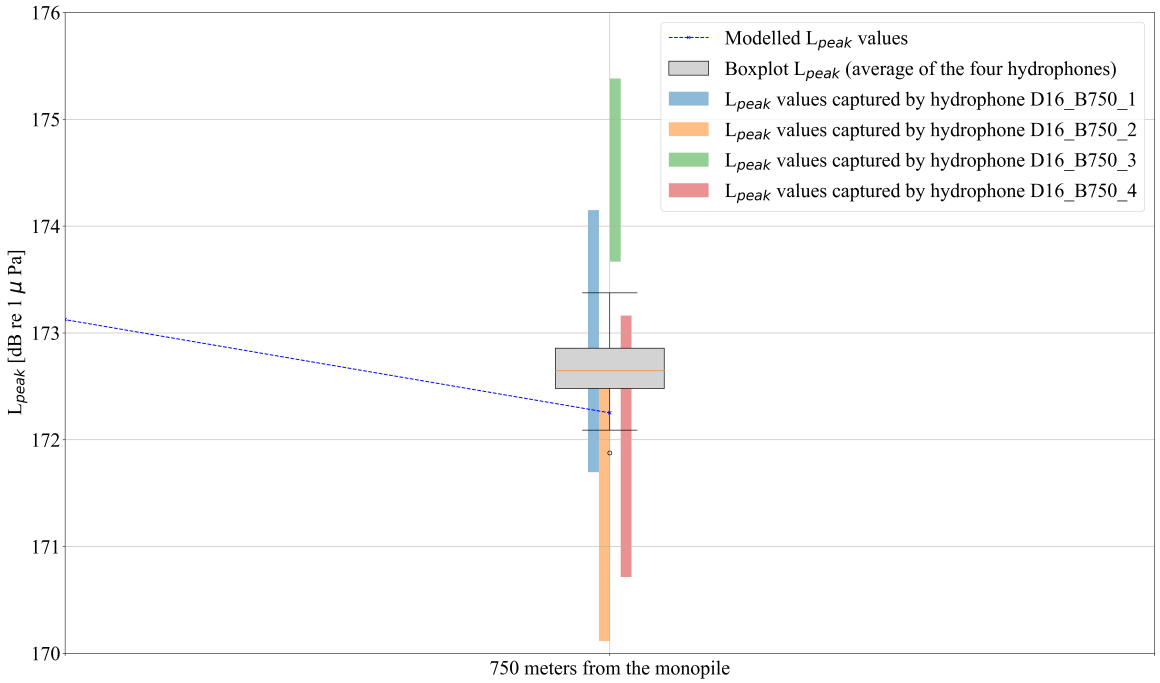

Figure 5.20: Detailed view of L_{peak} values at 750 meters from monopile D16 highlighting the variability among the hydrophones.

Spectral analysis

Fig. 5.21 compares the modelled and measured SEL values, averaged over the four hydrophones, across 1/3 octave bands. The individual hydrophone recordings are also shown for completeness. The alignment between the model and measurements is notably accurate in the mid-frequency range. Both the model and the measurements generally follow the same trend: SEL values increase at lower frequencies, remain relatively stable in the mid-frequency range, and then decrease at higher frequencies. However, the model shows a noticeable peak below 32 Hz that is not present in the measurements. This discrepancy suggests that the model might overestimate the energy at low frequencies, or that the measurements might underrepresent this energy. These differences can be attributed to the same reasons outlined in Section 5.3.1.

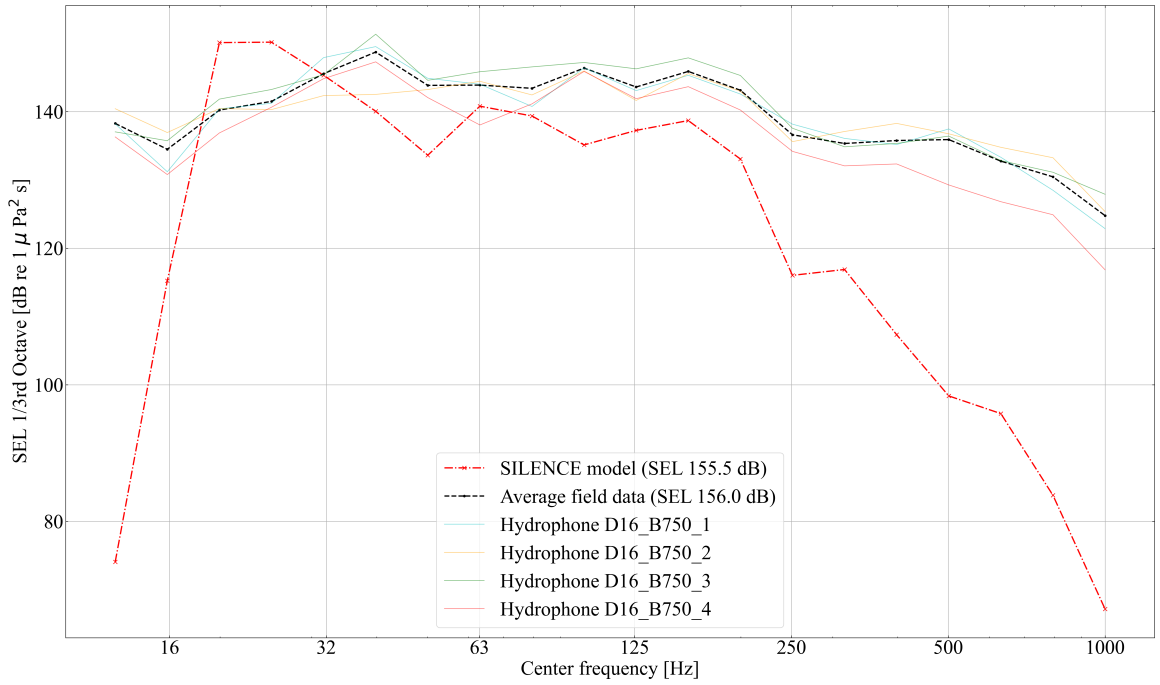

Figure 5.21: Comparison of modelled and measured SEL values per 1/3 octave band for PULSE combined with air-bubble curtains. The black dashed line represents the average field data over the four hydrophones, while the red dash-dot line represents the modelled values from the SILENCE model. The light blue, orange, green, and red lines represent the individual recordings from hydrophones 1, 2, 3, and 4, respectively.

5.4. Dynamics and energy flux of the monopile

Establishing an acceptable correspondence between the model and the measurements allows for the exploration of the effects of elongating the impulse using different PULSE settings. This analysis uses monopile D16 to ensure a consistent basis for comparison between the different PULSE settings. The input parameters for this monopile are discussed in Section 5.2. This section discusses the effects of impulse elongation on the monopile.

5.4.1. Impact of PULSE settings on the energy flux

Figs. 5.22 to 5.24 illustrate the energy flux at three positions along the length of the monopile for each PULSE setting, all corresponding to the same blow energy (i.e., the mean blow energy used for D16 as described in Section 5.3.2) and accounting for the efficiency of the *maximum PULSE* setting. The energy flux through a cross-section at location z_0 of the monopile due to the compressional motion of the pile can be estimated by the product of the normal force in the pile and the vertical velocity of the mid-surface of the pile, multiplied by the area of the cross-section [60], given in Eq. (4.1).

From the figures, it can be seen that the case without PULSE produces the highest amplitude peak and the shortest duration peak. This indicates that when the *no PULSE* setting is applied, the energy delivered to the pile is both more intense and more transient. Conversely, the energy flux in the pile when applying *minimum*, *medium*, and *maximum PULSE* settings shows a smaller amplitude but a longer duration. By elongating the duration of the impulse, the energy is spread over a longer period, reducing the instantaneous peak force and suggesting a more sustained transfer of energy into the pile. This pattern aligns with the characteristics of the different PULSE settings in the input force as depicted in Fig. 5.1.

Additionally, it can be observed that the reflections of the energy flux, which occur when the impulse reflects at the tip of the pile, are larger in amplitude without using PULSE. However, the duration of these reflections is shorter. This behaviour indicates that while PULSE settings reduce the peak amplitude of the energy flux, they prolong the presence of the impulse within the pile.

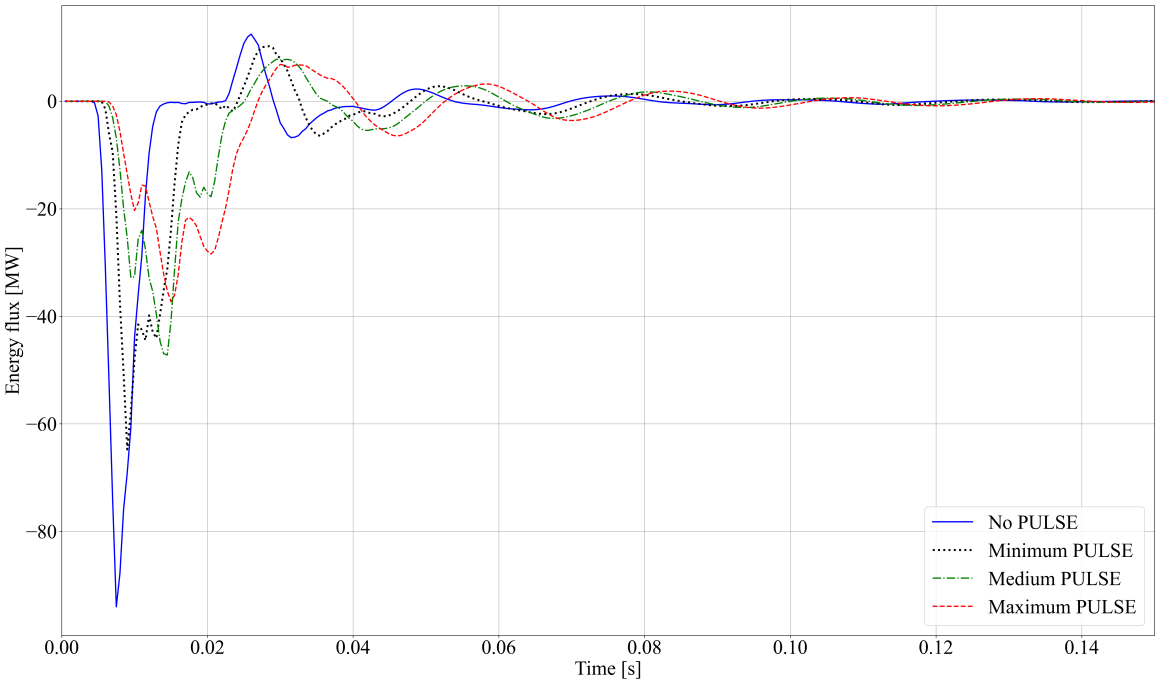

Figure 5.22: Comparison of the energy flux at 0.1 times the pile length from the top for all PULSE settings.

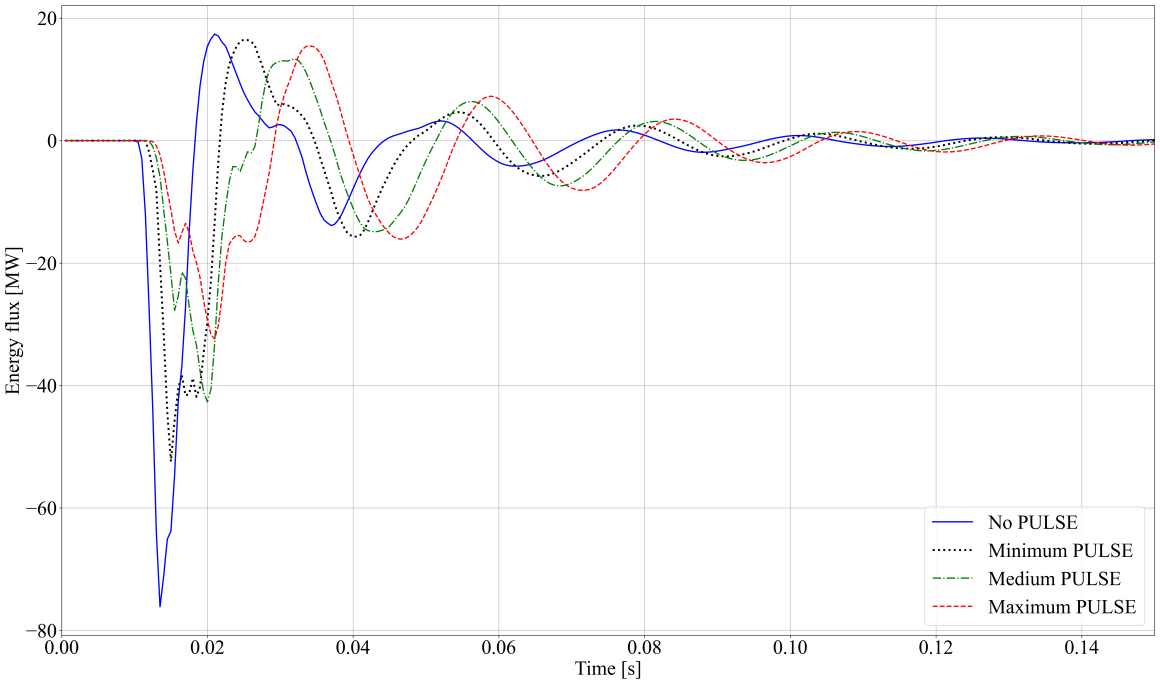

Figure 5.23: Comparison of the energy flux at 0.5 times the pile length from the top for all PULSE settings.

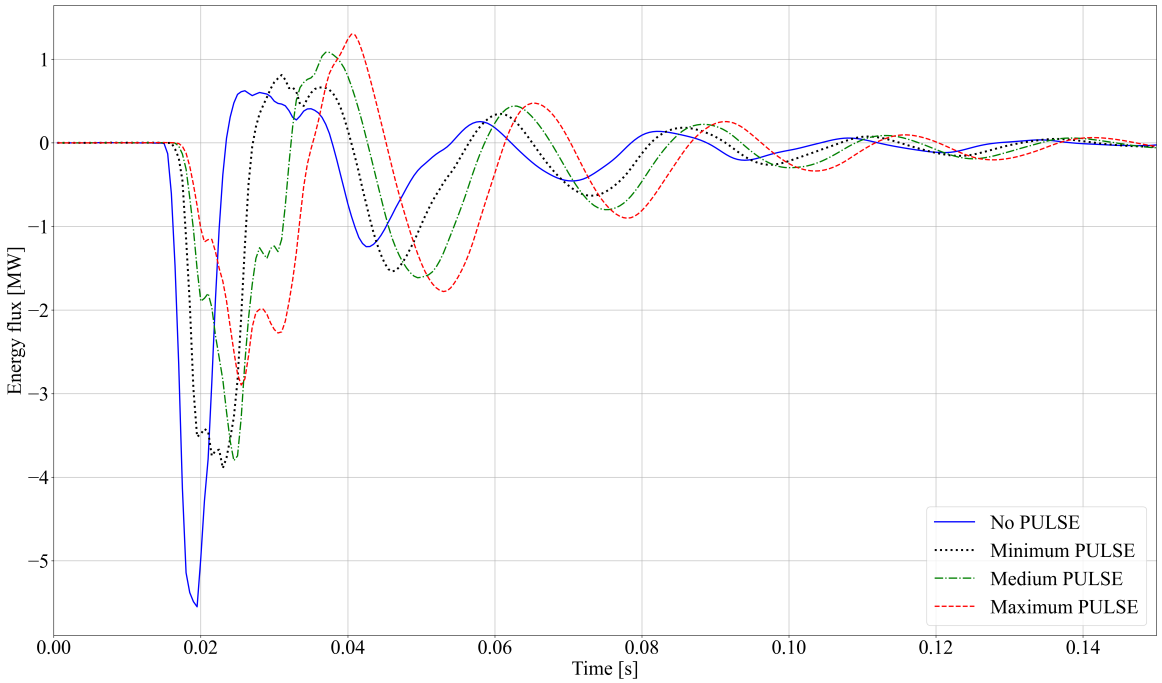

Figure 5.24: Comparison of the energy flux at 0.8 times the pile length from the top for all PULSE settings.

5.4.2. Pile vibrations in radial and vertical directions

The analysis of pile vibrations further clarifies the impacts of different PULSE settings on the pile's dynamics. The pile vibrations in both the radial and vertical directions at various vertical locations along the pile are analysed. The pile vibrations in both directions are shown in Appendix B at 3 locations of the pile: 0.1, 0.5, and 0.8 times the length of the pile.

When the impulse is elongated, the frequency content of the force changes, introducing more low-frequency components. Lower frequencies cause the entire pile to move more coherently, resulting in larger overall displacements. These low-frequency vibrations have longer wavelengths and dissipate more slowly, causing the vibrations to persist longer and exhibit higher peaks compared to the *no PULSE* setting, where higher frequency vibrations dominate and dissipate more quickly. Similarly, in the radial direction, elongated impulses result in larger displacement amplitudes due to the increased low-frequency content.

Overall, elongating the impulse leads to larger and longer vibrations in both the radial and vertical directions of the pile. This indicates that while the peak force is reduced, the energy includes lower frequency components, resulting in greater displacements. This behaviour underscores the importance of considering both the frequency content and duration when analysing pile dynamics under different PULSE settings. Lower frequency components are particularly influential in causing larger displacements, while higher frequency components contribute to higher strains but not necessarily larger overall displacements.

5.5. Wave radiation into the exterior domain

The next part of the analysis examines the effects of impulse elongation on the radiated underwater noise. This section first analyses the different impulses in the time domain and the energy distribution in the water and soil domains. Following this, the sound levels generated by different impulse elongations are evaluated. Assessing the sound levels and their corresponding frequency responses provides both quantitative and qualitative measures of the effectiveness of each PULSE setting. This analysis is conducted first for PULSE alone in Section 5.5.1, then for PULSE combined with a BBC in Section 5.5.2, and finally for PULSE combined with a DBBC in Section 5.5.3. Monopile D16 is used for all three sections to ensure a consistent basis for comparison.

5.5.1. PULSE without additional mitigation measures

Evolution of the radiated impulse in time

Fig. 5.25 illustrates that regardless of the PULSE setting – whether *zero*, *minimum*, *medium*, or *maximum* – the arrival times of the impulses are identical. This confirms that elongation does not alter the speed of propagation. The consistent arrival time is due to the speed of sound in water and the distance the impulse travels, which are unaffected by the PULSE settings. Furthermore, all signals exhibit approximately the same temporal pattern but with varying amplitudes and periods. The smaller amplitude for longer impulse elongations occurs because the energy is applied more gradually, leading to a lower peak pressure over a longer duration. This temporal analysis confirms that while impulse elongation does not affect the arrival time, it results in decreased amplitude and increased duration for longer impulses.

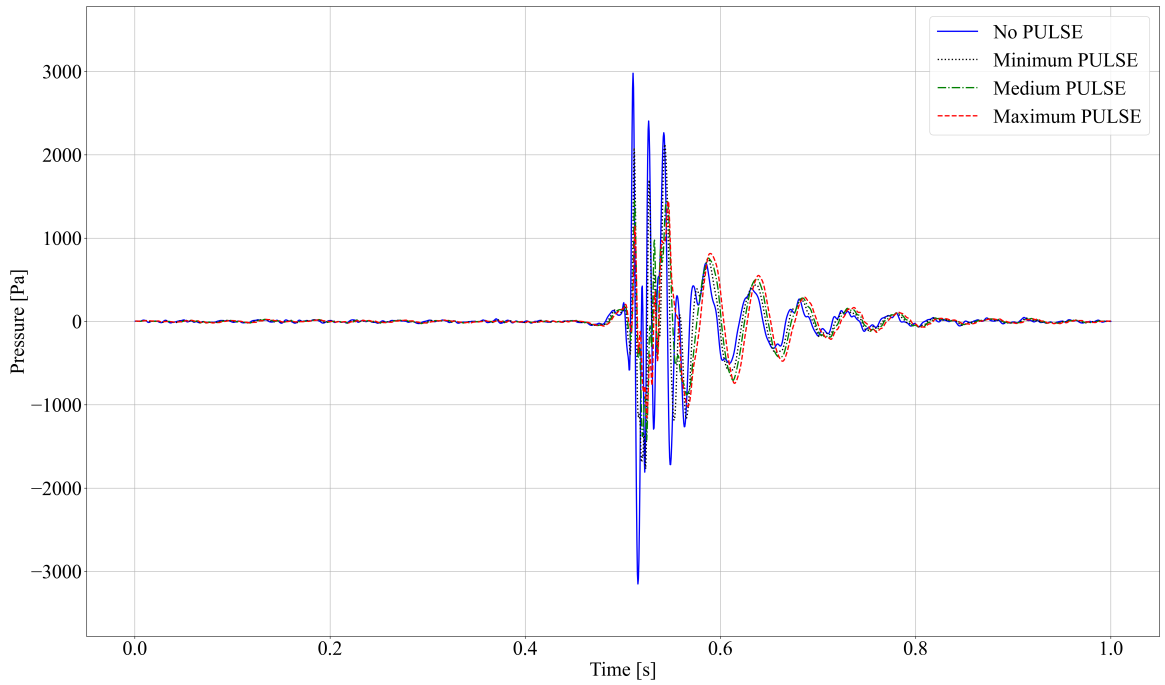

Figure 5.25: Time evolution of the modelled pressure for different PULSE settings without additional mitigation measures. The impulse is expected to reach 750 meters after approximately 0.5 seconds.

Energy introduced into the exterior domain

The energy introduced into the water by impact piling helps in understanding and quantifying the different types of waves generated. The distribution of energy in the water changes with varying energy inputs into the pile. This energy distribution can be quantified by examining the instantaneous power[2] radiated through a cylindrical surface positioned at a certain distance from the pile. The calculation of this instantaneous power in the fluid involves the surface integral of the normal component of acoustic intensity [60]:

$$P_w\left(r_0,t\right)=\oint_S I_n\left(r_0,z,\theta,t\right)dS=\oint_S p_f\left(r_0,z,\theta,t\right)v_{f,n}\left(r_0,z,\theta,t\right)dS \tag{5.13}$$

In this equation, $p_f\left(r_0,z,\theta,t\right)$ represents the pressure in the time domain in the fluid; as this is a scalar quantity, it has no direction. Furthermore, $v_{f,n}\left(r_0,z,\theta,t\right)$ represents the particle velocity in the time domain normal to S.

Figs. 5.26 to 5.28 show the instantaneous power in the water region at different horizontal distances from the monopile surface. It can be observed that there are two clear blocks of energy, except for Fig. 5.26, where both blocks are indistinguishable. These two blocks represent different types of waveforms: the first block corresponds to the pressure waves, and the second block corresponds to the Scholte waves. The Scholte waves appear later due to their lower wave speed. The pressure waves show much larger amplitudes than the Scholte waves.

The figures clearly illustrate the differences between the PULSE settings. The *no PULSE* setting shows the highest peak energy in the initial energy block. As the PULSE duration increases from *minimum* to *maximum*, the peak energy of the pressure waves significantly decreases. This change indicates that elongating the impulse duration substantially reduces the energy carried by the pressure waves. Conversely, the energy in the Scholte waves does not decrease proportionally with the increase in impulse duration. Instead, the energy of the Scholte waves shows a slight increase. Scholte waves, which are lower in frequency compared to compressional waves, benefit from elongated impulses. The resulting waveform contains more low-frequency components, which couple more effectively into Scholte waves, allowing them to propagate more efficiently in this frequency range. In summary, the analysis of instantaneous power in the water region reveals that adjusting the PULSE settings can effectively reduce the energy of pressure waves while slightly increasing the energy of Scholte waves.

Analysing the acoustic energy distribution in the water and soil regions provides additional insights into the problem. This is accomplished by examining the energy passing through a cylindrical surface S. The instantaneous power is integrated over time for both the water and soil regions, as shown in Eqs. (5.14) and (5.15) respectively [60].

$$\mathrm{E}_{f,n}\left(r_0\right)=\int_{t_0}^{t_0+T}P_w\left(r_0,t\right)dt=\int_{t_0}^{t_0+T}dt\oint_S p_f\left(r_0,z,\theta,t\right)v_{f,n}\left(r_0,z,\theta,t\right)dS \tag{5.14}$$

$$\mathrm{E}_{s,n}\left(r_0\right)=\int_{t_0}^{t_0+T}P_s\left(r_0,t\right)dt=\int_{t_0}^{t_0+T}dt\oint_S \mathbf{t}_s\cdot\mathbf{v}_s dS \tag{5.15}$$

Fig. 5.29 illustrates the total radiated energy in the water region, soil region, and the cumulative energy away from the pile for the four analysed PULSE settings. The figures reveal that up to a certain point, acoustic energy in the water region increases while it decreases in the soil region. This occurs because part of the energy radiates deeper into the soil and diminishes, and part of the energy is transferred from the soil to the water region due to reflections between soil layers. This transfer also results in an increase in acoustic energy around the water-soil interface, which was observed in Figs. 5.27 and 5.28 as well where the Scholte waves obtained slightly more energy when moving further from the monopile.

[2]The instantaneous power refers to the rate at which acoustic energy is transmitted through a specified surface area in the fluid at any given moment. It represents the real-time measurement of acoustic energy flow due to the impact piling.

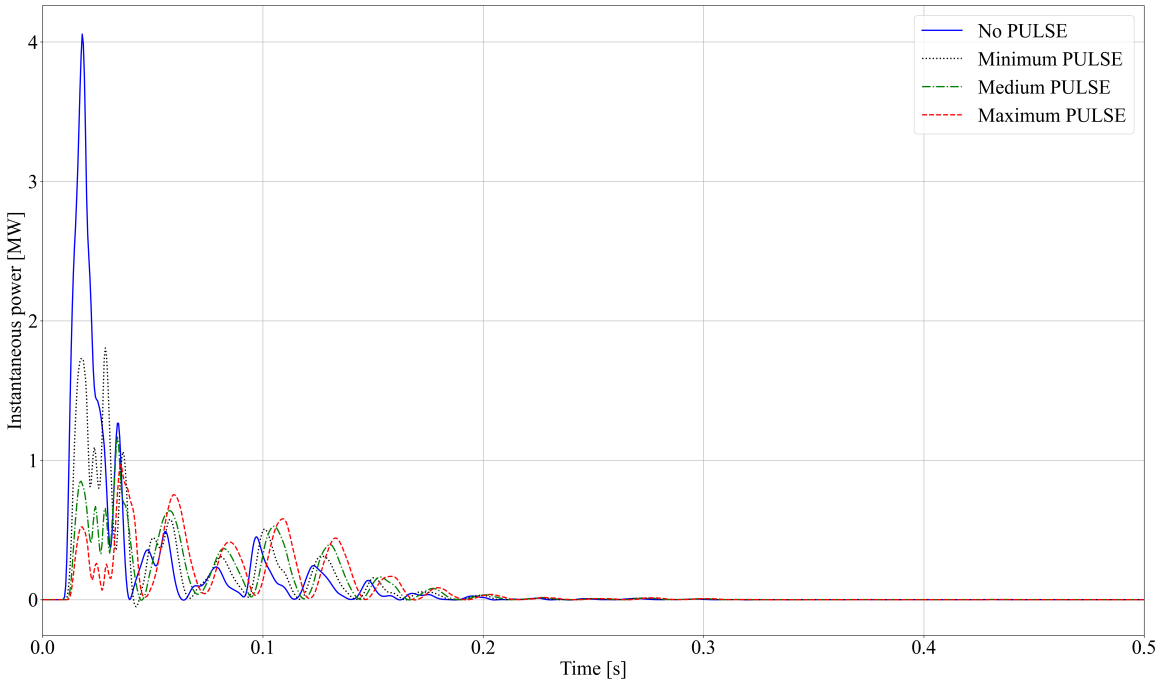

Figure 5.26: Instantaneous power in the water region at 12.25 m from the monopile for different PULSE settings.

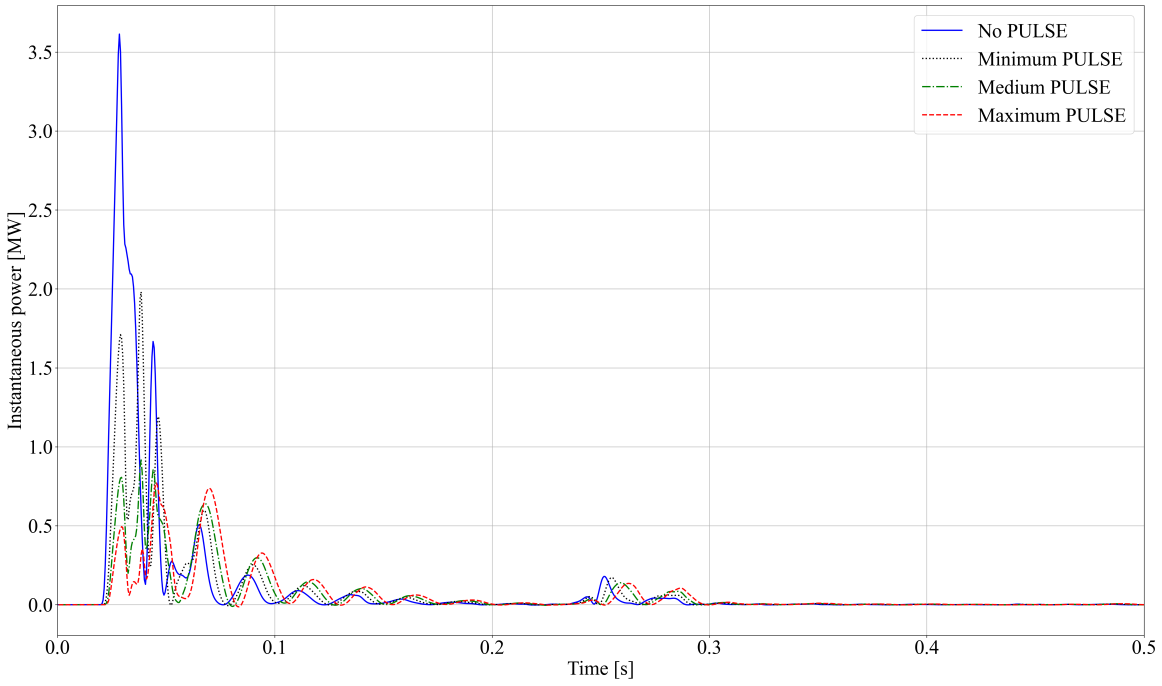

Figure 5.27: Instantaneous power in the water region at 28.25 m from the monopile for different PULSE settings.

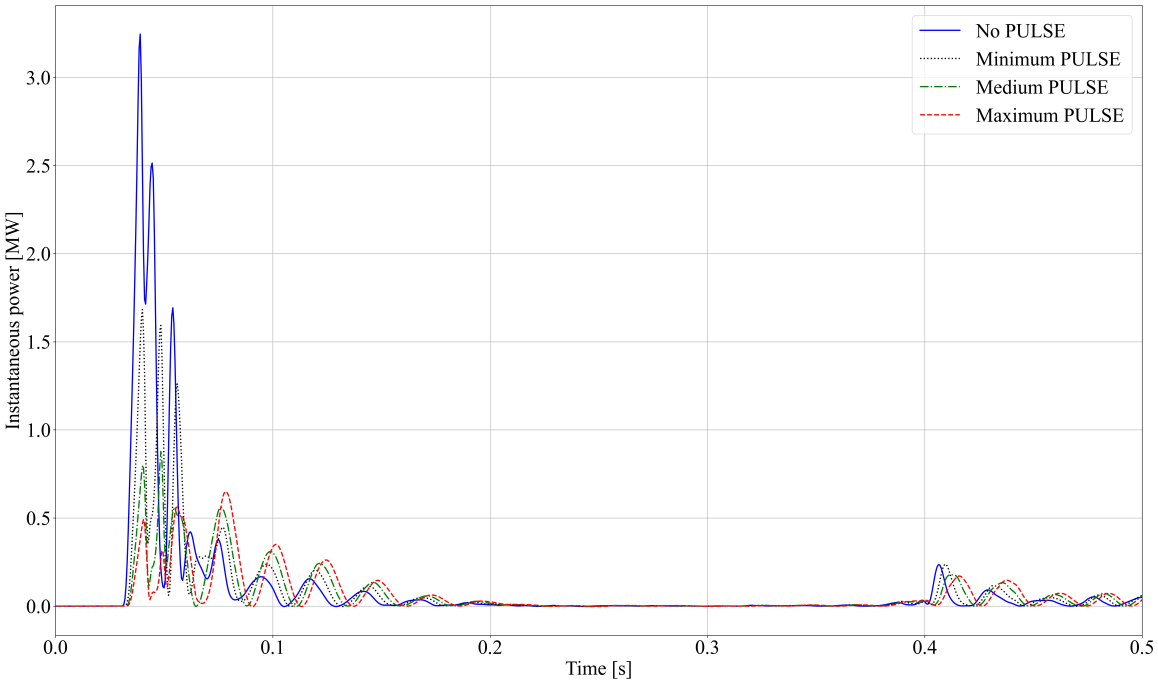

Figure 5.28: Instantaneous power in the water region at 44.25 m from the monopile for different PULSE settings.

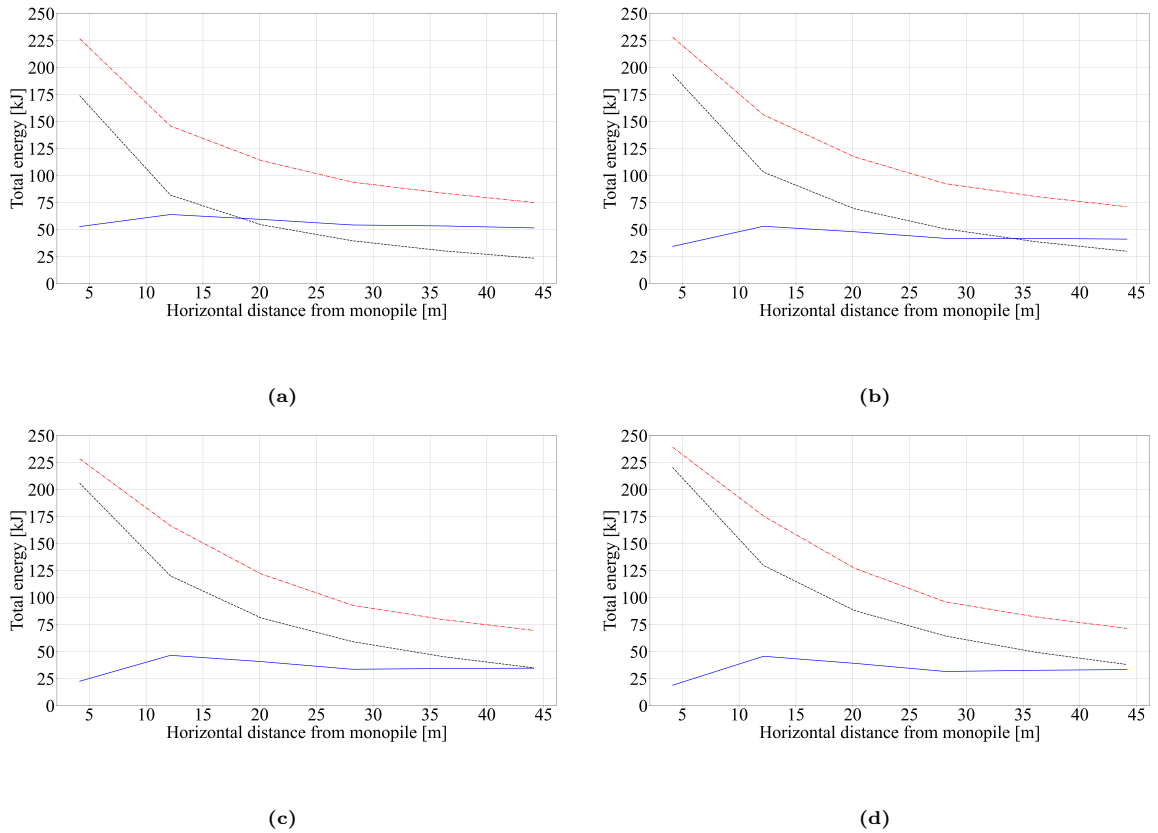

Figure 5.29: Total radiated energy in the water region, soil region, and the cumulative energy for the four different PULSE settings: (a) *no PULSE*, (b) *minimum PULSE*, (c) *medium PULSE*, and (d) *maximum PULSE*. The blue solid line represents the water region, the black dashed line represents the soil region, and the red dash-dotted line represents the cumulative energy.

Furthermore, with longer impulse elongation, the transfer of energy from the soil to the water region takes more time. This delayed transfer occurs because longer impulses distribute their energy over an extended period, resulting in a gradual energy transfer. This reduces the immediate energy transfer rate, leading to a delayed but sustained release of energy from the soil to the water. A slower transfer rate allows more energy to pass through the mitigation measures in the water column. Consequently, more energy may leak into the water column past the mitigation measures, potentially having a negative effect at larger distances from the monopile.

Additionally, it can be observed that there are lower energy levels in the water region for longer impulses compared to shorter ones. This is also visible in Fig. 5.30, where the energy fluxes over the height at different distances from the monopile are shown. As the impulse duration increases from *no PULSE* to *maximum PULSE*, there is a noticeable energy redistribution. Specifically, there is a decrease in energy within the water region and an increase in energy within the soil region. This shift indicates that longer impulse durations favour the transmission of energy into the seabed. It is important to understand that this observed energy redistribution is not solely about how energy moves through different media, but more about how changing the input force (i.e., by using different PULSE settings) affects the interaction between the monopile, the surrounding water, and the soil. This interaction is central to the way sound is generated. When the hammer strikes with different force durations, it alters how energy is transferred from the monopile into the surrounding environment.

In shallow-water channels, there is a critical frequency below which the channel stops acting as an effective waveguide. When the frequency components of an impulse fall below this cutoff frequency, the energy does not propagate efficiently through the water but instead is directed into the seabed [29]. Longer impulse durations introduce more low-frequency components, which are more likely to fall below this cutoff frequency. As a result, the energy from these low-frequency components is absorbed by the seabed rather than travelling through the water. This change in energy distribution affects the effectiveness of mitigation measures in the water. For example, although the overall sound level will be lower, the efficiency of mitigation measures, such as air-bubble curtains, will decrease because a larger portion of the energy is transferred into the soil rather than the water.

Therefore, understanding how the input force changes the interaction between the structure, water, and soil is essential. It highlights that the energy balance and the effectiveness of noise mitigation strategies depend on these interaction dynamics.

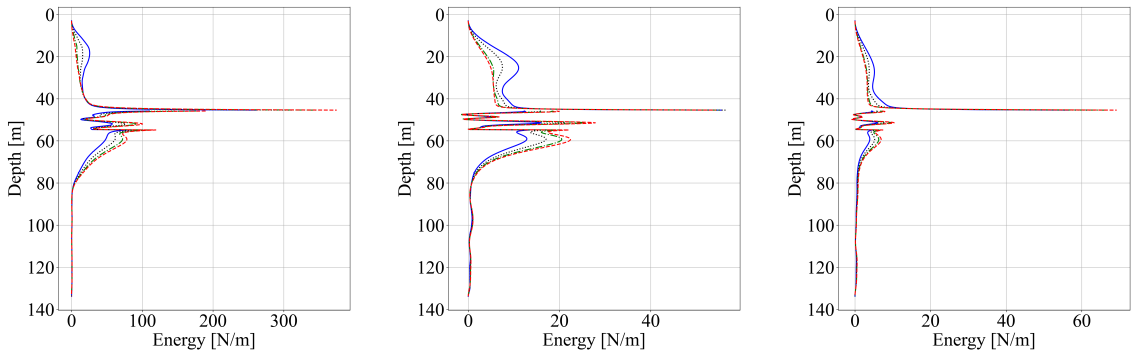

Figure 5.30: Energy flux in the fluid and soil regions at three different distances from the monopile: (a) 12.25 m, (b) 28.25 m, and (c) 44.25 m. The lines represent different PULSE settings: blue solid line for *no PULSE*, black dotted line for *minimum PULSE*, green dash-dotted line for *medium PULSE*, and red dashed line for *maximum PULSE*.

Sound levels of different impulses

The impact of different impulse elongations on sound levels will be assessed quantitatively first. This analysis will calculate the change in sound levels for each PULSE setting relative to the *no PULSE* setting to determine their performance. Subsequently, trends observed in the data will be identified, providing a qualitative analysis of the results. This qualitative assessment pinpoints specific frequency ranges where PULSE is most effective and those where its efficacy diminishes or even inadvertently enhances sound levels.

Figs. 5.31 and 5.32 respectively visualise the SEL and L_{peak} values of the sound waves across various horizontal distances from the monopile. These visualisations illustrate how sound levels change with distance under different PULSE settings. The figures show a general trend: as the impulse elongates, the SEL and L_{peak} values decrease across all distances. This trend suggests that longer impulse elongations are more effective in mitigating underwater noise. Notably, there is a sudden increase in SEL and L_{peak} values after approximately 300-350 meters. This increase results from the complex interaction of acoustic modes, where reflections from the seabed and sea surface temporarily enhance sound levels.

In underwater acoustics, the properties of the medium, such as water depth and seabed composition, influence sound propagation [29]. These factors lead to the formation of discrete acoustic modes, each with specific propagation paths and speeds. When multiple acoustic modes interact, they can interfere constructively or destructively, depending on their phase relationships. Constructive interference occurs when the phases of different acoustic waves align, increasing sound pressure at certain distances [29]. In the context of this study, the increase in SEL and L_{peak} values observed after 300-350 meters results from the constructive interference of multiple acoustic modes. At this distance, the direct and reflected sound waves may be in phase, reinforcing each other and causing a peak in the modelled sound levels.

Table 5.5 provides an overview of the SEL and L_{peak} values for different PULSE settings. The SEL and L_{peak} values are presented for each PULSE setting, along with their respective reductions relative to the baseline scenario *no PULSE*. The data demonstrate that increasing the impulse elongation – moving from *minimum PULSE* to *maximum PULSE* – results in progressively greater reductions in both SEL and L_{peak}. Additionally, the differences in pressure values for each PULSE setting relative to the baseline scenario are presented. Since SEL and L_{peak} values are logarithmic representations of sound levels, they can sometimes be misleading regarding actual changes in sound pressure levels. Therefore, it is crucial to consider both the logarithmic and actual pressure values to assess PULSE's performance accurately.

Table 5.5: Sound levels and reductions relative to the baseline scenario *no PULSE* at 750 meters from the monopile, 2 meters above the seabed, for different PULSE settings without additional mitigation measures.

	SEL [dB re 1 μPa^2]	**SEL reduction** [dB re 1 μPa^2]	**L_{peak}** [dB re 1 μPa]	**L_{peak} reduction** [dB re 1 μPa]	**p_{rms} reduction** [Pa]
No PULSE	171.1	-	190.0	-	-
Min. PULSE	169.5	-1.6	186.6	-3.4	-64
Med. PULSE	167.9	-3.2	183.3	-6.7	-112
Max. PULSE	167.7	-3.4	183.2	-6.8	-119

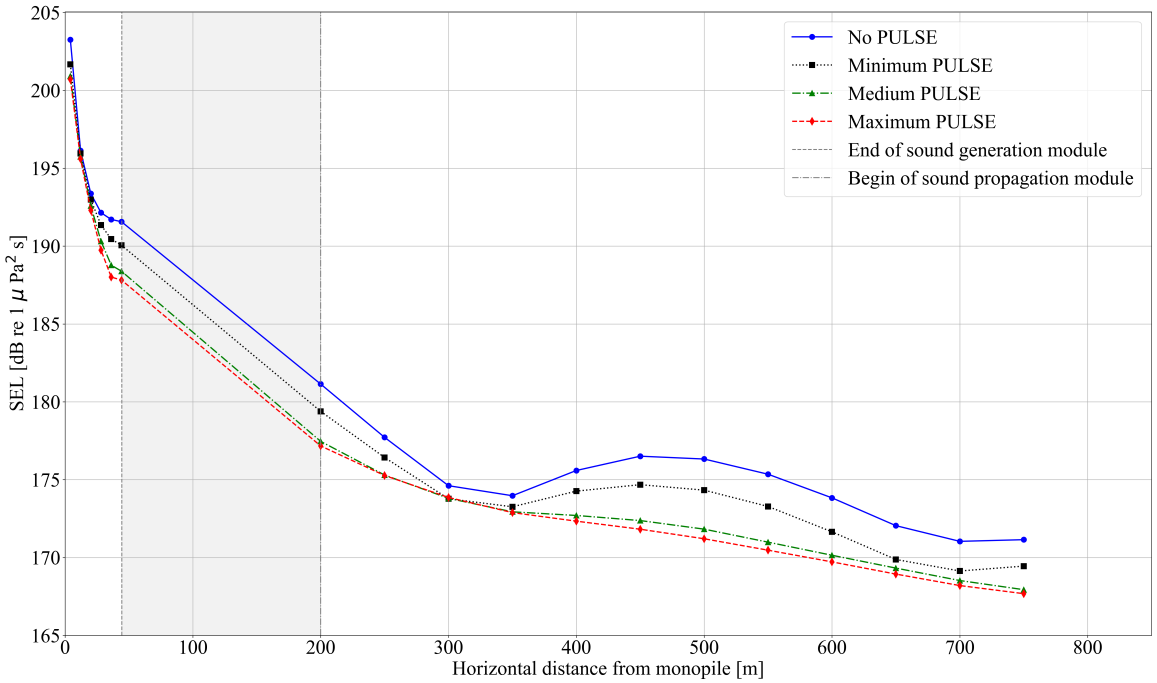

Figure 5.31: Comparison of modelled SEL values for different PULSE settings without additional mitigation measures at various horizontal distances from the monopile.

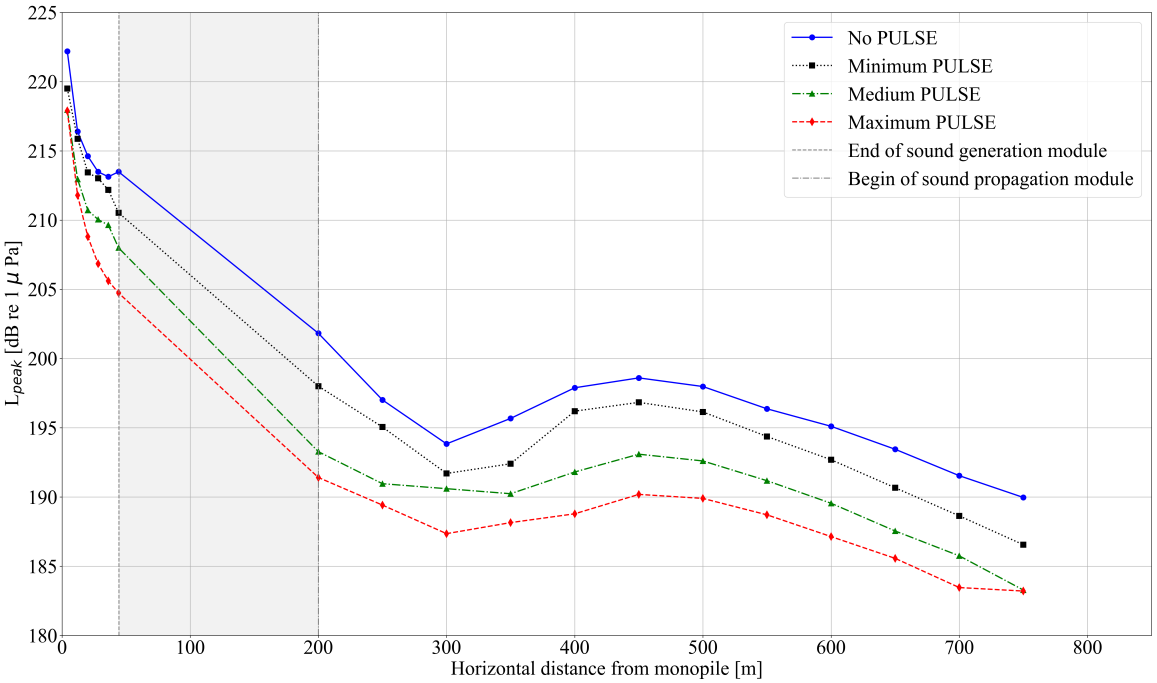

Figure 5.32: Comparison of modelled L_{peak} values for different PULSE settings without additional mitigation measures at various horizontal distances from the monopile.

With the quantitative assessment of the performance of different PULSE settings completed, the next step involves investigating the origins of these differences in sound levels. This can be achieved by analysing the frequency spectra. To understand the frequency spectra for the various PULSE settings, it is essential to begin with the frequency spectrum generated by a unit load, known as the transfer function of the system, as shown in Fig. 5.33. The transfer function represents how the pile-water-soil system responds to a unit load across different frequencies. It is characterised by specific peaks and dips in the spectrum, which correspond to the resonance and antiresonant frequencies of the system, respectively. At antiresonant frequencies, the system does not efficiently transmit energy, resulting in reduced pressure levels. These frequencies arise from destructive interference between the external driving force (i.e., the unit load applied to the monopile) and the reactive forces (i.e., the response of the pile-water-soil system) within the system. This phenomenon occurs due to the superposition of modal responses in opposite phases [30]. Furthermore, it can be observed that below approximately 20 Hz, the pressure levels are significantly reduced. This is due to the system's cutoff frequency, below which no wave propagation is possible.

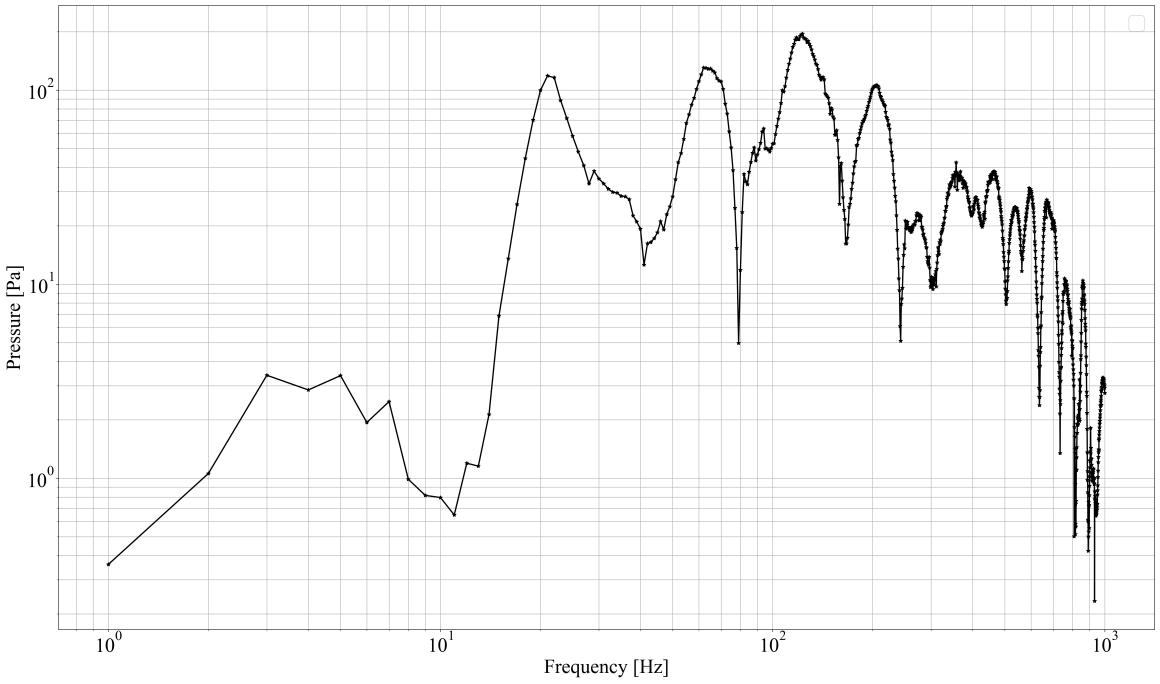

Figure 5.33: Frequency spectrum of the system's response to a unit load, illustrating the transfer function for PULSE without additional mitigation measures, measured 750 meters from the monopile and 2 meters above the seabed.

The next step is to analyse the frequency spectra of the forced systems, which means examining the transfer function multiplied by the input forces of the different PULSE settings. The transfer function of the system is depicted in Fig. 5.33, while the input forces for each PULSE setting are shown in Fig. 5.2. The input forces must be scaled to ensure they deliver the same amount of energy to the pile. This scaling is done using the efficiency of the *maximum PULSE* setting.

The frequency spectra of the forced systems are presented in Fig. 5.34a, with the blue solid line representing the baseline scenario *no PULSE*, the black dotted line showing the *minimum PULSE* setting, the green dash-dotted line illustrating the *medium PULSE* setting, and the red dashed line indicating the *maximum PULSE* setting. Additionally, Fig. 5.34b highlights the differences in the frequency spectrum when comparing each PULSE setting with the baseline scenario.

A positive effect, meaning a decrease in pressure, is observed for almost all frequencies higher than 32 Hz, depending on the PULSE setting. At this frequency (32 Hz), the force amplitude spectrum (Fig. 5.2) shows that the graphs of the elongated impulses and the baseline scenario *no PULSE* intersect. This means that the elongated impulses contain more energy for frequencies lower than 32 Hz than the baseline scenario. Conversely, for frequencies higher than 32 Hz, the energy is lower in the elongated impulses than in the baseline scenario.

To determine the energy redistribution from high frequencies to low frequencies, the total energy in different frequency bands is calculated and compared as follows:

1. **Define frequency bands:** Divide the frequency spectrum into low frequencies (below 32 Hz) and high frequencies (above 32 Hz). This threshold is chosen because it helps determine whether PULSE has a positive or negative effect.
2. **Calculate the energy in each band:** Integrate the square of the pressure amplitude over the respective frequency ranges.

$$E_{\text{low}} = \int_{\text{low band}} p(f)^2 df \tag{5.16}$$

$$E_{\text{high}} = \int_{\text{high band}} p(f)^2 df \tag{5.17}$$

3. **Compare energy redistribution:** Express the energy redistribution as a percentage change relative to the baseline scenario.

$$\Delta E_{\text{low}} = \frac{E_{\text{low, PULSE setting}} - E_{\text{low, baseline}}}{E_{\text{low, baseline}}} \times 100\% \tag{5.18}$$

$$\Delta E_{\text{high}} = \frac{E_{\text{high , PULSE setting}} - E_{\text{high, baseline}}}{E_{\text{high, baseline}}} \times 100\% \tag{5.19}$$

Following this method, the relative energy redistributions to the baseline scenario are calculated and listed in Table 5.6. The table reveals that as the PULSE setting increases from *minimum* to *maximum*, there is an increase in energy at low frequencies and a decrease at high frequencies. These findings confirm that energy shifts from higher to lower frequencies by elongating the impulse.

It must be emphasised that these values are relevant to the baseline scenario. The energy changes in the lower frequency bands are less influential than those in the higher frequencies due to the amplitude differences. As shown in Fig. 5.34a, the amplitudes of the low frequencies are lower, as the axes are logarithmically scaled. Therefore, the energy increase in the low-frequency band is less significant compared to the energy reductions in the high-frequency band, leading to an overall reduction in sound levels.

Table 5.6: Energy redistributions in low and high frequencies for different PULSE settings without additional mitigation measures relative to the baseline scenario *no PULSE*.

PULSE setting	**Low frequencies [%]**	**High frequencies [%]**
Minimum PULSE	+36	-52
Medium PULSE	+65	-87
Maximum PULSE	+78	-94

Furthermore, minor pressure fluctuations around 200 Hz and higher are visible, likely due to small "ripples" in the input forces in the time domain (see Fig. 5.1). These ripples result in higher frequencies being less effectively mitigated by PULSE, as shown in Fig. 5.2, where elongated impulses display more energy around 200 Hz compared to the baseline scenario. The presence of these ripples indicates

rapid changes or discontinuities in the force signal, which translate into high-frequency components in the frequency domain. This occurs because the Fourier Transform analyses the time-domain signal to identify different frequency components. Rapid changes or sharp transitions in the signal require a wide range of high-frequency components for accurate representation. Consequently, these high-frequency components appear in the frequency domain, explaining the observed energy around 200 Hz and minor fluctuations at higher frequencies. These minor deviations are also observable in Fig. 5.34b, although they are quite minimal.

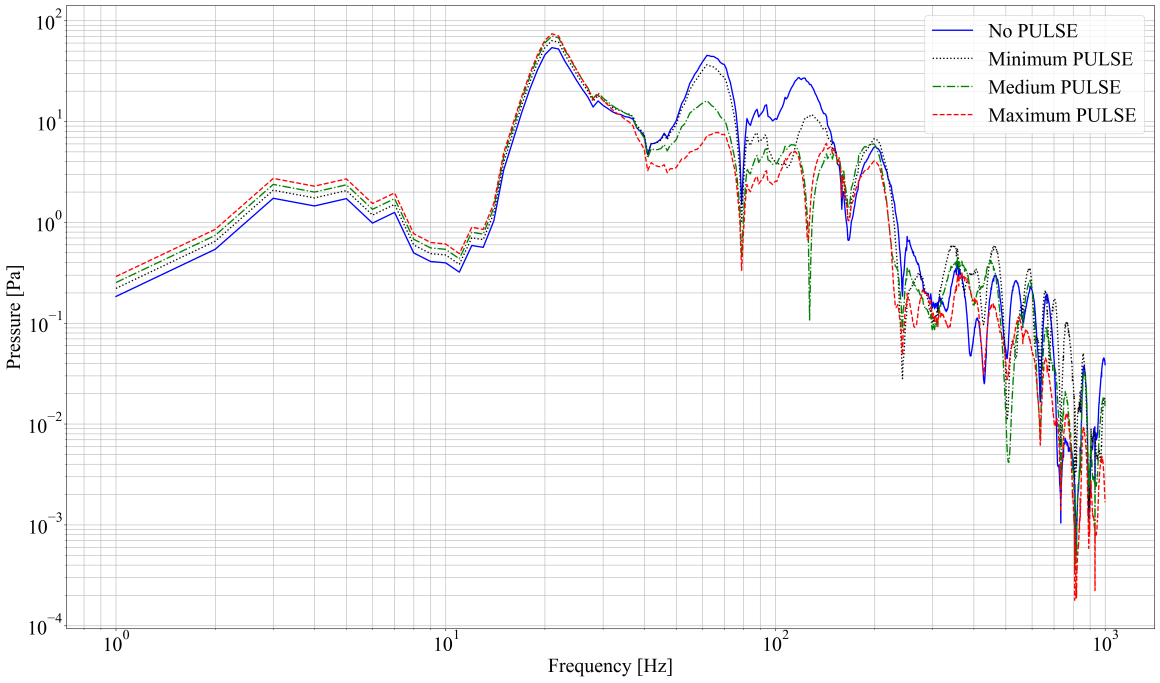

(a)

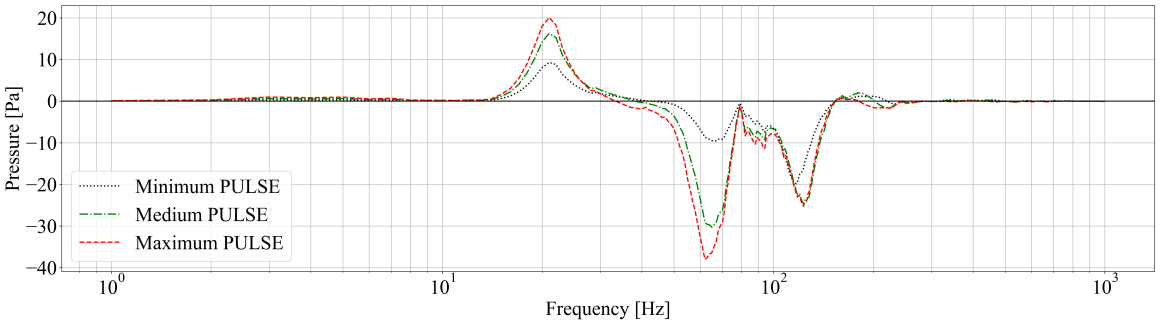

(b)

Figure 5.34: (a) Frequency spectra for different PULSE settings without additional mitigation measures at a distance of 750 meters from the monopile, with the receiver positioned 2 meters above the seabed. (b) Differences in the frequency spectra for each PULSE setting compared to the baseline scenario *no PULSE*.

5.5.2. PULSE combined with a BBC

Evolution of the radiated impulse in time

Fig. 5.35 illustrates the arrival times of the impulse for all PULSE settings. The goal is to understand how the introduction of a BBC impacts the characteristics of the impulse, particularly in terms of arrival time and amplitude attenuation. The results are consistent with those in Fig. 5.17 for PULSE without additional mitigation measures. Specifically, the elongation of the impulse and the introduction of a BBC do not alter the arrival time, which remains consistently constant. However, the BBC causes a reduction in amplitude across all impulses compared to the case without additional mitigation measures.

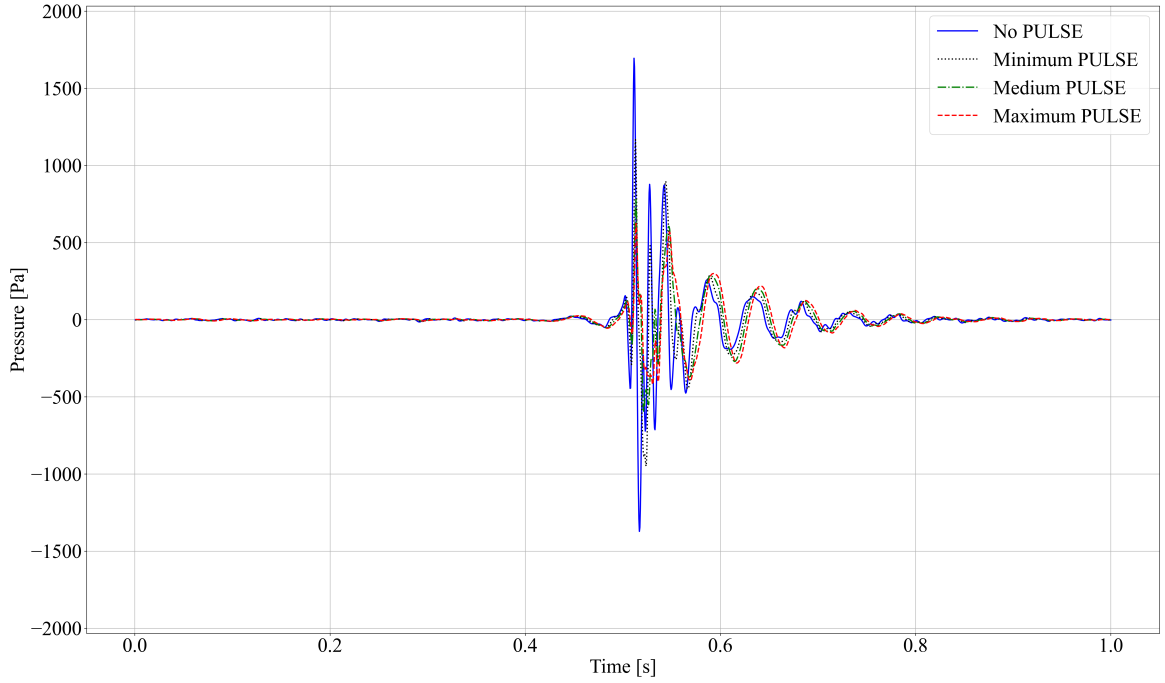

Figure 5.35: Time evolution of the modelled pressure impulse for different PULSE settings combined with a BBC. The impulse is expected to reach 750 meters after approximately 0.5 seconds.

Sound levels of different impulses

This section assesses the effect of different PULSE settings combined with a BBC on sound levels. The analysis follows the same structure as in Section 5.5.1, beginning with the quantification of noise reduction for each PULSE setting relative to the baseline scenario, followed by an investigation of the underlying causes by examining the system's frequency response.

Figs. 5.36 and 5.37 display the SEL and L_{peak} values at various horizontal distances from the monopile, respectively. The general trend observed in both sound levels mirrors the pattern seen for PULSE without additional mitigation measures, as shown in Figs. 5.31 and 5.32. Specifically, elongating the impulse results in a decrease in both SEL and L_{peak} values across all distances. As described in Section 5.5.1, the soil stratification is kept consistent to ensure a fair comparison across different scenarios. Consequently, there is a noticeable increase in sound levels observed at a distance of approximately 300-350 meters. This increase is attributed to the complex interaction of acoustic modes.

Table 5.7 summarises the SEL and L_{peak} values for all PULSE settings, along with their respective reductions relative to the baseline scenario. The SEL and L_{peak} data demonstrate that combining PULSE with a BBC results in greater relative reductions, particularly when comparing the *maximum PULSE* setting to the baseline scenario. Specifically, there is a 3.8 dB reduction in SEL with the addition of the BBC, compared to a 3.4 dB reduction in SEL for PULSE without additional mitigation measures.

However, these numbers can be misleading since they are logarithmic representations of sound levels. To accurately assess the effectiveness of PULSE combined with a BBC, reductions in the actual pressure values must also be considered. The pressure reductions are significantly lower when a BBC is added compared to when no BBC is used. For instance, with the *maximum PULSE* setting combined with a BBC, a reduction of 56 Pa is achieved relative to the baseline scenario, whereas without a BBC, a reduction of 119 Pa is obtained. This indicates that the efficiency of PULSE decreases when a BBC is introduced.

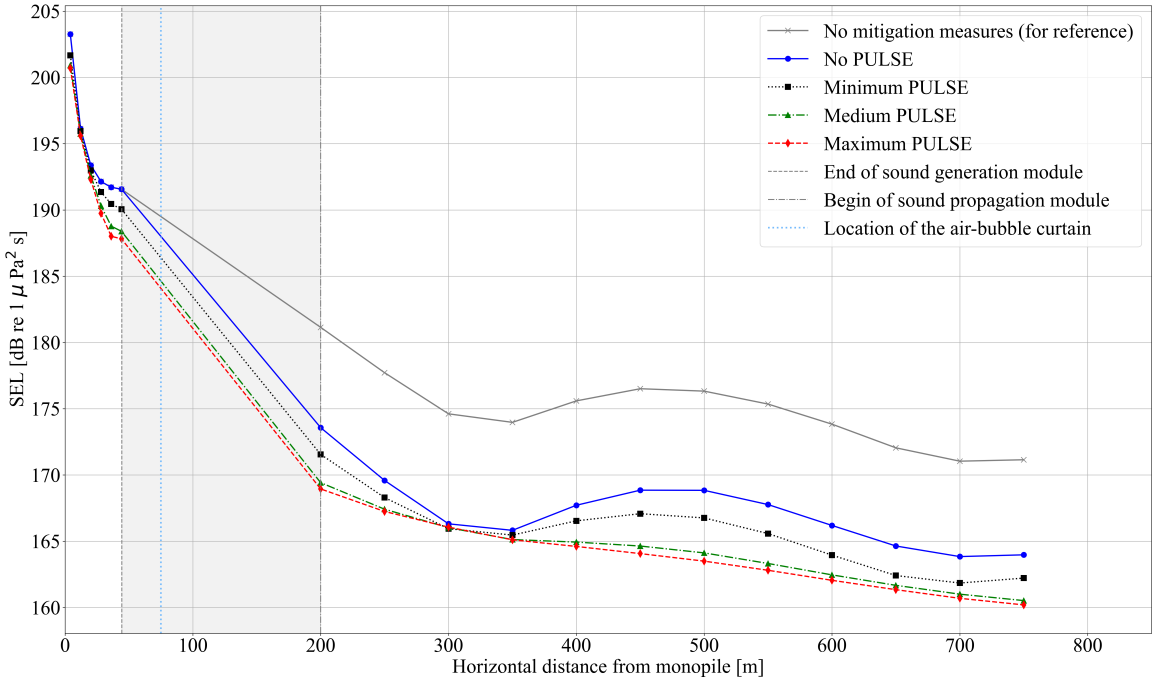

Figure 5.36: Comparison of modelled SEL values for different PULSE settings combined with a BBC at various horizontal distances from the monopile.

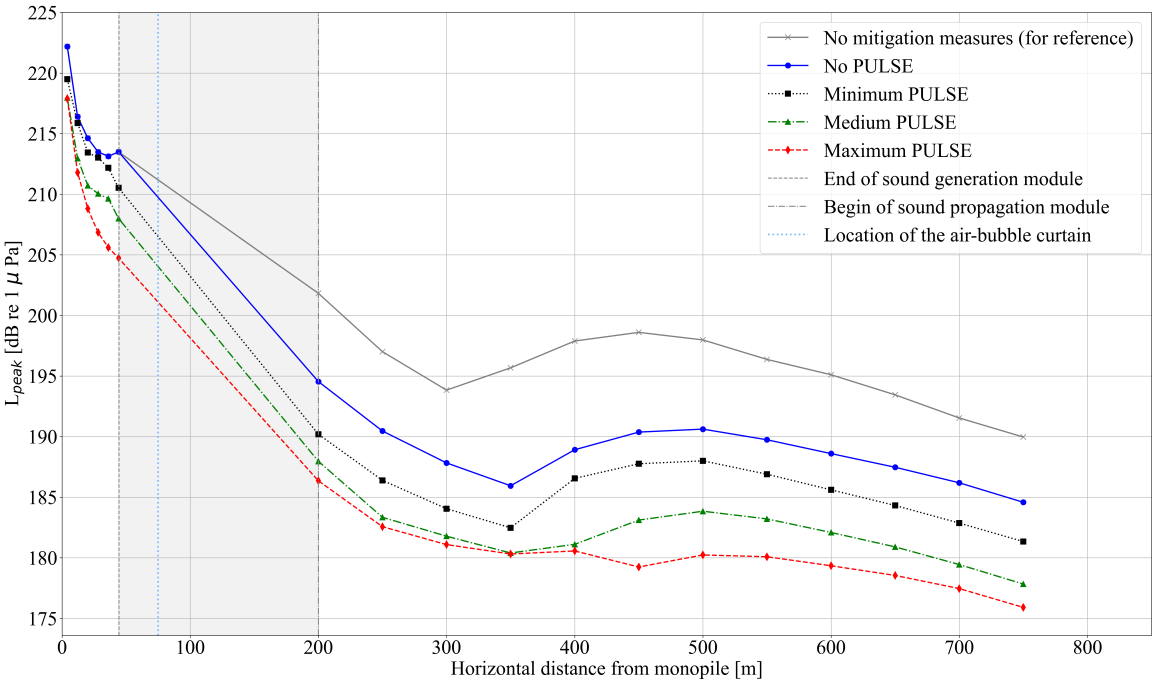

Figure 5.37: Comparison of modelled L_{peak} values for different PULSE settings combined with a BBC at various horizontal distances from the monopile.

Table 5.7: Sound levels and reductions relative to the baseline scenario *no PULSE* at 750 meters from the monopile, 2 meters above the seabed, for different PULSE settings combined with a BBC.

	SEL [dB re 1 μPa^2]	**SEL reduction** [dB re 1 μPa^2]	$\mathbf{L_{peak}}$ [dB re 1 μPa]	$\mathbf{L_{peak}}$ **reduction** [dB re 1 μPa]	p_{rms} **reduction** [Pa]
No PULSE	164.0	-	184.6	-	-
Min. PULSE	162.2	-1.8	181.3	-3.3	-29
Med. PULSE	160.5	-3.5	177.8	-6.8	-52
Max. PULSE	160.2	-3.8	175.9	-8.7	-56

These differences between PULSE settings can be explained by examining the frequency spectra of the different PULSE settings. This analysis is conducted similarly to Section 5.5.1, beginning with the transfer function of the system. The transfer function, which includes the BBC, is shown in Fig. 5.38. This transfer function reveals the antiresonant frequencies of the complete system. With this in mind, the frequency spectra of the forced system are analysed and presented in Fig. 5.39a. The blue solid line represents the baseline scenario *no PULSE*, the black dotted line shows the *minimum PULSE* setting, the green dash-dotted line illustrates the *medium PULSE* setting, and the red dashed line indicates the *maximum PULSE* setting. Additionally, Fig. 5.39b highlights the differences between each PULSE setting and the baseline scenario.

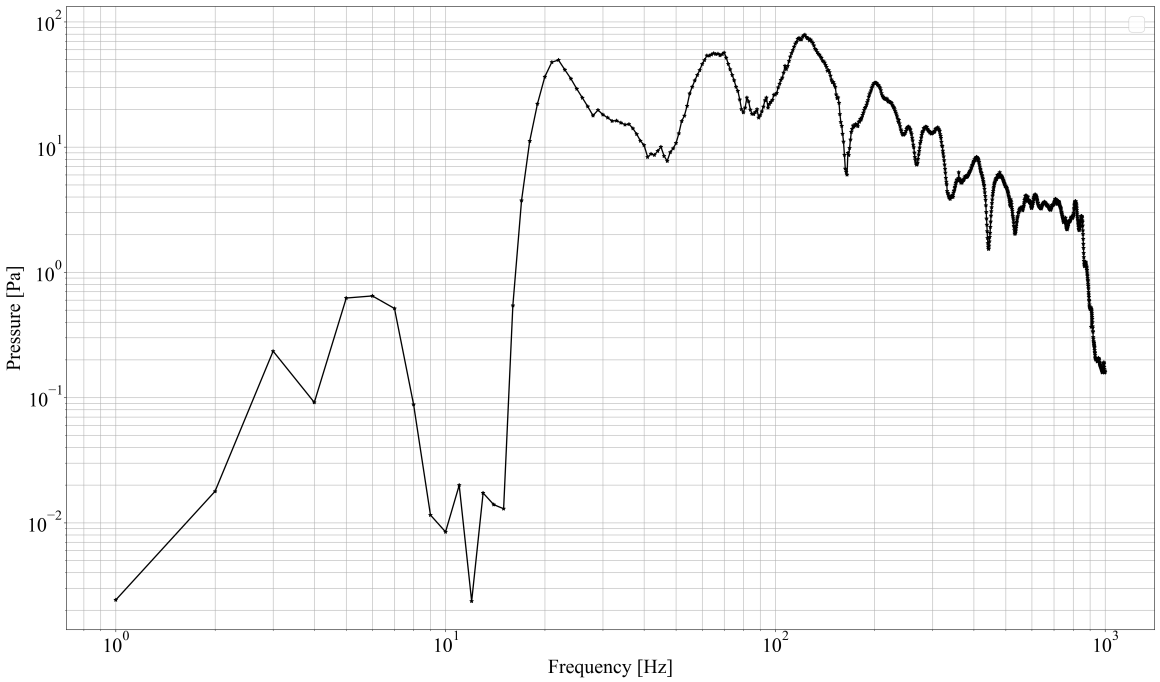

Figure 5.38: Frequency spectrum of the system's response to a unit load, illustrating the transfer function for PULSE combined with a BBC, measured 750 meters from the monopile and 2 meters above the seabed.

The observed pattern is similar to PULSE without additional mitigation measures, with energy shifting from high frequencies (above 32 Hz) to low frequencies (below 32 Hz) due to impulse elongation. The energy redistributions for different PULSE settings relative to the baseline scenario are summarised in Table 5.8. When adding a BBC, approximately the same amount of energy is reduced at high frequencies relative to the baseline, but less energy is added at low frequencies. Note that changes in lower frequency bands are less impactful than those in higher frequencies due to amplitude differences, as shown in Fig. 5.39a. Moreover, overall pressure levels are lower with a BBC because it also mitigates noise. Consequently, the absolute amount of redistributed energy is reduced, not reflected in the percentages in Table 5.8, as these are relative to the baseline scenario.

Table 5.8: Energy redistributions in low and high frequencies for different PULSE settings combined with a BBC relative to the baseline scenario *no PULSE*.

PULSE setting	**Low frequencies [%]**	**High frequencies [%]**
Minimum PULSE	+34	-52
Medium PULSE	+62	-87
Maximum PULSE	+71	-94

Furthermore, adding a BBC and elongating the impulse appears to shift the first antiresonant frequency from approximately 180 Hz to 140 Hz. This shift can be attributed to the interaction between the sound waves and the BBC. The introduction of a BBC increases damping in the system, which not only reduces the amplitude of oscillations but also affects the antiresonant frequencies. Additionally, elongating the impulse alters the time-domain characteristics of the input signal, impacting how sound waves propagate through the system and interact with the BBC. This change in propagation dynamics can lead to a shift in the frequencies where destructive interference, or antiresonance, occurs.

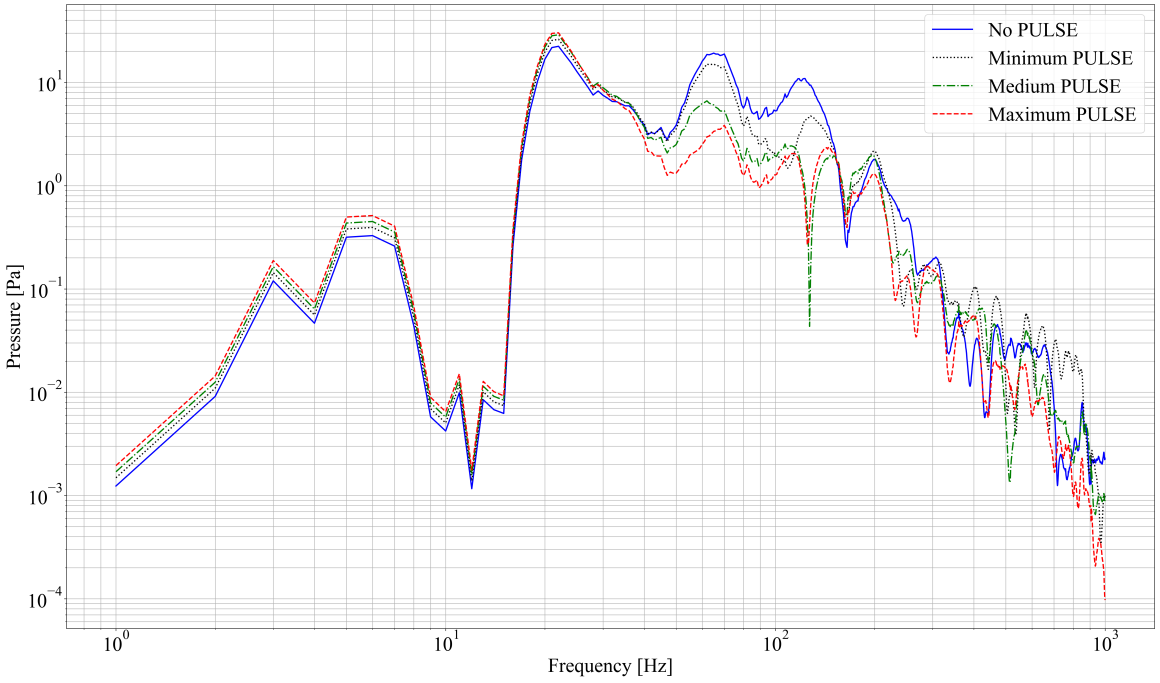

(a)

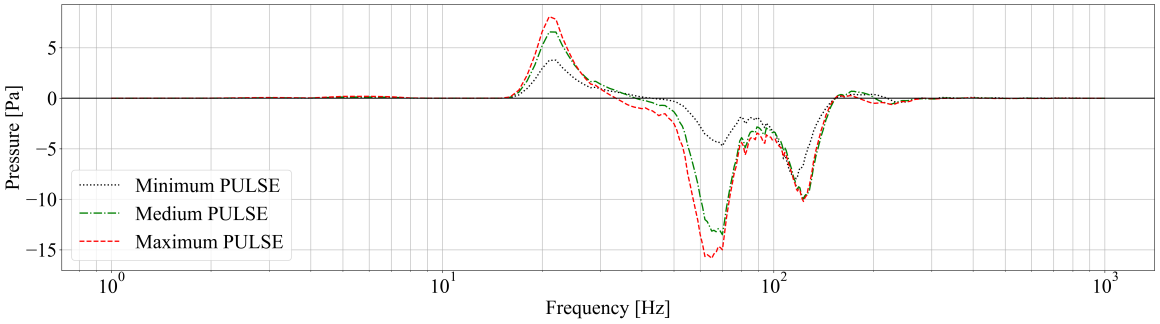

(b)

Figure 5.39: (a) Frequency spectra for different PULSE settings combined with a BBC at a distance of 750 meters from the monopile, with the receiver positioned 2 meters above the seabed. (b) Differences in the frequency spectra for each PULSE setting compared to the baseline scenario *no PULSE*.

5.5.3. PULSE combined with a DBBC

Evolution of the radiated impulse in time

Combining PULSE with a DBBC does not alter the arrival time of different impulse elongations at 750 meters from the monopile, as illustrated in Fig. 5.40. All impulses reach the receiver in approximately 0.5 seconds. The main difference between the various impulse elongations is their amplitude. Notably, the results are similar to the case with a BBC, but amplitudes are lower.

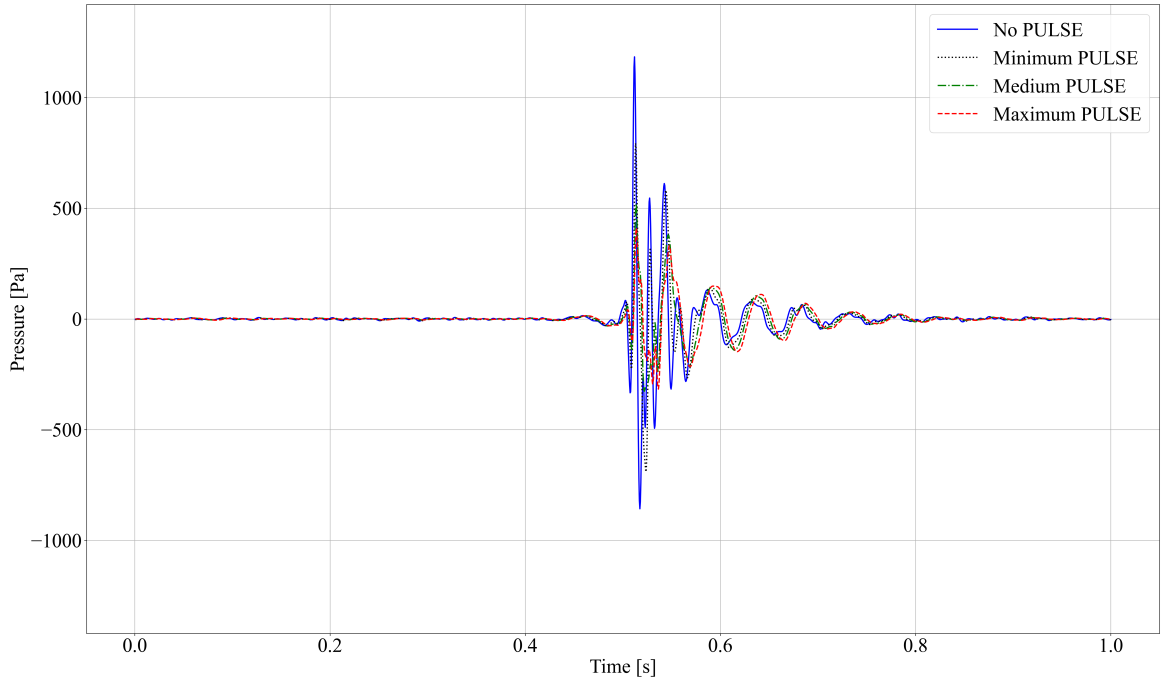

Figure 5.40: Time evolution of the modelled pressure impulse for different PULSE settings combined with a DBBC. The impulse is expected to reach 750 meters after approximately 0.5 seconds.

Sound levels of different impulses

The effect of combining different impulse elongations with a DBBC is assessed both quantitatively and qualitatively. Figs. 5.41 and 5.42 show the SEL and L_{peak} values across various distances from the monopile. As depicted in the figures, sound levels generally decrease as the distance from the monopile increases, with an observed increase after approximately 300-350 meters. These observations align with the findings discussed in Section 5.5.1.

Table 5.9 provides an overview of the modelled SEL and L_{peak} values for the different PULSE settings. Additionally, it presents the quantitative reductions in sound levels and pressure values compared to the baseline scenario. The data clearly show that elongating the impulse, combined with a DBBC, yields significant reductions. These reductions surpass those observed for PULSE without air-bubble curtains and PULSE with a BBC when considering the SEL and L_{peak} values alone. However, to correctly assess the effectiveness of PULSE when combined with a DBBC, the pressure levels must also be considered, as the SEL and L_{peak} values are logarithmically scaled. When examining the pressure reductions, it is evident that these are significantly lower when a DBBC is added compared to when no DBBC is used. For instance, with the *maximum PULSE* setting combined with a DBBC, a reduction of 45 Pa is achieved, relative to the baseline scenario, whereas without a DBBC, a reduction of 119 Pa is obtained. This indicates that the efficiency of PULSE decreases when a DBBC is introduced.

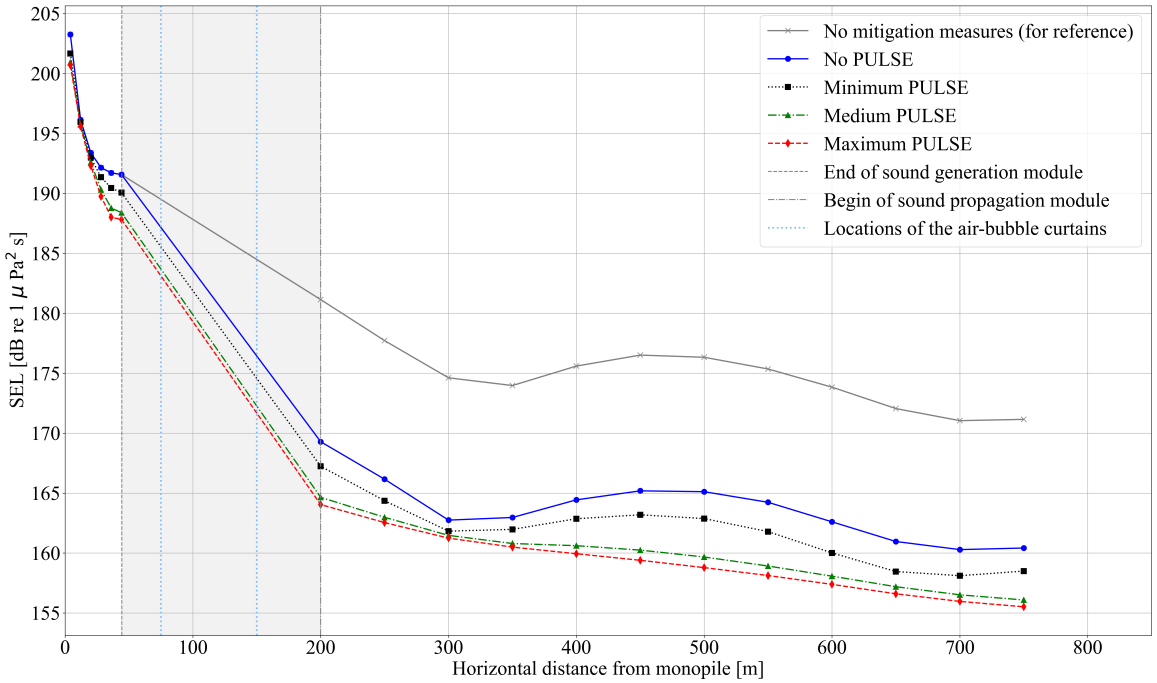

Figure 5.41: Comparison of modelled SEL values for different PULSE settings combined with a DBBC at various horizontal distances from the monopile.

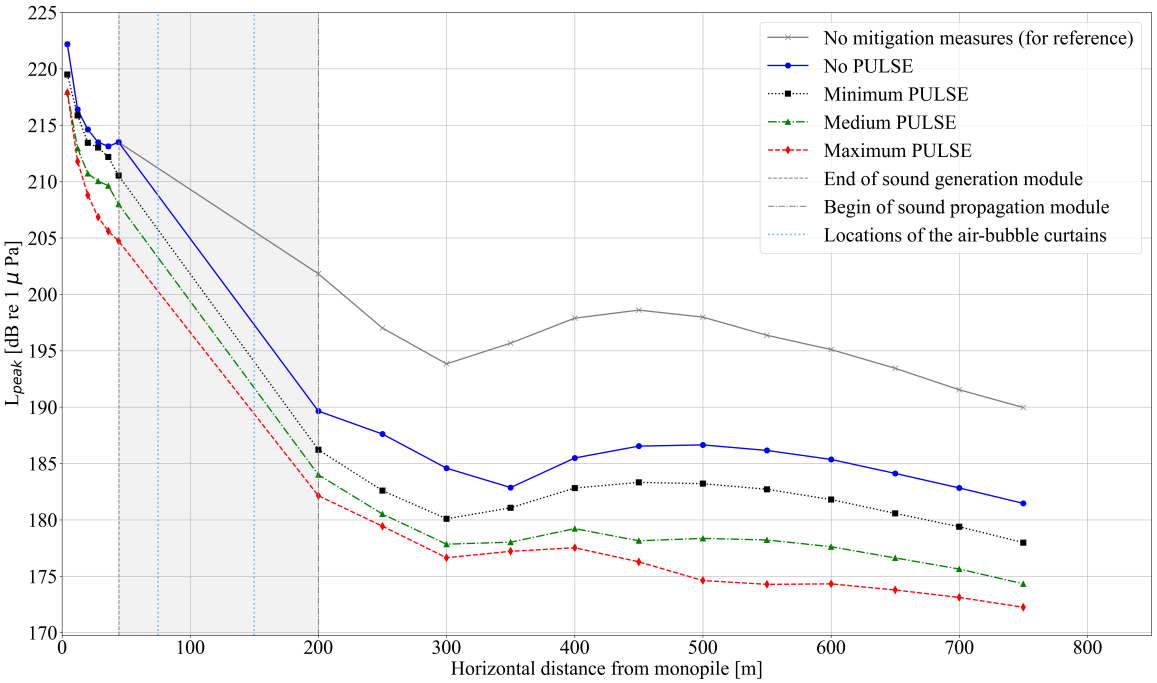

Figure 5.42: Comparison of modelled L_{peak} values for different PULSE settings combined with a DBBC at various horizontal distances from the monopile.

Table 5.9: Sound levels and reductions relative to the baseline scenario no PULSE at 750 meters from the monopile, 2 meters above the seabed, for different PULSE settings combined with a DBBC.

	SEL [dB re 1 μPa^2]	**SEL reduction** [dB re 1 μPa^2]	$\mathbf{L_{peak}}$ [dB re 1 μPa]	$\mathbf{L_{peak}}$ **reduction** [dB re 1 μPa]	p_{rms} **reduction** [Pa]
No PULSE	160.4	-	181.5	-	-
Min. PULSE	158.5	-1.9	178.0	-3.5	-21
Med. PULSE	156.1	-4.3	174.3	-7.2	-41
Max. PULSE	155.5	-4.9	172.3	-9.2	-45

The frequency spectra of the different impulse elongations are evaluated next. First, the transfer function of the pile-water-soil system, including a DBBC, is presented in Fig. 5.43. This transfer function reveals the system's antiresonant frequencies, identified by the dips in the spectrum. With these antiresonant frequencies known, the frequency spectra of the forced systems are analysed, as shown in Fig. 5.44a. The blue solid line represents the baseline scenario *no PULSE*, the black dotted line shows the *minimum PULSE* setting, the green dash-dotted line illustrates the *medium PULSE* setting, and the red dashed line indicates the *maximum PULSE* setting. Additionally, Fig. 5.44b highlights the differences between each PULSE setting and the baseline scenario.

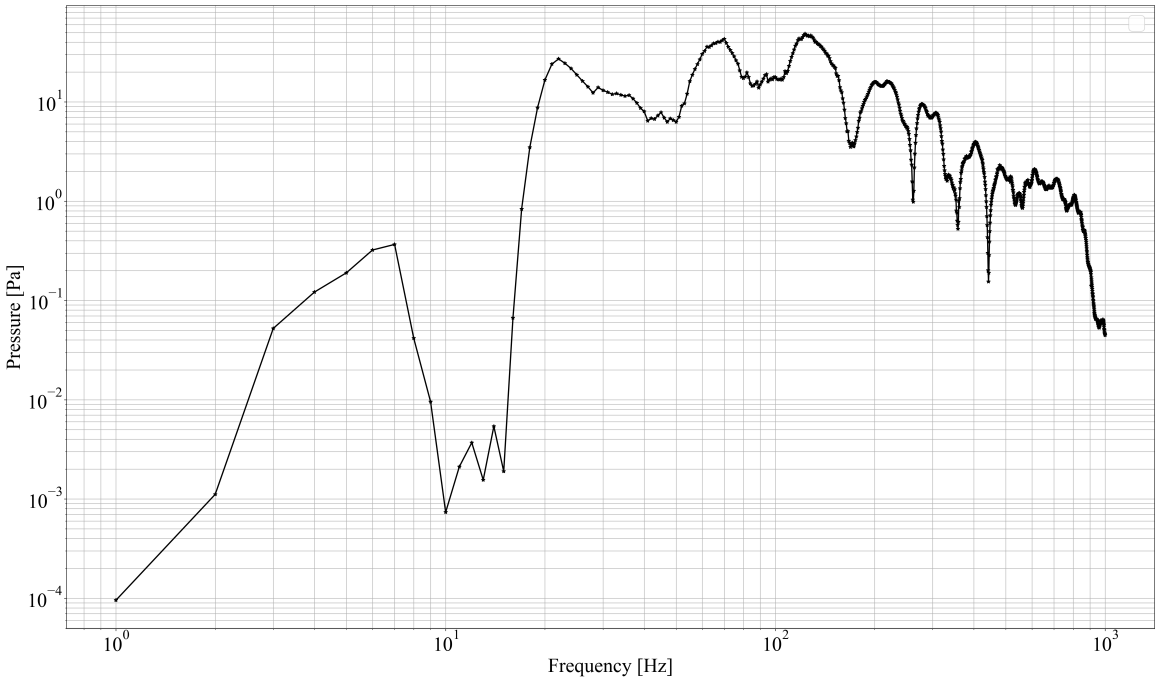

Figure 5.43: Frequency spectrum of the system's response to a unit load, illustrating the transfer function for PULSE combined with a DBBC, measured 750 meters from the monopile and 2 meters above the seabed.

The observed patterns in the differences are consistent with previously analysed cases. The energy redistributions from high frequencies (above 32 Hz) to low frequencies (below 32 Hz) due to the impulse elongations are presented in Table 5.10. These values indicate that incorporating a DBBC into the system results in a relatively similar reduction of high-frequency energy compared to previous cases, but with a smaller increase in low-frequency energy. It is important to note that this energy redistribution is relative to the baseline scenario. Changes in lower frequency bands are less impactful than those in higher frequencies due to amplitude differences, as illustrated in Fig. 5.44a. Additionally, the overall pressure levels are lower when a DBBC is applied because the DBBC mitigates noise. Consequently, the absolute amount of energy redistributed is reduced, which cannot be seen in the percentages shown in Table 5.10, as these are relative to the baseline scenario.

Table 5.10: Energy redistributions in low and high frequencies for different PULSE settings combined with a DBBC relative to the baseline scenario *no PULSE*.

PULSE setting	**Low frequencies [%]**	**High frequencies [%]**
Minimum PULSE	+33	-50
Medium PULSE	+58	-88
Maximum PULSE	+64	-94

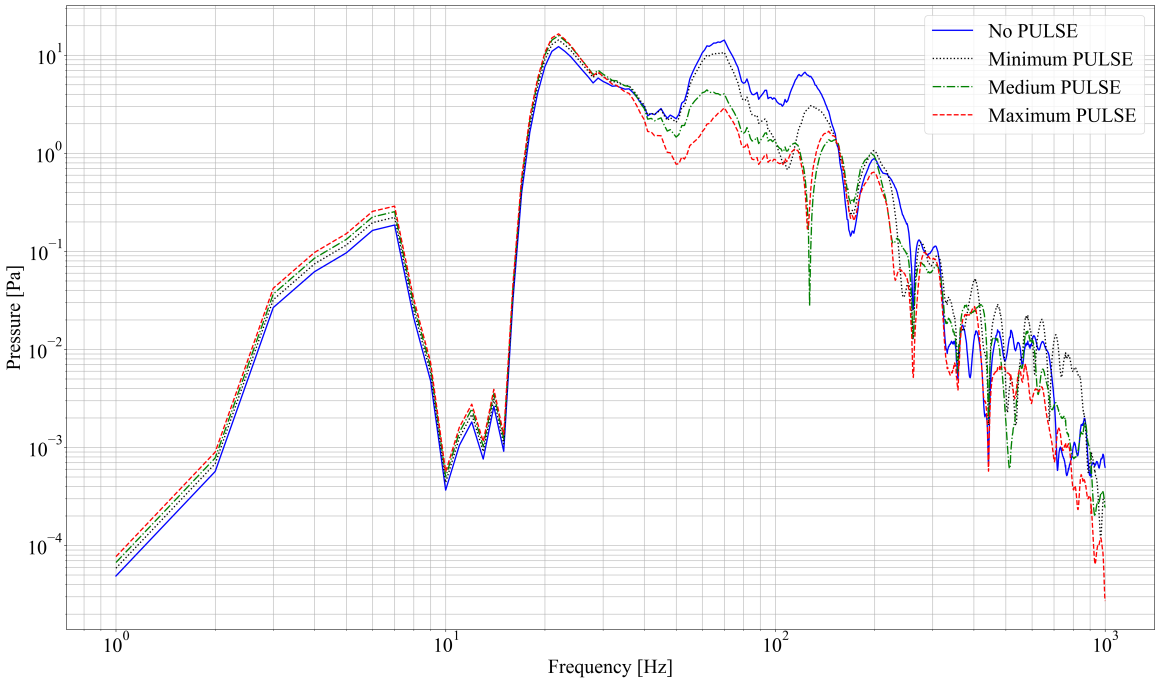

(a)

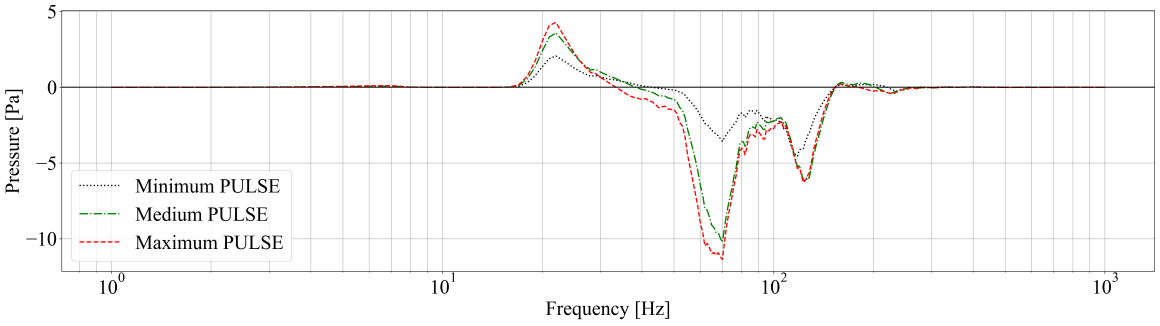

(b)

Figure 5.44: (a) Frequency spectra for different PULSE settings combined with a DBBC at a distance of 750 meters from the monopile, with the receiver positioned 2 meters above the seabed. (b) Differences in the frequency spectra for each PULSE setting compared to the baseline scenario *no PULSE*.

In conclusion, when combining PULSE with air-bubble curtain configurations, especially with a DBBC, a reduced noise reduction for PULSE is obtained when comparing the *maximum PULSE* setting to the baseline scenario.

5.6. Insertion losses

Fig. 5.45 presents the spectral differences of the modelled pressures across the frequency range, summarising the scenarios discussed in the previous section. These differences represent the impact of the various noise mitigation measures compared to the situation where no mitigation measures are applied. The following observations can be made by examining Fig. 5.45.

PULSE:

- **Low frequencies:** Introducing PULSE increases noise levels in the low-frequency range.
- **High frequencies:** Conversely, PULSE tends to reduce noise levels at higher frequencies, showing a positive effect in this range.

Air-bubble curtains:

- **Low frequencies:** The effectiveness of (D)BBC at lower frequencies is generally limited due to the longer wavelengths of low-frequency sound waves, as confirmed by Bellmann et al. [5]. If there is a positive effect at low frequencies, it should be negligible compared to the effectiveness at mid and high frequencies. However, this study found unexpected positive effects at low frequencies, which will be discussed later in this section.
- **High frequencies:** The (D)BBC is more effective at higher frequencies due to the smaller wavelengths of high-frequency sound waves being more easily scattered and absorbed by the air bubbles.

PULSE + air-bubble curtains:

- **Low frequencies:** Despite the initial increase in low-frequency noise caused by PULSE, the combination of PULSE with (D)BBC shows a reduction in low-frequency noise compared to the no mitigation scenario, resulting in a positive insertion loss at these frequencies. However, this result is unexpected, as (D)BBC typically shows limited performance at low frequencies. This behaviour will be discussed later in this section.
- **High frequencies:** At high frequencies, the combination of PULSE with (D)BBC results in a greater reduction in noise levels compared to (D)BBC alone. This is because PULSE reduces high-frequency noise, and the (D)BBC further attenuates these frequencies leading to an overall enhanced noise reduction effect in the high-frequency range.

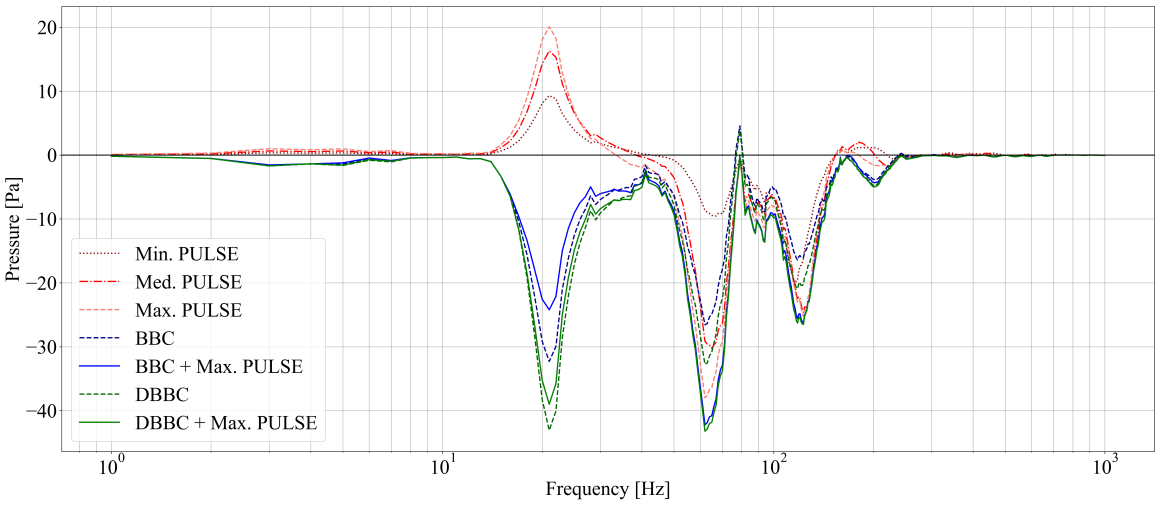

Figure 5.45: Overview of the spectral insertion loss for various scenarios, including different PULSE settings (*minimum*, *medium*, *maximum*), BBC and DBBC, and their combination.

As discussed above, Fig. 5.45 reveals that the modelled air-bubble curtains show very good performance at low frequencies. This very good performance contradicts common sense and previous research [5,

60] on the effectiveness of air-bubble curtains. This discrepancy likely arises from the air-bubble curtain model's assumption of one-dimensional (z-dependent) transmission loss. While this assumption is reasonable for high frequencies, it becomes less accurate at low frequencies. Consequently, the model overestimates the air-bubble curtain's performance at low frequencies, suggesting it absorbs more sound than it actually does in practice.

This issue can be addressed by applying a filter to the frequencies below 32 Hz. Initially, this can be achieved by using the unmitigated frequency response for frequencies up to 32 Hz and the mitigated response for frequencies above 32 Hz. This approach is essentially equivalent to assuming zero efficiency of the (D)BBC below 32 Hz.

To further refine this method, a smooth transition between the unmitigated and mitigated responses is implemented around the 32 Hz mark. Instead of an abrupt switch, a blending technique is employed using a hyperbolic tangent (`tanh`) function. This function creates a smooth transition over a specified range, blending the unmitigated and mitigated responses seamlessly. Specifically, the blending function is defined as:

$$\text{Blending function}(f) = 0.5 \left(1 + \tanh\left(\frac{f - 32\ \text{Hz}}{w}\right)\right)$$

where f is the frequency and w is the transition width. This blending function gradually changes from 0 to 1 around 32 Hz, with a smoother slope controlled by w. The reverse blending function is simply $1 - \text{Blending function}(f)$. These two functions are shown in Fig. 5.46.

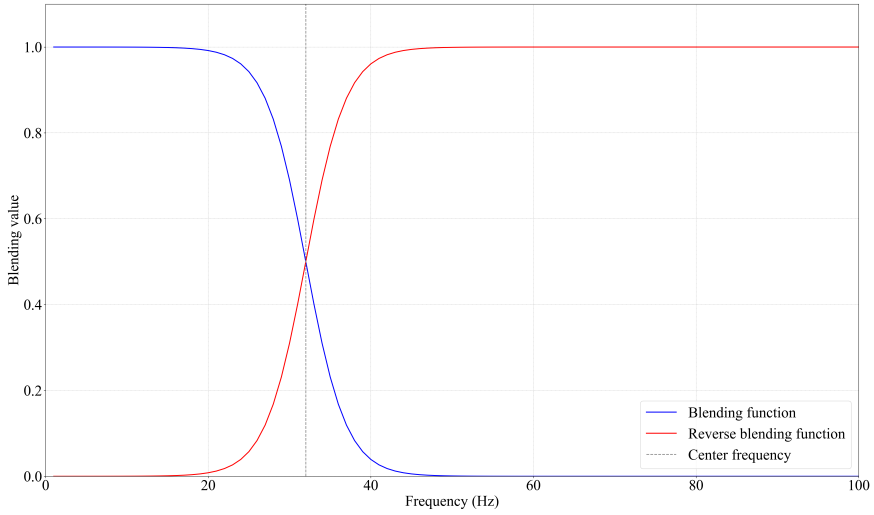

Figure 5.46: Blending function and reverse blending function around 32 Hz. The higher frequencies are not shown as they maintain a constant value of 0 for the blending function and 1 for the reverse blending function beyond this range.

Using these functions, the frequency response at each frequency f is calculated as:

$$\begin{aligned}\text{Merged response}(f) = {} & \text{Blending function}(f) \times \text{Unmitigated response}(f) \\ & + \text{Reverse blending function}(f) \times \text{Mitigated response}(f)\end{aligned}$$

This approach ensures a gradual and smooth transition between the unmitigated and mitigated responses around 32 Hz, thereby avoiding any abrupt changes that could introduce artefacts or inaccuracies in the frequency response data. This merged response, which represents the expected response of air-bubble curtains, is added to the graph with insertion losses, shown in Fig. 5.47. Here, it can be seen that the unmitigated response is used for the low frequencies, a gradual transition is applied around 32 Hz, and the mitigated response is used for higher frequencies. Additionally, the approach with the abrupt switch at 32 Hz is included for comparison.

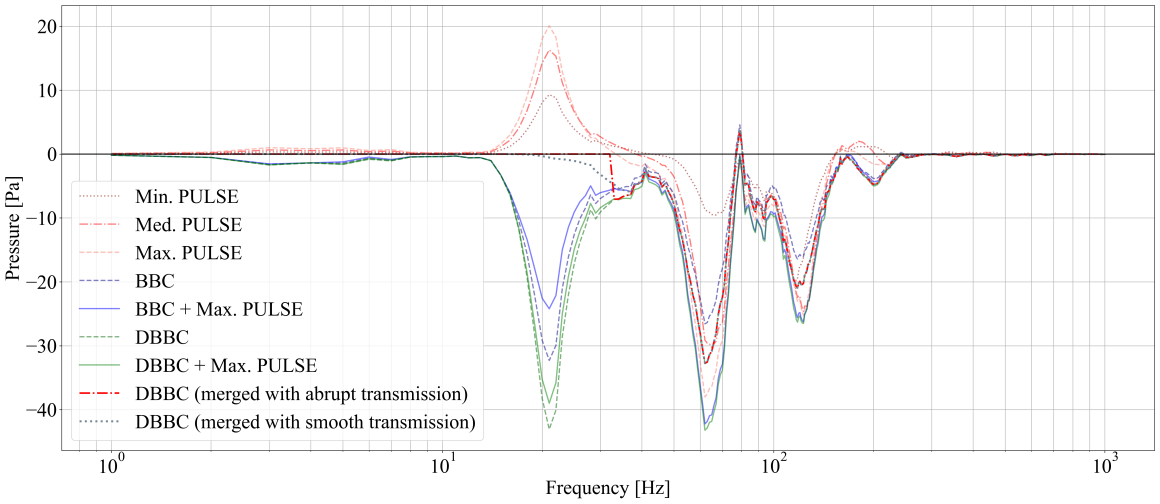

Figure 5.47: Overview of the spectral insertion loss for various scenarios, including the merged response of the system with a DBBC for an abrupt and smooth transition.

However, when calculating the noise levels using this modified response, the model does not perform well and significantly overestimates the measurements. This discrepancy is evident in Fig. 5.48. Therefore, the issue of the very good performance of air-bubble curtains at low frequencies cannot be resolved using this method (applying the unmitigated response for low frequencies). Consequently, the air-bubble curtain model should be reviewed to investigate the very good performance of the (D)BBC at low frequencies.

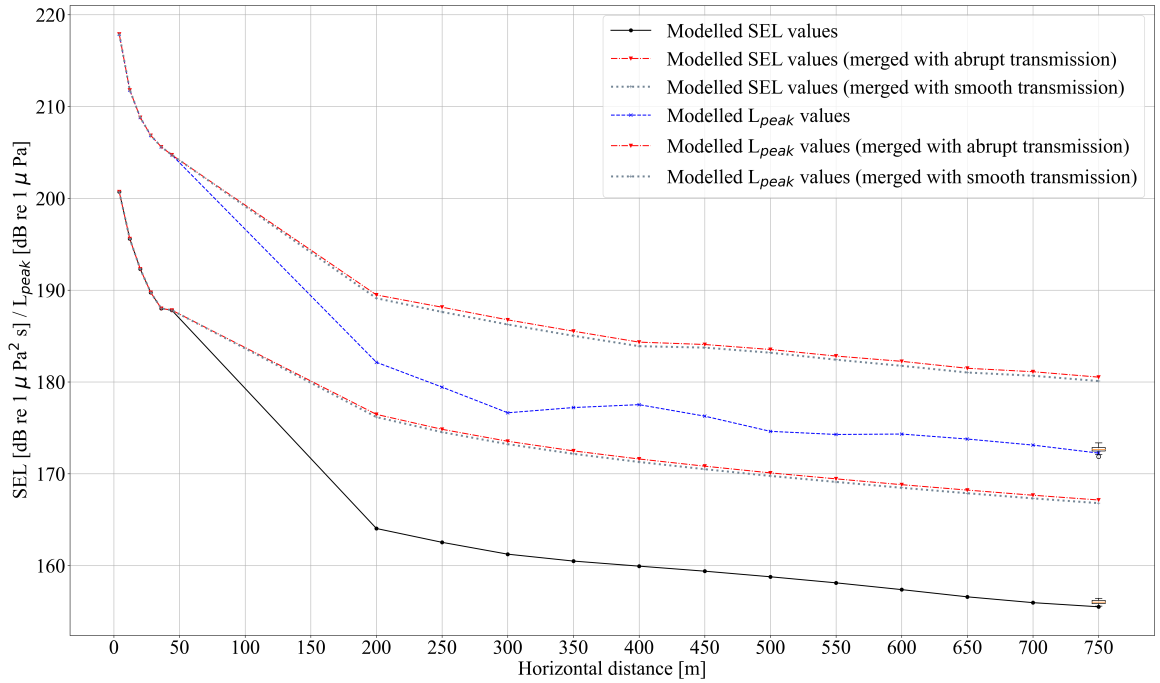

Figure 5.48: Comparison of modelled SEL and L_{peak} values with measurements for PULSE combined with a DBBC, including the noise levels of the merged responses.

6

Discussion, conclusions and recommendations

6.1. Discussion and conclusions

The primary aim of this study was to investigate the influence of PULSE on underwater radiated noise and its interaction with air-bubble curtains. As the world strives to limit the rise in global temperatures to well below 2 degrees Celsius, in line with the Paris Agreement [66], offshore wind farms (OWFs) play a crucial role in achieving this target. However, the construction of OWFs generates considerable noise, necessitating innovative noise mitigation techniques such as PULSE.

The study's main objective was achieved by modelling the complete coupled pile-water-soil system using the semi-analytical SILENCE model. PULSE was incorporated by multiplying the system's frequency response due to a unity load with the exact time force depending on the PULSE setting, while air-bubble curtains were integrated into SILENCE via a dedicated module. In general, the study found that PULSE significantly reduces sound levels, although its efficiency diminishes when used in combination with air-bubble curtain configurations. This chapter discusses and concludes the key findings, offering insights into the mechanisms underlying noise reduction by PULSE. Additionally, the study's limitations are addressed, discussing the quality and reliability of the results. Finally, recommendations are made for future research and the integration of additional noise mitigation measures.

6.1.1. Comparison of model results with field data

Since the primary objectives of this study focus on assessing the effects of different PULSE settings on pile dynamics and radiated underwater noise, comparing the SILENCE model against field data was essential to ensure its reliability for subsequent analyses. The comparison included two cases: (i) PULSE without additional mitigation measures, and (ii) PULSE combined with a Double Big Bubble Curtain (DBBC).

The model demonstrated good agreement with the field data for both Sound Exposure Level (SEL) and Sound Peak Level (L_{peak}). For the first case, the model overestimated the SEL by 0.6 dB and underestimated the L_{peak} by 0.5 dB. Similarly, the model's predictions for the second case were within 0.5 dB of the measured SEL and 0.4 dB of the measured L_{peak}. These predictions fall within the uncertainty range of the results, which stems from inherent uncertainties in the parameter values, primarily soil parameters, and measurements [49]. The model's spectral analysis aligned well with the field data across most frequency ranges, although there were some discrepancies. The model tended to overestimate energy at lower frequencies (below 32 Hz) and underestimate it at higher frequencies (beyond 200 Hz). These differences could be attributed to limitations in the model's resolution – which are discussed later in this section – or the propagation environment not being fully captured. These findings hold for both cases.

The comparison confirms previous studies [47, 48, 49, 64] that the SILENCE model provides a reliable foundation for analysing the effects of different PULSE settings on pile dynamics and radiated underwater noise. The discrepancies observed are within acceptable limits and do not significantly impact the model's overall predictive accuracy.

6.1.2. Dynamics and energy flux of the monopile

The analysis of the dynamics and energy flux of the monopile revealed that elongating the impulse with different PULSE settings affects the energy transfer and vibration behaviour of the pile. Specifically, the study found that without PULSE, the energy flux exhibited the highest amplitude peak and the shortest duration, resulting in more intense and transient energy delivery. This scenario suggests that the pile experiences a high-impact force over a short period, leading to greater instantaneous stress and an increased risk of damage. Conversely, PULSE settings with elongated impulses reduce peak amplitudes but extend the duration, resulting in a more sustained energy transfer.

In terms of pile vibrations, elongating the impulse led to higher and longer vibrations in both radial and vertical directions. These findings underscore the importance of considering both amplitude and duration when analysing pile dynamics under different PULSE settings.

6.1.3. Underwater noise radiation due to PULSE

The effect of impulse elongation on radiated underwater noise revealed significant changes in energy distribution and sound levels, which have important implications for marine ecosystems. The analysis of energy introduced into the exterior domain showed how varying PULSE settings affect the different types of waves generated and their subsequent impact on underwater noise levels. Longer impulses reduced the peak energy of pressure waves, helping mitigate the amount of underwater noise radiated directly into the water. In contrast, Scholte waves, which are lower in frequency, showed a slight increase in energy with longer impulses, indicating that elongated impulses are more effective in transferring energy into Scholte waves. These waves primarily affect marine life close to the seabed, such as sponges and shellfish, compared to higher-frequency pressure waves. An advantage of longer impulses is that they favour the transmission of energy into the soil rather than the water, leading to a noticeable redistribution of energy with increasing impulse duration. This means that soil becomes more important when elongating the impulse, meaning that the efficiency of mitigation measures in the water will decrease when the impulse is elongated but the overall sound level will be lower. This redistribution of energy from water to soil highlights the benefits of longer impulse durations in mitigating underwater noise.

The analysis of sound levels under different PULSE settings demonstrated that elongating the impulse duration effectively reduces both SEL and L_{peak} at various distances from the monopile. For instance, at 750 meters from the monopile, using the *maximum PULSE* setting resulted in a reduction of 3.4 dB for SEL and 6.8 dB for L_{peak} compared to the baseline scenario *no PULSE*. This nearly aligns with the manufacturer's claims [25], who initially reported an advantage of 6-10 dB for SEL, but later guaranteed a 4-6 dB reduction for SEL values for new projects [13]. Although there is no scientific research specifically on PULSE's reduction, these findings support the manufacturer's guarantees and suggest that elongating the impulse duration significantly reduces underwater noise levels.

Investigating the origins of these differences involved analysing the frequency spectra for the various PULSE settings, revealing significant redistributions in energy distribution across frequency bands. Detailed frequency spectra analysis showed that elongating the impulse resulted in a decrease in energy levels for almost all frequencies higher than 32 Hz, depending on the PULSE setting. Conversely, for frequencies lower than 32 Hz, the energy is higher in the elongated impulses compared to the baseline scenario.

6.1.4. Underwater noise radiation due to PULSE combined with air-bubble curtains

The quantitative analysis of combining different impulse elongations with air-bubble curtains demonstrated that this combination effectively reduces both SEL and L_{peak} values at various distances from the monopile. At 750 meters from the monopile, the combined use of PULSE with a BBC resulted in SEL reductions of up to 3.8 dB and L_{peak} reductions of up to 8.7 dB compared to the baseline scenario. Similarly, when combining different impulse elongations with a DBBC, the analysis showed SEL reductions of up to 4.9 dB and L_{peak} reductions of up to 9.2 dB compared to the baseline scenario. However, these reductions, being logarithmic representations of sound levels, can be misleading. To accurately assess the effectiveness of PULSE combined with air-bubble curtains, actual pressure value reductions must also be considered. The pressure reductions are significantly lower when a (D)BBC is added compared to when no (D)BBC is used, indicating that the efficiency of PULSE decreases when air-bubble curtains are introduced. Therefore, it is important to highlight that the individual performance of the two mitigation measures – PULSE and air-bubble curtains – cannot be linearly added to obtain the performance of the combined measures.

The frequency spectra of the different impulse elongations combined with air-bubble curtains were evaluated to understand the energy distribution across frequencies. Analyses showed that impulse elongations cause significant energy shifts from high frequencies (above 32 Hz) to low frequencies (below 32 Hz). These findings are consistent with the analysis of PULSE without additional mitigation measures, confirming that longer impulse durations increase low-frequency energy while reducing high-frequency energy. It must be emphasised that this energy redistribution is relative to the baseline scenario, meaning that the energy changes in the lower frequency bands are less influential than those in the higher frequencies due to amplitude differences. Moreover, the overall energy levels are lower when a (D)BBC is applied because the (D)BBC also mitigates noise. Consequently, the absolute amount of energy redistributed is reduced.

The analysis of insertion losses highlighted the impact of various noise mitigation measures on radiated underwater noise. The findings for PULSE alone were confirmed. Air-bubble curtains showed a positive effect on reducing low-frequency noise and are even more effective at higher frequencies. However, the surprisingly good performance at low frequencies contradicts both common sense and previous research [5, 60]. This discrepancy likely stems from the air-bubble curtain model's assumption of one-dimensional (z-dependent) transmission loss. While this assumption is reasonable for high frequencies, it becomes less accurate at low frequencies. Consequently, the model overestimated the air-bubble curtain's effectiveness at low frequencies, suggesting it absorbed more sound than it does in practice.

To address this issue, a filter was applied to frequencies below 32 Hz. Despite these adjustments, the model significantly overestimated the measurements and did not accurately predict the noise levels. Thus, the unexpected performance of air-bubble curtains at low frequencies cannot be resolved using this method.

6.1.5. Main research question

By addressing the two objectives, the main research question can be answered:

To what extent does PULSE influence radiated underwater noise and interact with other mitigation measures such as air-bubble curtains?

The study found that elongating the impulse duration significantly enhances noise reduction, both when used alone and in combination with air-bubble curtains. The *maximum PULSE* setting achieves substantial reductions in sound levels while adding air-bubble curtain configurations decreases its effectiveness. As marine infrastructure continues to develop, it is crucial to implement these findings to protect marine ecosystems. The challenge ahead is clear: how will future technologies balance industrial advancement with the preservation of our underwater environments? This pressing question calls for innovative solutions and a commitment to sustainable practices.

6.2. Limitations of the study

This study encountered several uncertainties and limitations throughout its duration. These uncertainties and limitations are important to consider when interpreting the results and are discussed in detail below.

SILENCE model limitations

- **Neglect of interactions:** The model neglects certain nonlinear interactions, including nonlinear soil-structure interaction, nonlinear fluid-structure interaction, and the interaction between the hammer and pile, as it only considers an input force at the top.
- **Boundary conditions approximation:** The boundary conditions at the edges of the monopile are simplified. This study uses a clamped-free boundary condition – where the pile tip is clamped into the ground, and the top is free. In reality, boundary conditions lie between clamped-free and free-free, leading to small variations in the results.
- **Rigid baffle and boundary:** The model includes a rigid baffle and boundary below the pile, preventing wave radiation into deeper soil layers. Research by Masoumi and Degrande [40] suggests the rigid boundary's influence is minor for deep pile penetration, but this remains a model limitation.
- **Simplified monopile geometry:** The model assumes a uniform diameter and thickness for the monopile, although real-world monopiles have canonical shapes. This simplification can lead to discrepancies between the model predictions and actual performance, but would not significantly change the results.
- **Exclusion of fluid and soil inside the pile:** The model does not account for fluid and soil within the pile, factors which would not significantly influence the pile's response to applied forces.
- **Layered soil model:** The model for this study represents the soil with only two layers, i.e. marine mud and a deeper soil layer. The deeper soil layer is an average of multiple real-world layers, a substantial assumption that simplifies the complex stratigraphy of the seabed. Including more soil layers would provide more accurate results but at the cost of increased computational complexity.
- **Constant layering in the radial direction:** The model assumes uniform water depth and consistent soil composition across the horizontal distance.

Environmental and operational constraints

- **Shallow water assumptions:** The study's results apply to shallow water conditions. Future monopile installations in deeper waters will face additional challenges, such as stronger currents and increased monopile diameter. This study did not consider these factors which could significantly impact the results.
- **Dynamic environmental factors:** The model does not fully account for dynamic environmental factors such as varying current speeds and temperature fluctuations, which can influence the predictability of noise levels. However, temperature changes are not expected to influence the results significantly.

Field data

- **Limited data availability:** The study is based on a limited part of the dataset since only three monopiles were installed without the use of additional noise mitigation measures besides PULSE and air-bubble curtains.
- **Uncertainty in soil parameters:** The input parameters used for the soil layers are derived from Cone Penetration Tests (CPTs) provided by geotechnical reports. These parameters are approximations of reality, and their accuracy is not guaranteed. Combined with the simplifications in the model, this introduces uncertainty in the modelled soil properties. To address this, a better approach would be to include this uncertainty as a statistical distribution, such as a Gaussian distribution. By modelling the soil parameters as distributions, uncertainty quantification techniques like Monte Carlo simulations can be performed. This will result in output distributions that provide a probabilistic assessment of the model's predictions, offering a more comprehensive understanding of the potential variability and reliability of the results.

- **Hydrophone accuracy**: The hydrophones used for measuring sound levels require precise calibration to ensure accurate data collection. These instruments can also pick up errors and noise from other sources, adding to the uncertainty. Factors such as ambient noise, equipment sensitivity, and placement accuracy can all influence the measurements, making it challenging to obtain clear and accurate measurements.
- **PULSE efficiency:** The assumed efficiency of different PULSE settings is an approximation based on the summation of individual energy losses. This method has not been validated with field data, which would provide a more accurate measure of efficiency.

Specific monopile configuration

- **Fixed monopile size and shape:** The results presented are based on a typical monopile currently in use. Variations in pile geometry and soil conditions could lead to different outcomes. While it is anticipated that different monopile sizes might not cause significant changes, further research is necessary to generalise the findings across various monopile configurations.

Air-bubble curtains

- **Air-bubble curtain model:** The current air-bubble curtain model appears to be effective at very low frequencies, which contradicts actual measurements. This discrepancy likely arises from the model's assumption of one-dimensional (z-dependent) transmission loss. While this assumption is reasonable for high frequencies, it becomes less accurate at low frequencies. Consequently, the model overestimates the air-bubble curtain's performance at low frequencies, suggesting it absorbs more sound than it actually does in practice.
- **Limited air-bubble curtain configurations:** The study only considered two specific configurations of air-bubble curtains. Different configurations – such as varying distances from the pile, using more compressors, or applying more frequent nozzles – could affect the combined efficiency with PULSE. Additionally, different soil configurations could alter the channelling effect of sound waves. The presence of very loose marine sediment in the topsoil layer in this study could lead to different results if this layer changes.

6.3. Recommendations for further research

Building upon the discussed limitations outlined in Section 6.2, recommendations for further research can be made. These recommendations are discussed in this section.

Review of the air-bubble curtain model

The unexpectedly good performance of the air-bubble curtain model at low frequencies necessitates further investigation. A filter was applied to frequencies below 32 Hz to address this issue. This involved using the unmitigated frequency response for frequencies up to 32 Hz and the mitigated response for frequencies above 32 Hz, with a smooth transition between the two around the 32 Hz mark. Despite these adjustments, the model significantly overestimated the measurements and failed to predict the noise levels accurately. Thus, the issue of the air-bubble curtains' performance at low frequencies could not be resolved using this method.

Therefore, the air-bubble curtain model needs to be reviewed and refined to better understand and account for its performance at low frequencies. Further research should focus on developing a more accurate model that can reliably predict the effectiveness of (D)BBCs across all frequency ranges. Additionally, the model could be improved by incorporating not only the vertical (z-direction) but also the radial (r) and angular (θ) dependencies. This would allow for a more accurate representation of sound wave interactions within the air-bubble curtain, leading to a better understanding of its overall effectiveness.

Variable monopile configurations

Understanding the effects of different monopile configurations is crucial for generalising the findings of this study and ensuring their applicability across a broader range of scenarios. Their design can vary significantly depending on factors such as size, water depth, and seabed conditions. Future research should focus on the following areas to enhance the understanding of how these variables impact noise mitigation measures:

- **Different monopile sizes:** Investigating how varying the diameter and length of monopiles affects their vibrational behaviour and noise radiation. Larger monopiles exhibit different resonance characteristics and energy transfer patterns compared to smaller ones. Especially as monopiles are increasing in size nowadays.
- **Different soil conditions:** The model would benefit from incorporating a broader range of soil conditions. The cases analysed in this study included a thick marine mud layer, which probably influenced the results. Additionally, modelling more than two soil layers would further enhance the accuracy of the model.

Extensive literature research on low-frequency noise mitigation

Given the current limitations of PULSE and air-bubble curtains in mitigating low-frequency noise, conducting an extensive literature review on this topic is highly recommended for further research. Low-frequency noise poses significant challenges due to its ability to propagate over long distances and potentially impact marine life, particularly species sensitive to these frequencies. Understanding and developing effective mitigation strategies for low-frequency noise is important. The review should focus on the following areas:

- **Current mitigation techniques:** Investigate existing techniques specifically designed to mitigate low-frequency noise, including their principles, applications, and effectiveness. This could include an exploration of resonance-based methods, such as large tethered encapsulated bubbles as researched by Lee et al. [35], acoustic metamaterials as discussed by Dong et al. [11], and other advanced technologies that have shown promise in reducing low-frequency noise.
- **Innovative approaches:** Review innovative approaches that have not yet been widely adopted in the industry but show potential for low-frequency noise reduction in other fields of engineering. Examples include the use of acoustic black holes for mitigating low-frequency noise [45].

Modelling of near-field noise mitigation measures

As detailed in Chapter 1, the Hydro-Sound-Damper-System (HSD-system) is one of the most commonly used mitigation measures for underwater noise, alongside PULSE and air-bubble curtains. The HSD-system involves surrounding the monopile with a net of PE-foam or rubber elements to dampen sound, adding another layer of noise reduction. This system operates through several mechanisms:

- **Absorption:** The system scatters sound waves by exciting elements at their resonant frequencies. Each element functions as a local resonator and can be tuned to different frequencies and water depths. The resonance frequency decreases with the size of the element. Additionally, the positioning of the elements on the net can be adjusted.
- **Reflection:** Sound waves reflect at the interface between water and air at the HSD-system due to the impedance mismatch between the two mediums [12].
- **Material damping and dissipation:** The choice of materials and the injected pressure within the HSD-system determine the level of damping and dissipation [59].

Modelling the HSD-system in this study was considered too complex to accurately simulate, particularly due to its vibrations caused by the vessel's movements. Given the time constraints of this study, accurately modelling these dynamics was not feasible. However, further research into this mitigation measure could be highly valuable, especially since it is often used in combination with the noise mitigation techniques discussed in this study. Integrating the HSD-system could potentially reduce overall noise levels further. However, it is expected to slightly increase low-frequency noise, as indicated by a study conducted by Bellmann et al. [5]. With limited data available without this system, its incorporation in the model would provide a significant amount of comparative data.

A study by Stahlmann et al. [57] offers a useful starting point for modelling an HSD-system, including research on finite element modelling. To model the HSD-system, a simplified model can be developed in COMSOL software, capturing the system's essential characteristics. An array of balloons can be simulated and tuned to absorb different frequencies, mimicking the behaviour of the HSD-elements. The model should account for the vessel-induced vibrations, simulating the up-and-down movements of the vessel. The insertion loss, or the noise reduction achieved by the HSD-system, can then be calculated.

This information can be integrated into the semi-analytical SILENCE model by using the calculated transmission loss as input.

Furthermore, it would be valuable to explore the modelling of the AdBm Noise Mitigation System (NMS). This technique is also widely used as a near-field noise mitigation measure and could provide additional insights into effective noise reduction strategies.

6.4. Study's value for the industry

This study provides insights for the marine construction and energy industries, particularly in the context of underwater noise mitigation. The research highlights the impact of varying input energy **over time** on underwater noise levels, offering a comprehensive understanding of how different PULSE settings and the integration of air-bubble curtains can mitigate noise pollution.

The analysis in this study used fixed input energy to ensure consistent comparisons across different PULSE settings and air-bubble curtain configurations. However, Appendix C extends this analysis by exploring the effects of reduced and increased hammer and input energies into the monopile on noise levels. This additional data allows industry stakeholders to estimate how energy changes impact noise levels, providing a broader understanding of the potential outcomes under various operational conditions. Specific estimated noise levels for multiple cases, derived from this scaling approach, are detailed in Tables C.1 to C.3 for varying hammer energies and in Tables C.4 to C.6 for varying input energies into the monopile.

References

[1] AdBm Technologies. *Technology: Effective, Reliable, and Environmentally Friendly*. 2020. URL: https://adbmtech.com/technology/ (visited on 07/03/2024).

[2] M. Aziman et al. "Compressive and Shear Wave Velocity Profiles using Seismic Refraction Technique". In: vol. 710. Institute of Physics Publishing, May 2016. DOI: 10.1088/1742-6596/710/1/012011.

[3] A.A. Bakr. "Axisymmetric Potential Problems". In: *The Boundary Integral Equation Method in Axisymmetric Stress Analysis Problems*. Berlin, Heidelberg: Springer Berlin Heidelberg, 1986. ISBN: 978-3-642-82644-3. DOI: 10.1007/978-3-642-82644-3_2. URL: https://doi.org/10.1007/978-3-642-82644-3_2.

[4] M.A. Bellmann, S. Gündert, and P. Remmer. *Offshore Messkampagne 1 (OMK 1) für das Projekt BORA im Windpark BARD Offshore 1*. 2014.

[5] M.A. Bellmann et al. *Underwater noise during percussive pile driving: Influencing factors on pile-driving noise and technical possibilities to comply with noise mitigation values*. 2020.

[6] T. Bohne, T. Grießmann, and R. Rolfes. "Development of an efficient buoyant jet integral model of a bubble plume coupled with a population dynamics model for bubble breakup and coalescence to predict the transmission loss of a bubble curtain". In: *International Journal of Multiphase Flow* 132 (Nov. 2020). ISSN: 03019322. DOI: 10.1016/j.ijmultiphaseflow.2020.103436.

[7] K. Brandt et al. *The mitigation of noise by a big bubble curtain: A study into the optimization of a big bubble curtain configuration and a contribution to noise mitigation modelling*. 2022. URL: https://repository.tudelft.nl/islandora/object/uuid%3A8710dd87-e05a-44d2-9d14-3052306108fa.

[8] M. Brüers, J. Poppitz, and M.A. Bellmann. *Messung der Unterwasserschallimmissionen im Offshore Windpark "**********": Abschlussbericht*. ****.

[9] S. Christoph, C. Henning, and P. Van Vuuren. *Pile Drivability Assessments*. ****.

[10] K.W. Commander and A. Prosperetti. "Linear pressure waves in bubbly liquids: Comparison between theory and experiments". In: *The Journal of the Acoustical Society of America* 85.2 (Feb. 1989), pp. 732–746. ISSN: 0001-4966. DOI: 10.1121/1.397599. eprint: https://pubs.aip.org/asa/jasa/article-pdf/85/2/732/11398559/732_1_online.pdf. URL: https://doi.org/10.1121/1.397599.

[11] E. Dong et al. "Underwater acoustic metamaterials". In: *National Science Review* 10.6 (Nov. 2022), nwac246. ISSN: 2095-5138. DOI: 10.1093/nsr/nwac246. eprint: https://academic.oup.com/nsr/article-pdf/10/6/nwac246/50268312/nwac246.pdf. URL: https://doi.org/10.1093/nsr/nwac246.

[12] K.H. Elmer et al. "Hydroschalldämpfer (HSD) zur Schallminderung bei Offshore Rammarbeiten". In: 2012.

[13] A. Euhus and M.A. Bellmann. *Prognose der zu erwartenden Unterwasserschall-Immissionen während der Rammarbeiten*. 2023.

[14] European Parliament. *Marine Strategy Framework Directive 2008/56/EC*. 2008.

[15] W.M. Ewing. *Elastic Waves in Layered Media*. McGraw-Hill, 1957.

[16] F. Fahy and D. Thompson. *Fundamentals of sound and vibration*. Vol. 2. 2015. ISBN: 9780367874872. URL: https://www.routledge.com/Fundamentals-of-Sound-and-Vibration/Fahy-Thompson/p/book/9780367874872.

[17] N.C.F. van Geel, D. Risch, and A. Wittich. "A brief overview of current approaches for underwater sound analysis and reporting". In: *Marine Pollution Bulletin* 178 (May 2022), p. 113610. ISSN: 0025-326X. DOI: 10.1016/J.MARPOLBUL.2022.113610.

[18] S. Gerlach and M.A. Bellmann. *Offshore Wind Farm Project "**********": Prognosis of the expected underwater sound emissions during pile-driving work*. 2020.

[19] GROW. *Gentle Driving of Piles (GDP)*. URL: https://grow-offshorewind.nl/project/gentle-driving-of-piles (visited on 01/02/2024).

[20] E.L. Hamilton. "Geoacoustic modeling of the sea floor". In: *Journal of the Acoustical Society of America* 68 (5 1980), pp. 1313–1340. ISSN: NA. DOI: 10.1121/1.385100.

[21] G. Hastie et al. "Effects of impulsive noise on marine mammals: investigating range-dependent risk". In: *Ecological applications : a publication of the Ecological Society of America* 29 (5 July 2019). ISSN: 1051-0761. DOI: 10.1002/EAP.1906. URL: https://pubmed.ncbi.nlm.nih.gov/30986328/.

[22] International Energy Agency. *World Energy Outlook 2019*. 2019. URL: https://www.iea.org/reports/world-energy-outlook-2019 (visited on 06/27/2024).

[23] IQIP. *Piling data D16*. ****.

[24] IQIP. *Piling data D26*. ****.

[25] IQIP. *PULSE – A smarter way to mitigate noise*. URL: https://iqip.com/pulse/ (visited on 12/10/2023).

[26] IQIP. *PULSE®*. URL: https://iqip.com/products/pile-driving-equipment/piling-under-limited-stress-equipment/ (visited on 12/10/2023).

[27] itap GmbH. *Messung der Hydroschallimmissionen bei den Rammarbeiten zur Gründung der D16 (Monopile) im Offshore-Windpark **********. ****.

[28] itap GmbH. *Messung der Hydroschallimmissionen bei den Rammarbeiten zur Gründung der D26 (Monopile) im Offshore-Windpark **********. ****.

[29] F.B. Jensen et al. *Computational Ocean Acoustics*. Vol. 2. 2011. URL: http://www.springer.com/series/3754.

[30] J. Jung, S. Goo, and J. Kook. "Predicting anti-resonance frequencies using a novel eigenvalue formulation". In: *Finite Elements in Analysis and Design* 191 (2021), p. 103525. ISSN: 0168-874X. DOI: https://doi.org/10.1016/j.finel.2021.103525. URL: https://www.sciencedirect.com/science/article/pii/S0168874X21000093.

[31] J. Kaplunov, E. Nolde, and L. Kossovich. "Dynamics of Thin Walled Elastic Bodies". In: 1997. URL: https://api.semanticscholar.org/CorpusID:117224450.

[32] F. Kirsch, K. Grivas, and C.T. Akdag. ***********: Main Soil and Foundation Expertise Report*. ****.

[33] E. Klages et al. "Reducing offshore pile driving noise: Shape optimization of the impact hammer". In: 2019.

[34] S. Koschinski and K. Lüdemann. *Noise mitigation for the construction of increasingly large offshore wind turbines: Technical options for complying with noise limits*. 2020.

[35] K.M. Lee, M.S. Wochner, and P.S. Wilson. "Mitigation of low-frequency underwater noise generated by rotating machinery on a mobile work barge using large tethered encapsulated bubbles". In: *The Journal of the Acoustical Society of America* 131.4_Supplement (Apr. 2012), pp. 3507–3507. ISSN: 0001-4966. DOI: 10.1121/1.4709259. URL: https://doi.org/10.1121/1.4709259.

[36] S. Lippert, H. Lohmann, and H. Marckmann. *Prediction of the underwater noise emission during construction of the ********** offshore wind farm*. ****.

[37] M. Long. "Fundamentals of Acoustics". In: *Architectural Acoustics* (Jan. 2014), pp. 39–79. DOI: 10.1016/B978-0-12-398258-2.00002-7.

[38] A. MacGillivray. "Finite difference computational modeling of marine impact pile driving". In: vol. 136. June 2015. DOI: 10.1121/1.4900002.

[39] P.T. Madsen. "Marine mammals and noise: Problems with root mean square sound pressure levels for transients". In: *The Journal of the Acoustical Society of America* 117 (6 June 2005), pp. 3952–3957. ISSN: 0001-4966. DOI: 10.1121/1.1921508. URL: /asa/jasa/article/117/6/3952/543678/Marine-mammals-and-noise-Problems-with-root-mean.

[40] H. Masoumi and G. Degrande. "Numerical modeling of free field vibrations due to pile driving using a dynamic soil-structure interaction formulation". In: *Journal of Computational and Applied Mathematics* 215 (June 2008), pp. 503–511. DOI: 10.1016/j.cam.2006.03.051.

[41] H. Masoumi, G. Degrande, and G. Lombaert. "Prediction of free field vibrations due to pile driving using a dynamic soil-structure interaction formulation". In: *Soil Dynamics and Earthquake Engineering* 27.2 (Jan. 2007), pp. 126–143. DOI: 10.1016/j.soildyn.2006.05.005.

[42] H. Masoumi, S. François, and G. Degrande. "A non-linear coupled finite element–boundary element model for the prediction of vibrations due to vibratory and impact pile driving". In: *International Journal for Numerical and Analytical Methods in Geomechanics* 33 (Feb. 2009), pp. 245–274. DOI: 10.1002/nag.719.

[43] G. Nehls and M.A. Bellmann. *Weiterentwicklung und Erprobung des "Großen Blasenschleiers" zur Minderung der Hydroschallemissionen bei Offshore-Rammarbeiten: Schlussbericht*. Tech. Rep. Bio-Consult SH GmbH & Company KG; itap GmbH Oldenburg; Hydrotechnik Lubeck, 2016. DOI: 10.2314/GBV:868671320.

[44] OffNoise-Solutions. *The Hydro-Sound-Damper-System (HSD-System)*. URL: https://www.offnoise-solutions.com/the-hydro-sound-damper-system-hsd-system/ (visited on 01/02/2024).

[45] A. Azbaid El Ouahabi, V. Krylov, and D. O'Boy. "Experimental investigation of the acoustic black hole for sound absorption in air". In: July 2015.

[46] Y. Peng, A.J. Laguna, and A. Tsouvalas. "A multi-physics approach for modelling noise mitigation using an air-bubble curtain in impact pile driving". In: *Frontiers in Marine Science* 10 (Oct. 2023). ISSN: 22967745.

[47] Y. Peng, A. Tsouvalas, and A. Metrikine. "A coupled modelling approach for the fast computation of underwater noise radiation from offshore pile driving". In: 2 (2020), pp. 2427–2436. ISSN: 2427-2436. DOI: 10.47964/1120.9196.18574. URL: www.easdprocedia.org.

[48] Y. Peng et al. "A fast computational model for near- and far-field noise prediction due to offshore pile driving". In: *The Journal of the Acoustical Society of America* 149 (3 Mar. 2021), pp. 1772–1790. ISSN: 0001-4966. DOI: 10.1121/10.0003752.

[49] Y. Peng et al. "Study of the Sound Escape with the Use of an Air Bubble Curtain in Offshore Pile Driving". In: *Journal of Marine Science and Engineering 2021, Vol. 9, Page 232* 9 (2 Feb. 2021), p. 232. ISSN: 2077-1312. DOI: 10.3390/JMSE9020232. URL: https://www.mdpi.com/2077-1312/9/2/232.

[50] A.D. Pierce. *Acoustics: An Introduction to Its Physical Principles and Applications*. Vol. 3. 2019.

[51] A.N. Popper and M.C. Hastings. "The effects of human-generated sound on fish". In: *Integrative Zoology* 4.1 (2009), pp. 43–52. DOI: 10.1111/j.1749-4877.2008.00134.x.

[52] P. Reinhall and P. Dahl. "Underwater Mach wave radiation from impact pile driving: Theory and observation". In: *The Journal of the Acoustical Society of America* 130 (Sept. 2011), pp. 1209–16. DOI: 10.1121/1.3614540.

[53] Rijksoverheid. *Kavelbesluit II windenergiegebied Borssele*. 2016. URL: https://wetten.overheid.nl/BWBR0037801/2016-04-09.

[54] S. Sánchez et al. "Foundations in Offshore Wind Farms: Evolution, Characteristics and Range of Use. Analysis of Main Dimensional Parameters in Monopile Foundations". In: *Journal of Marine Science and Engineering* 7.12 (2019). ISSN: 2077-1312. DOI: 10.3390/jmse7120441. URL: https://www.mdpi.com/2077-1312/7/12/441.

[55] A.W. Shapiro. *The dynamics and thermodynamics of compressible fluid flow*. Ronald, 1953.

[56] H. Slabbekoorn et al. "A noisy spring: the impact of globally rising underwater sound levels on fish". In: *Trends in Ecology & Evolution* 25.7 (2010), pp. 419–427. ISSN: 0169-5347. DOI: https://doi.org/10.1016/j.tree.2010.04.005. URL: https://www.sciencedirect.com/science/article/pii/S0169534710000832.

[57] J. Stahlmann et al. *Untersuchung und Erprobung von Hydro-Schall-Dämpfern (HSD) zur Minderung von Unterwasserschall bei Rammarbeiten für Gründungen von OWEA*. 2015.

[58] D. Steven et al. “Executive summary: Assessing and managing the effect sphere of influence.” In: *Environmental impacts of offshore wind farms in the Belgian part of the North Sea: assessing and managing effect spheres of influence. Memoirs on the Marine Environment*. 201. ISBN: 978-9-0732-4242-5.

[59] A. Tsouvalas. “Underwater Noise Emission Due to Offshore Pile Installation: A Review”. In: *Energies 2020, Vol. 13, Page 3037* 13 (12 June 2020), p. 3037. ISSN: 1996-1073. DOI: 10.3390/EN13123037. URL: https://www.mdpi.com/1996-1073/13/12/3037/htm%20https://www.mdpi.com/1996-1073/13/12/3037.

[60] A. Tsouvalas. “Underwater noise generated by offshore pile driving”. In: (2015).

[61] A. Tsouvalas and A. Metrikine. “A semi-analytical model for the prediction of underwater noise from offshore pile driving”. In: *Journal of Sound and Vibration* 332 (June 2013), pp. 3232–3257. DOI: 10.1016/j.jsv.2013.01.026.

[62] A. Tsouvalas and A. Metrikine. “A three-dimensional vibroacoustic model for the prediction of underwater noise from offshore pile driving”. In: *Journal of Sound and Vibration* 333 (8 Apr. 2014), pp. 2283–2311. ISSN: 0022-460X. DOI: 10.1016/J.JSV.2013.11.045.

[63] A. Tsouvalas and A. Metrikine. “Noise reduction by the application of an air-bubble curtain in offshore pile driving”. In: *Journal of Sound and Vibration* 371 (June 2016), pp. 150–170. ISSN: 0022-460X. DOI: 10.1016/J.JSV.2016.02.025.

[64] A. Tsouvalas, Y. Peng, and A. Metrikine. “Underwater noise generated by offshore pile driving: A pile-soil-water vibroacoustic model based on a mode matching method”. In: *Conference: 5th International Conference and Exhibition on Underwater Acoustics (UACE2019)* (2019). URL: https://www.researchgate.net/publication/334947429.

[65] Umwelt Bundesamt. *Underwater noise*. 2020. URL: https://www.bsh.de/EN/TOPICS/Offshore/Environmental_assessments/Underwater_sound/underwater_sound_node.html (visited on 01/03/2024).

[66] United Nations Framework Convention on Climate Change. *The Paris Agreement*. 2015. URL: https://unfccc.int/sites/default/files/resource/parisagreement_publication.pdf (visited on 06/27/2024).

A

Individual recordings of the hydrophones

A.1. Monopile D26

SEL measurements

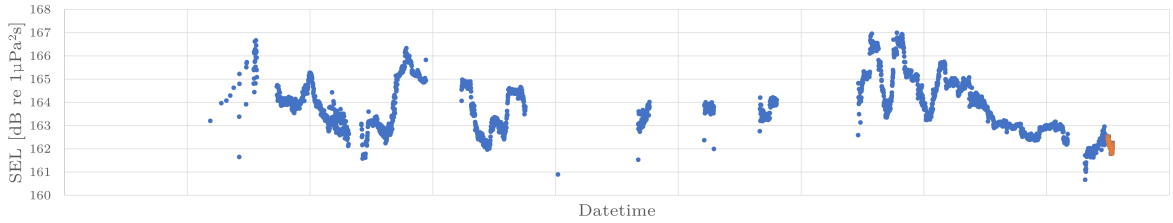

Figure A.1: SEL measurements for monopile D26 monitored over time, depicting hydrophone *D26_B750_1*. The orange part highlights the blows necessary for the final 25 cm penetration.

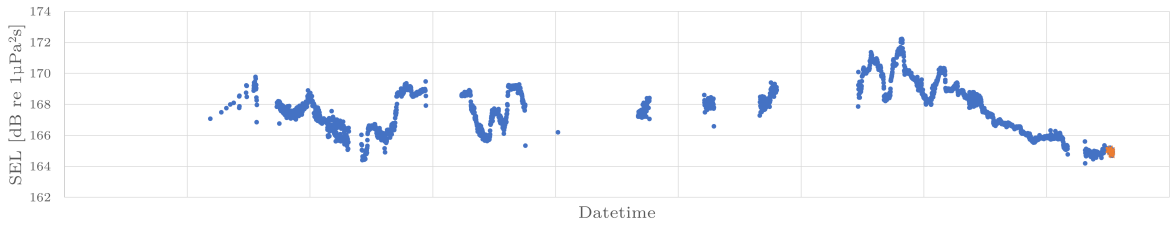

Figure A.2: SEL measurements for monopile D26 monitored over time, depicting hydrophone *D26_B750_2*. The orange part highlights the blows necessary for the final 25 cm penetration.

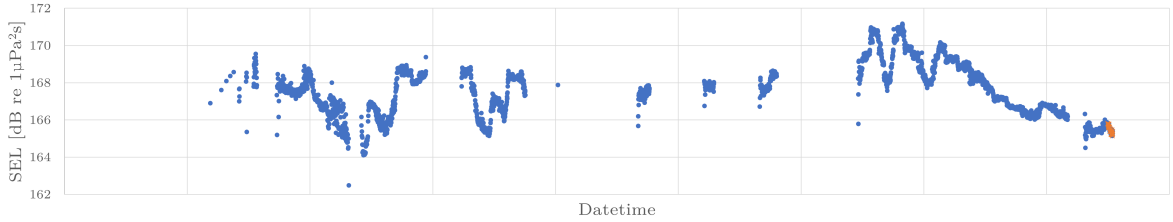

Figure A.3: SEL measurements for monopile D26 monitored over time, depicting hydrophone *D26_B750_3*. The orange part highlights the blows necessary for the final 25 cm penetration.

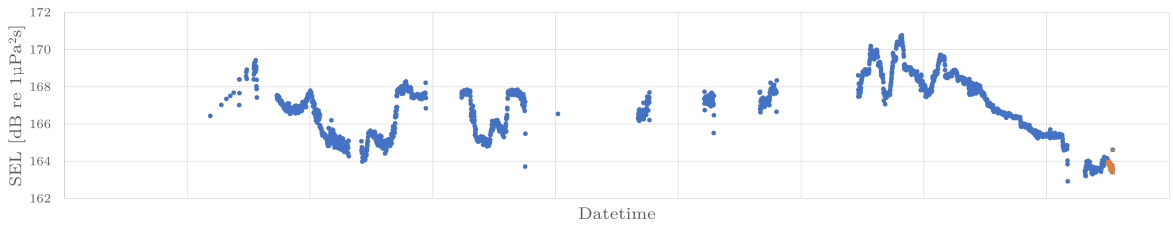

Figure A.4: SEL measurements for monopile D26 monitored over time, depicting hydrophone *D26_B750_4*. The orange part highlights the blows necessary for the final 25 cm penetration.

L_{peak} measurements

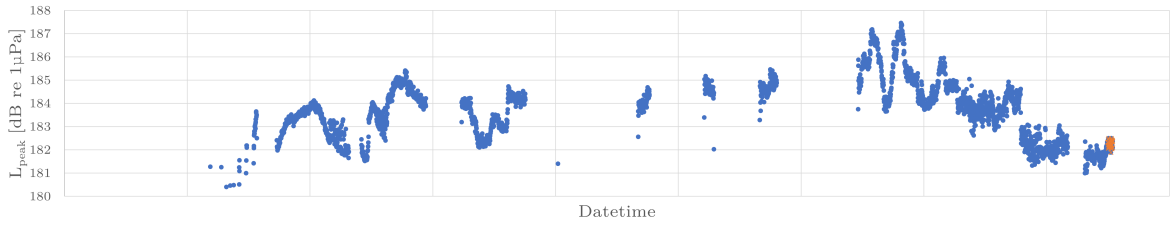

Figure A.5: L_{peak} measurements for monopile D26 monitored over time, depicting hydrophone *D26_B750_1*. The orange part highlights the blows necessary for the final 25 cm penetration.

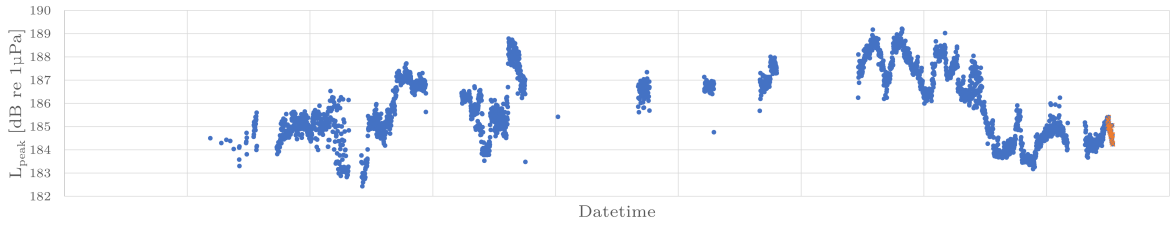

Figure A.6: L_{peak} measurements for monopile D26 monitored over time, depicting hydrophone *D26_B750_2*. The orange part highlights the blows necessary for the final 25 cm penetration.

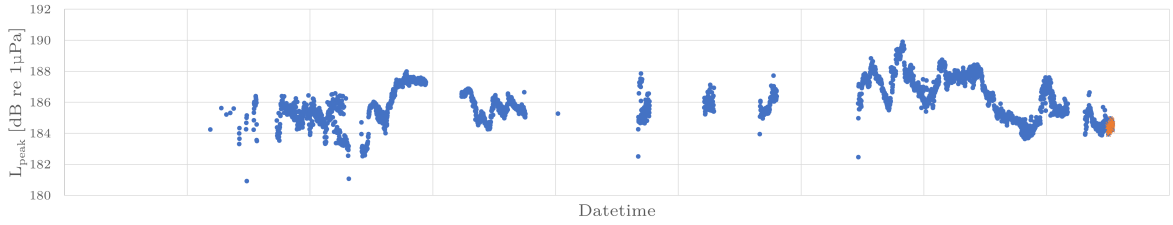

Figure A.7: L_{peak} measurements for monopile D26 monitored over time, depicting hydrophone *D26_B750_3*. The orange part highlights the blows necessary for the final 25 cm penetration.

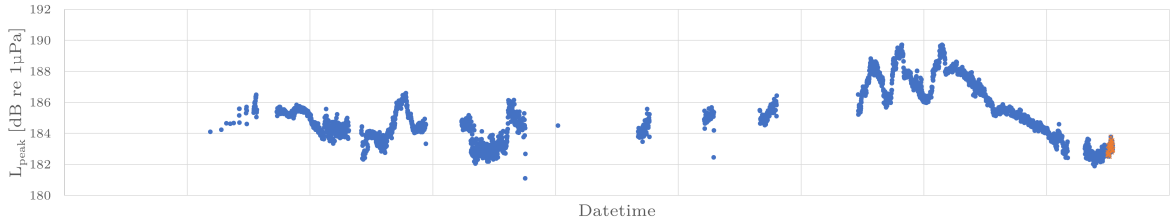

Figure A.8: L_{peak} measurements for monopile D26 monitored over time, depicting hydrophone *D26_B750_4*. The orange part highlights the blows necessary for the final 25 cm penetration.

A.2. Monopile D16

SEL measurements

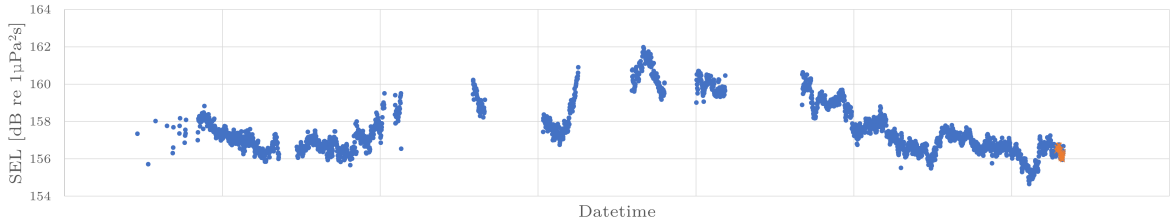

Figure A.9: SEL measurements for monopile D16 monitored over time, depicting hydrophone *D16_B750_1*. The orange part highlights the blows necessary for the final 25 cm penetration.

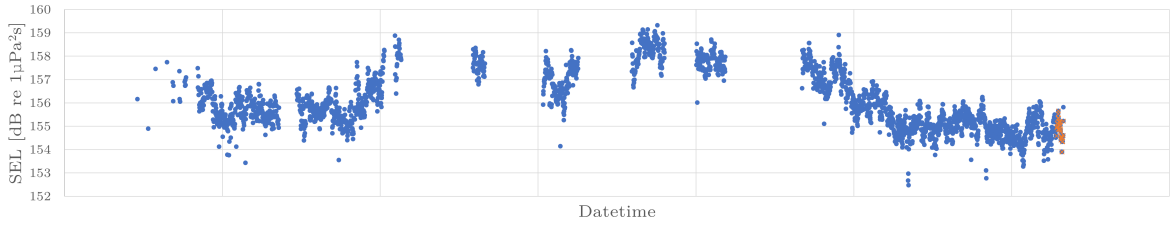

Figure A.10: SEL measurements for monopile D16 monitored over time, depicting hydrophone *D16_B750_2*. The orange part highlights the blows necessary for the final 25 cm penetration.

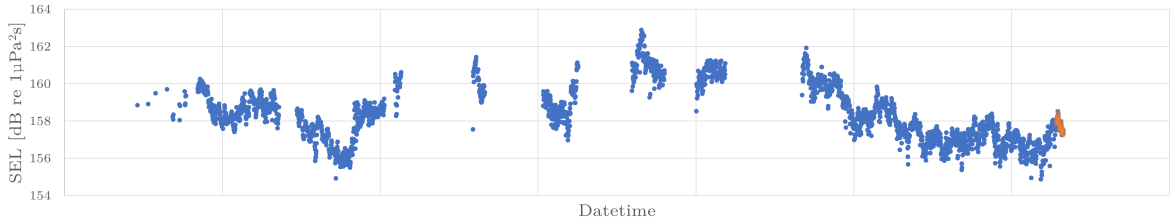

Figure A.11: SEL measurements for monopile D16 monitored over time, depicting hydrophone *D16_B750_3*. The orange part highlights the blows necessary for the final 25 cm penetration.

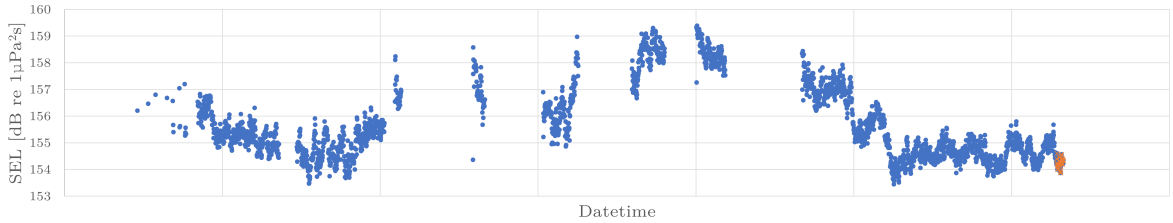

Figure A.12: SEL measurements for monopile D16 monitored over time, depicting hydrophone *D16_B750_4*. The orange part highlights the blows necessary for the final 25 cm penetration.

L_{peak} measurements

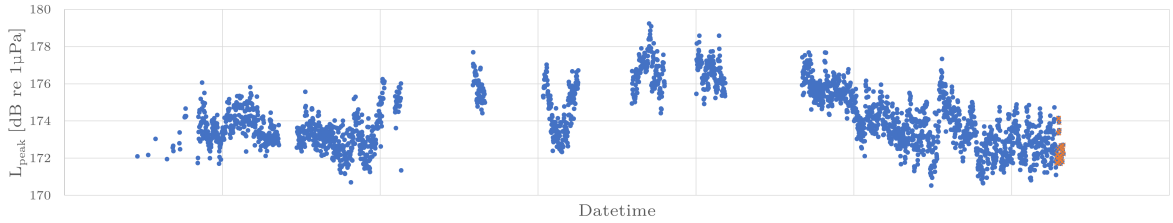

Figure A.13: L_{peak} measurements for monopile D16 monitored over time, depicting hydrophone *D16_B750_1*. The orange part highlights the blows necessary for the final 25 cm penetration.

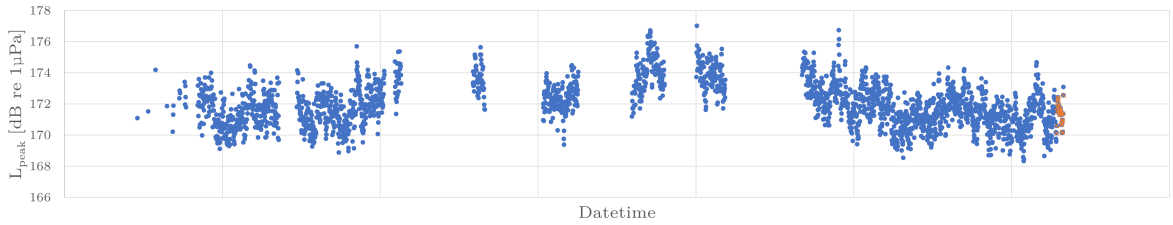

Figure A.14: L_{peak} measurements for monopile D16 monitored over time, depicting hydrophone *D16_B750_2*. The orange part highlights the blows necessary for the final 25 cm penetration.

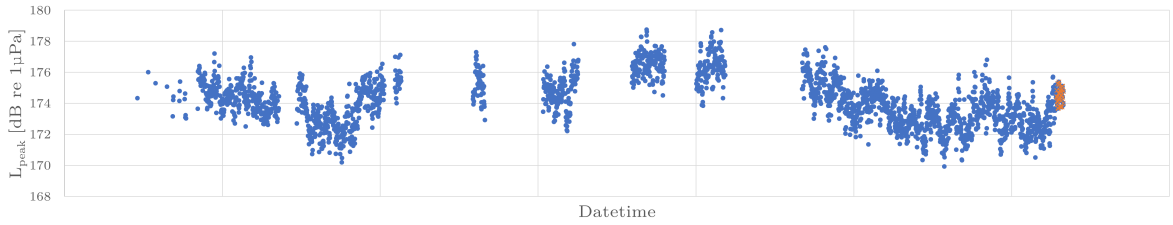

Figure A.15: L_{peak} measurements for monopile D16 monitored over time, depicting hydrophone *D16_B750_3*. The orange part highlights the blows necessary for the final 25 cm penetration.

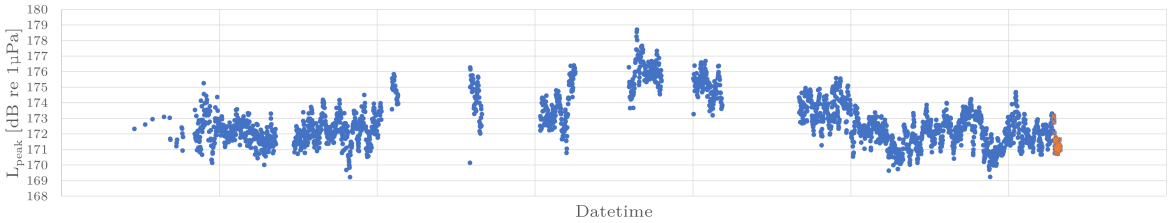

Figure A.16: L_{peak} measurements for monopile D16 monitored over time, depicting hydrophone *D16_B750_4*. The orange part highlights the blows necessary for the final 25 cm penetration.

B

Pile vibrations

B.1. Vibrations in vertical direction

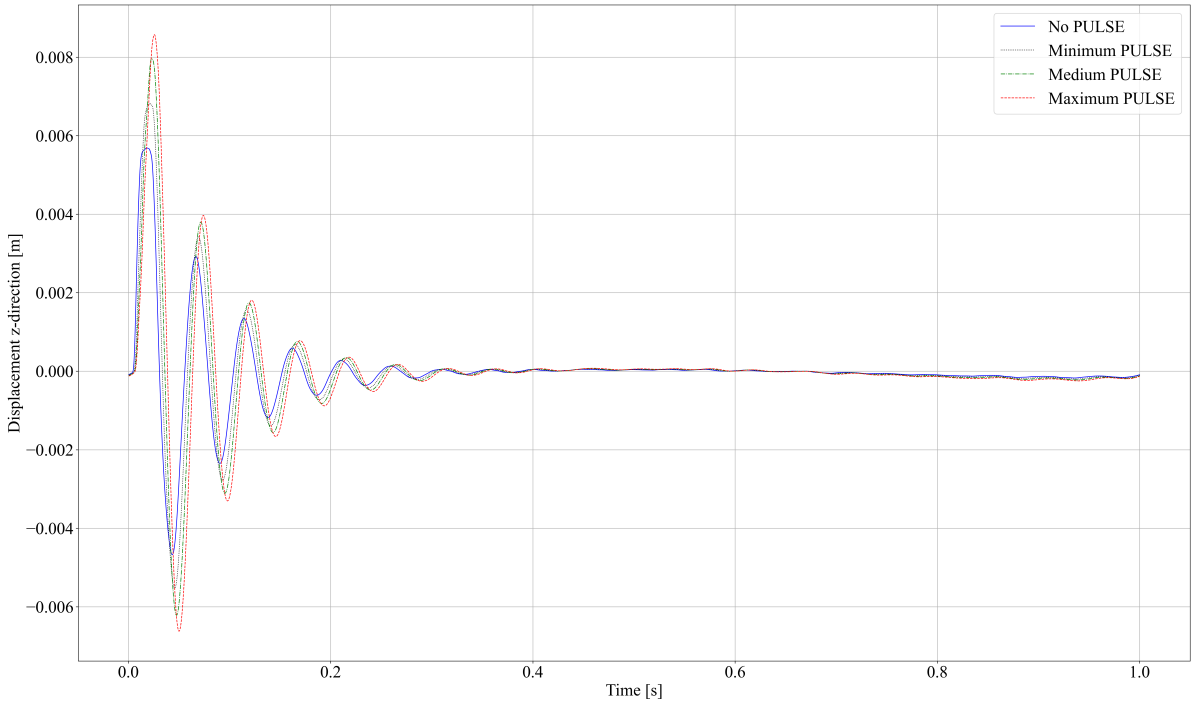

Figure B.1: Vibrations of the monopile in z-direction at 0.1 times the length.

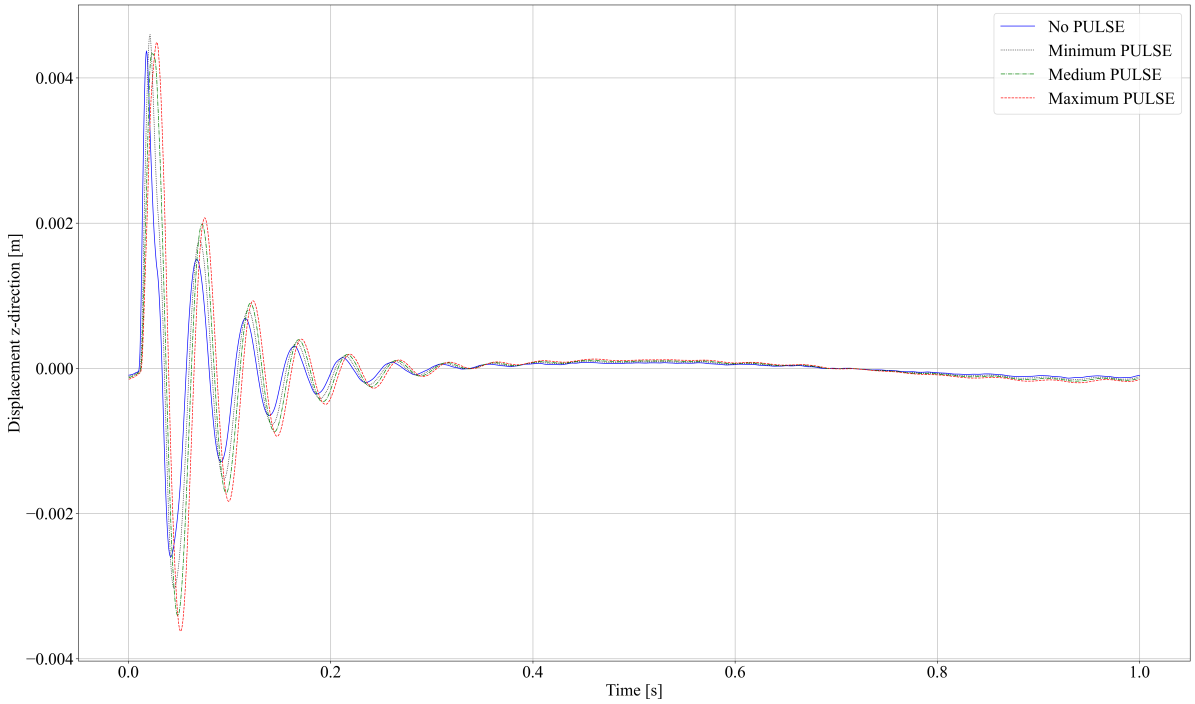

Figure B.2: Vibrations of the monopile in z-direction at 0.5 times the length.

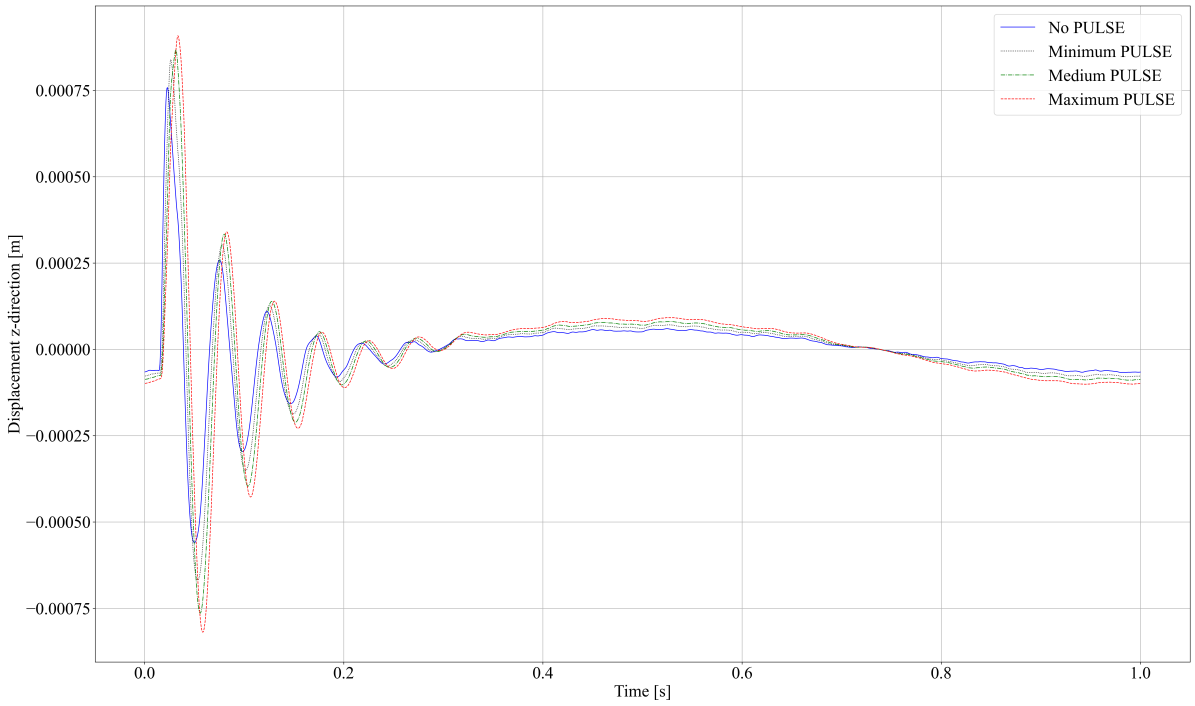

Figure B.3: Vibrations of the monopile in z-direction at 0.8 times the length.

B.2. Vibrations in radial direction

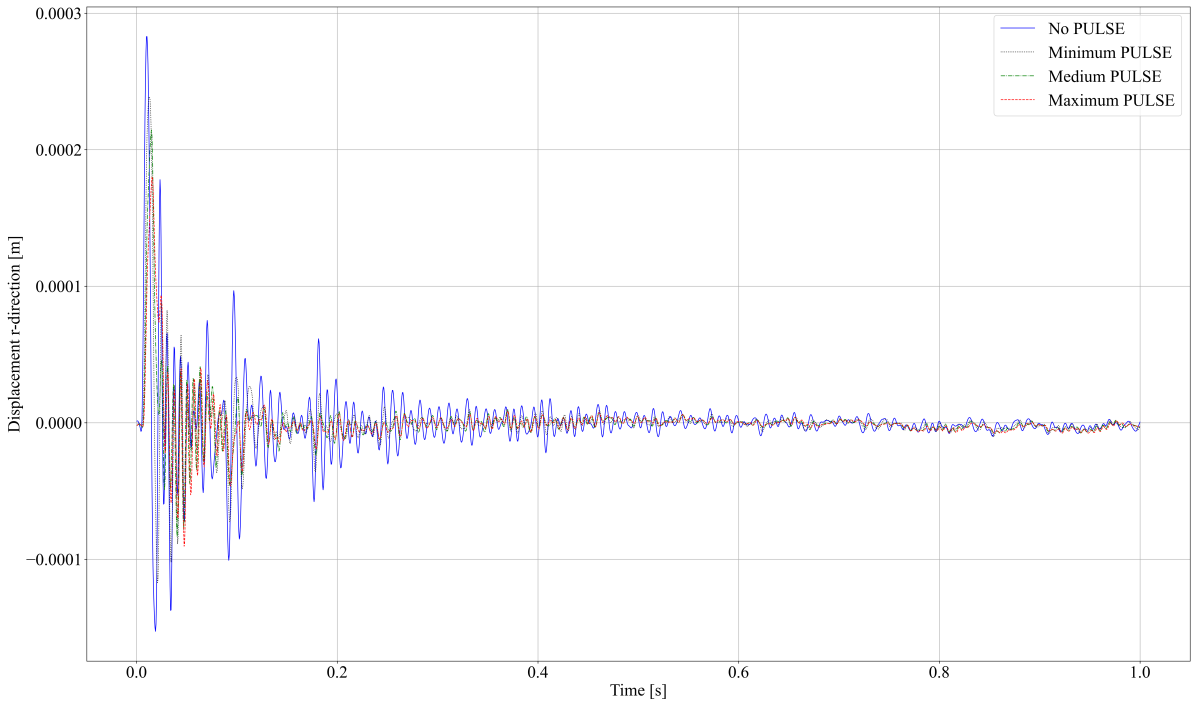

Figure B.4: Vibrations of the monopile in r-direction at 0.1 times the length.

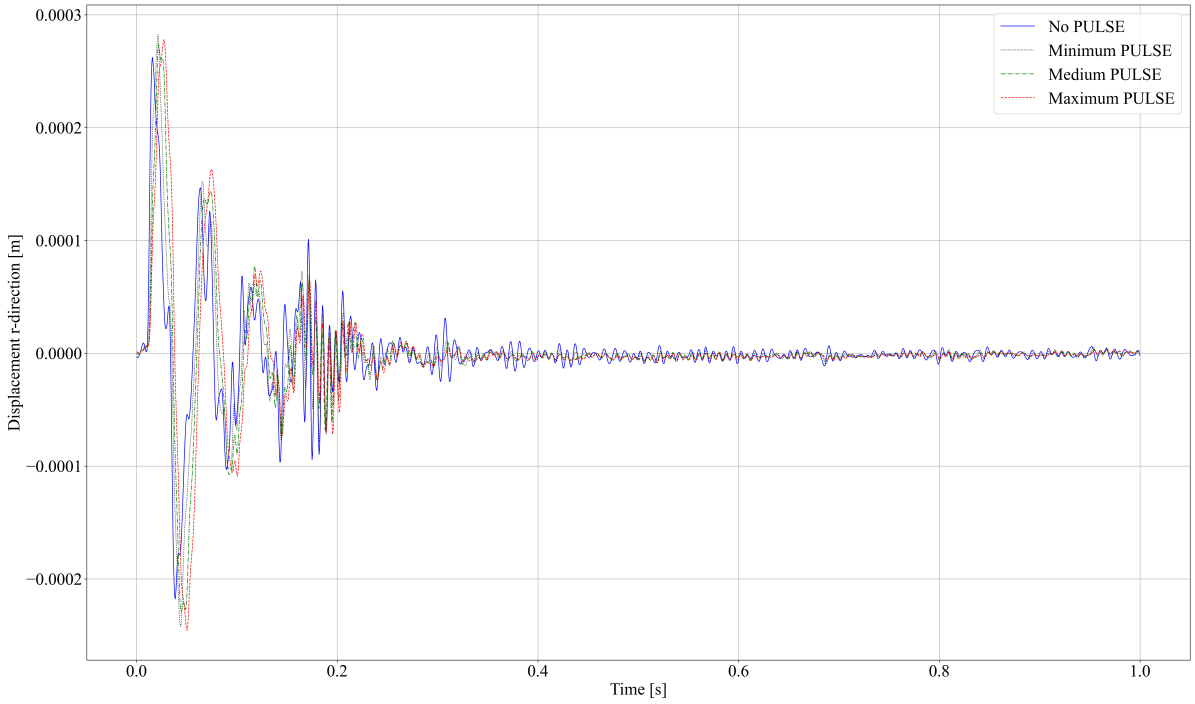

Figure B.5: Vibrations of the monopile in r-direction at 0.5 times the length.

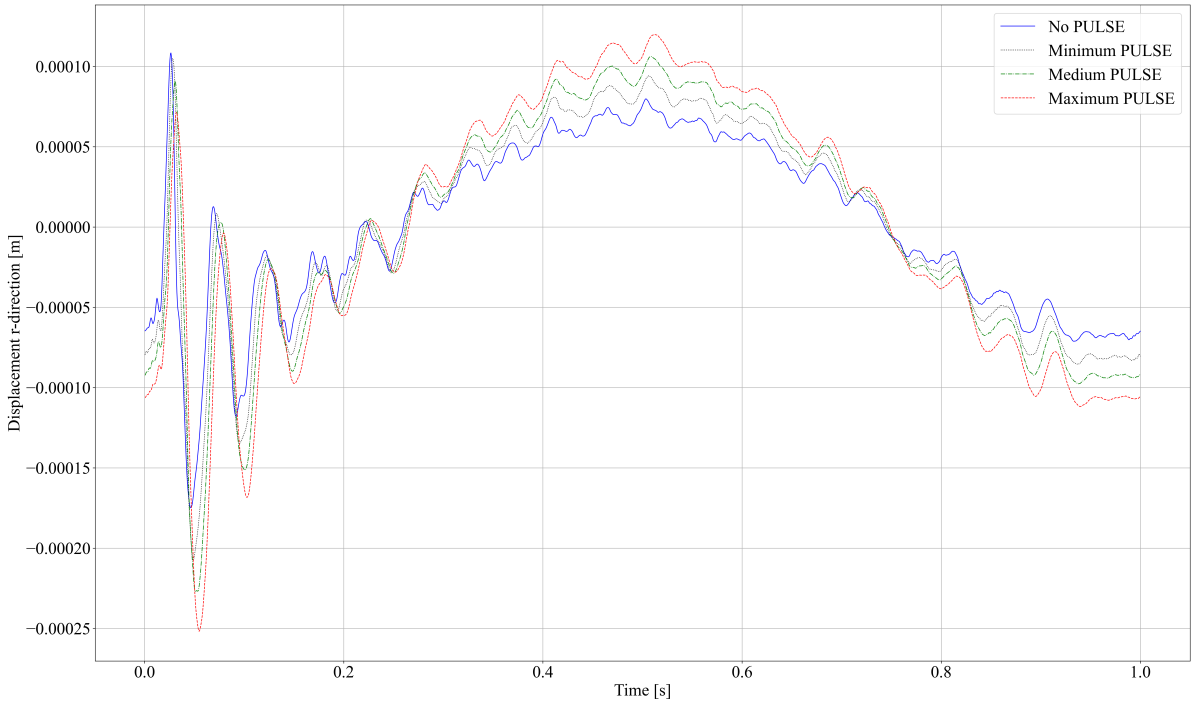

Figure B.6: Vibrations of the monopile in r-direction at 0.8 times the length.

C

Effect of reduced or increased energy on the noise levels

The values presented in this appendix are given in [dB re 1 μPa^2] for SEL and in [dB re 1 μPa] for L_{peak}.

C.1. Hammer energy

PULSE without additional mitigation measures

Table C.1: Predicted SEL and L_{peak} values for different hammer energies across various PULSE settings, without additional mitigation measures

Hammer energy	**No PULSE**		**Minimum PULSE**		**Medium PULSE**		**Maximum PULSE**	
[kJ]	**SEL**	**L_{peak}**	**SEL**	**L_{peak}**	**SEL**	**L_{peak}**	**SEL**	**L_{peak}**
200	167.8	186.6	165.9	183.0	164.0	179.3	163.2	178.7
400	170.8	189.7	168.9	186.0	167.0	182.3	166.2	181.7
600	172.6	191.4	170.6	187.7	168.7	184.1	168.0	183.5
800	173.8	192.7	171.9	189.0	170.0	185.3	169.2	184.8
1000	174.8	193.6	172.9	190.0	171.0	186.3	170.2	185.7
1200	175.6	194.4	173.7	190.8	171.7	187.1	171.0	186.5
1400	176.3	195.1	174.3	191.4	172.4	187.8	171.7	187.2
1600	176.9	195.7	174.9	192.0	173.0	188.3	172.2	187.8
1800	177.4	196.2	175.4	192.5	173.5	188.8	172.8	188.3
2000	177.8	196.6	175.9	193.0	174.0	189.3	173.2	188.7
2200	178.2	197.1	176.3	193.4	174.4	189.7	173.6	189.1
2400	178.6	197.4	176.7	193.8	174.8	190.1	174.0	189.5
2600	179.0	197.8	177.0	194.1	175.1	190.4	174.4	189.9
2800	179.3	198.1	177.3	194.4	175.4	190.8	174.7	190.2
3000	179.6	198.4	177.6	194.7	175.7	191.1	175.0	190.5
3200	179.9	198.7	177.9	195.0	176.0	191.3	175.3	190.8
3400	180.1	199.0	178.2	195.3	176.3	191.6	175.5	191.0
3600	180.4	199.2	178.4	195.5	176.5	191.9	175.8	191.3
3800	180.6	199.4	178.7	195.8	176.8	192.1	176.0	191.5
4000	180.8	199.7	178.9	196.0	177.0	192.3	176.2	191.7

PULSE combined with a BBC

Table C.2: Predicted SEL and L_{peak} values for different hammer energies across various PULSE settings, combined with a BBC

Hammer energy	**No PULSE**		**Minimum PULSE**		**Medium PULSE**		**Maximum PULSE**	
[kJ]	**SEL**	**L_{peak}**	**SEL**	**L_{peak}**	**SEL**	**L_{peak}**	**SEL**	**L_{peak}**
200	160.7	181.3	158.6	177.8	156.5	173.9	155.7	171.4
400	163.7	184.3	161.6	180.8	159.6	176.9	158.7	174.5
600	165.4	186.0	163.4	182.5	161.3	178.6	160.5	176.2
800	166.7	187.3	164.7	183.8	162.6	179.9	161.7	177.5
1000	167.6	188.3	165.6	184.7	163.5	180.9	162.7	178.4
1200	168.4	189.0	166.4	185.5	164.3	181.6	163.5	179.2
1400	169.1	189.7	167.1	186.2	165.0	182.3	164.2	179.9
1600	169.7	190.3	167.7	186.8	165.6	182.9	164.8	180.5
1800	170.2	190.8	168.2	187.3	166.1	183.4	165.3	181.0
2000	170.7	191.3	168.6	187.8	166.5	183.9	165.7	181.4
2200	171.1	191.7	169.1	188.2	167.0	184.3	166.1	181.9
2400	171.4	192.1	169.4	188.6	167.3	184.7	166.5	182.2
2600	171.8	192.4	169.8	188.9	167.7	185.0	166.9	182.6
2800	172.1	192.7	170.1	189.2	168.0	185.3	167.2	182.9
3000	172.4	193.0	170.4	189.5	168.3	185.6	167.5	183.2
3200	172.7	193.3	170.7	189.8	168.6	185.9	167.8	183.5
3400	173.0	193.6	170.9	190.1	168.9	186.2	168.0	183.7
3600	173.2	193.8	171.2	190.3	169.1	186.4	168.3	184.0
3800	173.4	194.0	171.4	190.5	169.3	186.6	168.5	184.2
4000	173.7	194.3	171.6	190.8	169.6	186.9	168.7	184.5

PULSE combined with a DBBC

Table C.3: Predicted SEL and L_{peak} values for different hammer energies across various PULSE settings, combined with a DBBC

Hammer energy	**No PULSE**		**Minimum PULSE**		**Medium PULSE**		**Maximum PULSE**	
[kJ]	**SEL**	**L_{peak}**	**SEL**	**L_{peak}**	**SEL**	**L_{peak}**	**SEL**	**L_{peak}**
200	157.1	178.1	154.9	174.4	152.1	170.4	151.0	167.8
400	160.1	181.2	157.9	177.4	155.1	173.4	154.1	170.8
600	161.9	182.9	159.7	179.2	156.9	175.1	155.8	172.6
800	163.1	184.2	160.9	180.4	158.1	176.4	157.1	173.8
1000	164.1	185.1	161.9	181.4	159.1	177.4	158.0	174.8
1200	164.9	185.9	162.7	182.2	159.9	178.1	158.8	175.6
1400	165.5	186.6	163.4	182.9	160.6	178.8	159.5	176.2
1600	166.1	187.2	163.9	183.4	161.1	179.4	160.1	176.8
1800	166.6	187.7	164.5	183.9	161.7	179.9	160.6	177.3
2000	167.1	188.1	164.9	184.4	162.1	180.4	161.0	177.8
2200	167.5	188.6	165.3	184.8	162.5	180.8	161.5	178.2
2400	167.9	188.9	165.7	185.2	162.9	181.2	161.8	178.6
2600	168.2	189.3	166.1	185.5	163.3	181.5	162.2	178.9
2800	168.6	189.6	166.4	185.9	163.6	181.8	162.5	179.2
3000	168.9	189.9	166.7	186.2	163.9	182.1	162.8	179.5
3200	169.1	190.2	167.0	186.4	164.2	182.4	163.1	179.8
3400	169.4	190.5	167.2	186.7	164.4	182.7	163.3	180.1
3600	169.7	190.7	167.5	187.0	164.7	182.9	163.6	180.3
3800	169.9	190.9	167.7	187.2	164.9	183.1	163.8	180.6
4000	170.1	191.2	167.9	187.4	165.1	183.4	164.1	180.8

C.2. Input energy

PULSE without additional mitigation measures

Table C.4: Predicted SEL and L_{peak} values for different input energies into the pile across various PULSE settings, without additional mitigation measures

Input energy	**No PULSE**		**Minimum PULSE**		**Medium PULSE**		**Maximum PULSE**	
[kJ]	**SEL**	$\mathbf{L_{peak}}$	**SEL**	$\mathbf{L_{peak}}$	**SEL**	$\mathbf{L_{peak}}$	**SEL**	$\mathbf{L_{peak}}$
200	168.5	187.3	166.8	183.9	165.3	180.6	165.0	180.5
370	171.1	190.0	169.5	186.6	167.9	183.3	167.7	183.2
400	171.5	190.3	169.8	186.9	168.3	183.6	168.0	183.5
600	173.3	192.1	171.6	188.7	170.0	185.4	169.8	185.3
800	174.5	193.3	172.8	189.9	171.3	186.6	171.0	186.6
1000	175.5	194.3	173.8	190.9	172.3	187.6	172.0	187.5
1200	176.3	195.1	174.6	191.7	173.1	188.4	172.8	188.3
1400	176.9	195.7	175.2	192.3	173.7	189.0	173.4	189.0
1600	177.5	196.3	175.8	192.9	174.3	189.6	174.0	189.6
1800	178.0	196.8	176.3	193.4	174.8	190.2	174.6	190.1
2000	178.5	197.3	176.8	193.9	175.3	190.6	175.0	190.5
2200	178.9	197.7	177.2	194.3	175.7	191.0	175.4	191.0
2400	179.3	198.1	177.6	194.7	176.1	191.4	175.8	191.3
2600	179.6	198.4	177.9	195.0	176.4	191.8	176.2	191.7
2800	179.9	198.8	178.2	195.3	176.7	192.1	176.5	192.0
3000	180.2	199.1	178.5	195.6	177.0	192.4	176.8	192.3
3200	180.5	199.3	178.8	195.9	177.3	192.7	177.1	192.6
3400	180.8	199.6	179.1	196.2	177.6	192.9	177.3	192.8
3600	181.0	199.9	179.3	196.4	177.8	193.2	177.6	193.1
3800	181.3	200.1	179.6	196.7	178.1	193.4	177.8	193.3
4000	181.5	200.3	179.8	196.9	178.3	193.6	178.0	193.5

PULSE combined with a BBC

Table C.5: Predicted SEL and L_{peak} values for different input energies into the pile across various PULSE settings, combined with a BBC

Input energy	**No PULSE**		**Minimum PULSE**		**Medium PULSE**		**Maximum PULSE**	
[kJ]	**SEL**	**L_{peak}**	**SEL**	**L_{peak}**	**SEL**	**L_{peak}**	**SEL**	**L_{peak}**
200	161.3	181.9	159.6	178.7	157.9	175.2	157.5	173.2
370	164.0	184.6	162.2	181.3	160.5	177.8	160.2	175.9
400	164.3	184.9	162.6	181.7	160.9	178.2	160.5	176.3
600	166.1	186.7	164.3	183.4	162.6	179.9	162.3	178.0
800	167.3	187.9	165.6	184.7	163.9	181.2	163.6	179.3
1000	168.3	188.9	166.5	185.7	164.8	182.2	164.5	180.2
1200	169.1	189.7	167.3	186.5	165.6	183.0	165.3	181.0
1400	169.7	190.3	168.0	187.1	166.3	183.6	166.0	181.7
1600	170.3	190.9	168.6	187.7	166.9	184.2	166.6	182.3
1800	170.9	191.5	169.1	188.2	167.4	184.7	167.1	182.8
2000	171.3	191.9	169.6	188.7	167.9	185.2	167.5	183.2
2200	171.7	192.3	170.0	189.1	168.3	185.6	167.9	183.7
2400	172.1	192.7	170.3	189.5	168.6	186.0	168.3	184.0
2600	172.4	193.1	170.7	189.8	169.0	186.3	168.7	184.4
2800	172.8	193.4	171.0	190.1	169.3	186.6	169.0	184.7
3000	173.1	193.7	171.3	190.4	169.6	186.9	169.3	185.0
3200	173.4	194.0	171.6	190.7	169.9	187.2	169.6	185.3
3400	173.6	194.2	171.9	191.0	170.2	187.5	169.8	185.5
3600	173.9	194.5	172.1	191.2	170.4	187.7	170.1	185.8
3800	174.1	194.7	172.3	191.5	170.6	188.0	170.3	186.0
4000	174.3	194.9	172.6	191.7	170.9	188.2	170.5	186.3

PULSE combined with a DBBC

Table C.6: Predicted SEL and L_{peak} values for different input energies into the pile across various PULSE settings, combined with a DBBC

Input energy	**No PULSE**		**Minimum PULSE**		**Medium PULSE**		**Maximum PULSE**	
[kJ]	**SEL**	**L_{peak}**	**SEL**	**L_{peak}**	**SEL**	**L_{peak}**	**SEL**	**L_{peak}**
200	157.8	178.8	155.8	175.3	153.4	171.7	152.8	169.6
370	160.4	181.5	158.5	178.0	156.1	174.3	155.5	172.3
400	160.8	181.8	158.8	178.3	156.4	174.7	155.9	172.6
600	162.5	183.6	160.6	180.1	158.2	176.4	157.6	174.4
800	163.8	184.8	161.8	181.3	159.4	177.7	158.9	175.6
1000	164.7	185.8	162.8	182.3	160.4	178.7	159.8	176.6
1200	165.5	186.6	163.6	183.1	161.2	179.5	160.6	177.4
1400	166.2	187.2	164.3	183.7	161.8	180.1	161.3	178.0
1600	166.8	187.8	164.9	184.4	162.4	180.7	161.9	178.6
1800	167.3	188.3	165.4	184.9	163.0	181.2	162.4	179.1
2000	167.8	188.8	165.8	185.3	163.4	181.7	162.8	179.6
2200	168.2	189.2	166.2	185.7	163.8	182.1	163.3	180.0
2400	168.5	189.6	166.6	186.1	164.2	182.5	163.6	180.4
2600	168.9	189.9	167.0	186.5	164.6	182.8	164.0	180.7
2800	169.2	190.3	167.3	186.8	164.9	183.1	164.3	181.0
3000	169.5	190.6	167.6	187.1	165.2	183.4	164.6	181.3
3200	169.8	190.8	167.9	187.4	165.5	183.7	164.9	181.6
3400	170.1	191.1	168.1	187.6	165.7	184.0	165.2	181.9
3600	170.3	191.4	168.4	187.9	166.0	184.2	165.4	182.1
3800	170.5	191.6	168.6	188.1	166.2	184.5	165.6	182.4
4000	170.8	191.8	168.8	188.3	166.4	184.7	165.9	182.6